The Dissertation Committee for Douglas Paul Breden
certifies that this is the approved version of the following dissertation:

# Simulations of Atmospheric Pressure Plasma Discharges

Committee:

Laxminarayan L. Raja, Supervisor

Clint Dawson

Ofodike Ezekoye

Gary Hallock

Philip Varghese

# Simulations of Atmospheric Pressure Plasma Discharges

**by**

**Douglas Paul Breden, B.S.**

**DISSERTATION**

Presented to the Faculty of the Graduate School of

The University of Texas at Austin

in Partial Fulfillment

of the Requirements

for the Degree of

**DOCTOR OF PHILOSOPHY**

THE UNIVERSITY OF TEXAS AT AUSTIN

August 2013

Dedicated to my family.

# Acknowledgments

I wish to thank my family for all their support over the years. I would like to thank my adviser, Dr. Laxminarayan Raja for guiding me during my time as a student. I also wish to thank all my colleagues who I have worked with during my time as a graduate student including my academic twin Hari Sitaraman and fellow grad students Shankar Mahadevan, Utsav KC, Marshall Albright, Thomas Deconinck, Malcolm White, Michael Pachuilo, Prem Kumar and Frans Ebersohn.

**Simulations of Atmospheric Pressure Plasma Discharges**

Publication No. _____

Douglas Paul Breden, Ph.D.
The University of Texas at Austin, 2013

Supervisor: Laxminarayan L. Raja

This document presents a study of the numerical simulation of non-equilibrium plasma discharges in air mixtures in the atmospheric pressure regime. Such plasma is formed by applying a very high electric field over a very short time duration (nano-microsecond) which preferentially heats the electrons to very high temperatures (10 electron Volts or more) while preventing thermalization of the gas. Preferentially heating the electrons to very high temperatures allows the discharge to efficiently and rapidly ionize and dissociate the gas mixture without losing too much energy to thermalization or vibrational excitation. Consequently, two useful characteristics of these discharges are low gas temperatures and rapid electron chemistry. This study focuses on two applications of interest: ignition of fuel-air mixtures and plasma enhanced medicine. For ignition, there are two situations that arise where it is difficult for traditional spark ignition systems to operate. The first is at

the supersonic flow regime where the residence time of the flow in the engine is low. The second is high pressure ignition of lean fuel-air mixtures. For plasma medicine and surface treatment, non-equilibrium plasma is an effective means of delivering reactive radical species to the surface while limiting damage due to thermal heating. The problems of interest are characterized by the formation of weakly ionized plasma in the presence of flow fields such as supersonic boundary layers or low speed jets. To simulate the coupled plasma-fluid flow physics of these discharges, two numerical tools are utilized. The first is a two-temperature, multiple species, self-consistent plasma solver with finite rate chemistry which is used to simulate the plasma as it forms in a neutral background gas. The second tool is a multiple-species compressible flow solver which calculates the flow field properties of the background gas mixture.

# Table of Contents

# List of Tables

# List of Figures

# Chapter 1

# Introduction

Plasma is a state of matter consisting of a mixture of positive and negatively charged particles, unstable neutral radicals and ground state atoms and molecules. Owing to self-generated electric fields plasmas are quasi neutral meaning that the positive and negative charge densities are almost equivalent, except over a small characteristic length scale (the Debye length) where separation of charge is significant. Furthermore, plasmas can be classified according to whether they are in thermal equilibrium or non-equilibrium. For a thermal plasma, the electrons and ions are the same temperature (sparks, lightning) while for a non-equilibrium plasma the electrons are typically much hotter than the ion and neutral particles.

Plasma occurs naturally or can be produced artificially in a laboratory by applying electromagnetic fields to a gas with sufficiently high field strengths such that the neutral gas is decomposed into its charged components in a process called gas breakdown [86]. The focus of this study is on the numerical simulation of gas breakdown and the formation of non-equilibrium plasma at high pressures. The applications of non-equilibrium plasma investigated in this work are for combustion ignition in supersonic flows, automotive combustion

ignition and atmospheric pressure plasma jets. High voltages are applied as truncated pulses, with pulse widths on the order of tens of nanoseconds. The use of nanosecond pulsing prevents the discharge from transitioning to a spark and the resultant plasma remains non-equilibrium. Such plasma discharges are effective at producing reactive radical species while minimizing energy expended to heat the gas.

This study is organized as follows: the first chapter provides an introduction to the history and development of gas breakdown theory along with a review of several different modern applications of interest. The second chapter provides a discussion of the governing equations that are solved as well as the numerical discretization techniques used. The third chapter presents a scaling study of the parallel plasma code on several hundred cores and discusses some of the limitations inherent in scaling the numerical models to a large number of processors as well as a grid resolution study. The fourth and fifth chapters present the results for computational studies of three modern applications of interests : ignition enhancement in supersonic flows, ignition of lean fuel-air mixtures in IC engines and atmospheric pressure plasma jets. The sixth chapter summarizes the conclusions from this study. The seventh chapter lists research contributions and a discussion of possible future avenues of research.

## 1.1 History of Gas Discharge Theory

Gas discharges due to electrical breakdown have been investigated since the turn of the twentieth century [86] , [85]. In 1900, the classical theory of gas

breakdown between two plate electrodes was developed by J. S. Townsend and students and is often referred to as the Townsend theory of gas breakdown. The essence of the theory is the concept of the exponential multiplication of electrons due to collisions of a few seed electrons with neutral gas particles in an electric field resulting in a so called electron avalanche. The Townsend theory of gas discharge does a reasonable job of predicting the dependence of the breakdown voltage on the product of the gas pressure P and the gap distance d (Pd) (i.e. the Paschen curve of gas breakdown) as well as the time required for the onset of breakdown. The Townsend theory is generally valid for low to moderate values of Pd (Pd $<$ 200 Torr cm) [86].

Subsequent visualization techniques such as the Wilson cloud chamber allowed researchers (Raether et al [85]) to study individual avalanches, avalanche multiplications and gas breakdown as it occurred. Experiments confirmed that Townsend theory does a reasonable job of predicting the behavior at lower pressures, shorter gap distances and moderate applied voltages. At higher (e.g. atmospheric) pressures, large gap distances and high over-voltages it was found that the process of gas breakdown occurred at a much faster rate than what was predicted by Townsend theory. The classic example of gas breakdown for which Townsend theory is not applicable is a spark discharge under long gap conditions.

By the end of the 1930's, it became clear that a new theory was required to explain the formation of gas discharges at high pressures and large voltages. The new theory of spark breakdown was developed independently

by Loeb and Meek [57], [58] and Raether [84] in 1940 and is known as streamer theory. While streamer theory still uses the concept of the electron avalanche to explain the breakdown process, it differs in that it considers a single large electron avalanche rather than a series of avalanches as the mechanism of breakdown. A single large avalanche forms an active zone (the streamer head) which propagates into the gap producing other secondary electron avalanches which are drawn towards the primary avalanche. As the primary avalanche propagates into the gap it leaves behind a long, thin trail of quasi neutral plasma from which comes the term streamer.

It was not until the 1970's that attempts were made to model the process numerically. An early model by Dawson and Winn [23] considered the streamer to consist of a spherical head connected to an ionized plasma channel with a negligibly low conductivity and estimated propagation distance, charge density in the head and streamer radius. In 1972, the streamer equations were solved in one-dimension by Gallimberti [35] who considered charge transport equations and energy conservation and was able to obtain values for streamer length, propagation speed and charge densities that were in good agreement with experiments. It was not until the 1980's and the simulations of Dhali and Williams [28], [29] that the streamer equations were solved numerically in two-dimensions. Since the 1980's numerous research groups have simulated streamers in two and three dimensions using both the fluid and kinetic models.

## 1.2 The Electron Avalanche and Gas Breakdown

The fundamental mechanism that drives the creation of a plasma from a neutral gas by an electric field is the electron avalanche. Before any voltage is applied, the gas is electrically neutral and only a small quantity of charge carriers (electrons with background densities on the order of $10^4 - 10^9 m^{-3}$) are present due to processes such as background UV radiation and cosmic rays. When an electric field is applied, the initial "seed" electrons gain sufficient energy such that as they collide with the neutral gas creating new electron-ion pairs. If $\alpha$ (the ionization coefficient) is the average distance that an electron travels in an electric field before impacting and ionizing a neutral molecule, then the buildup of electrons in an avalanche from a single electron can be expressed as

$$N_e = exp(\alpha x) \tag{1.2.1}$$

where the term $exp(\alpha x)$ is called the amplification factor. The ionization coefficient $\alpha$ is a function of the type of gas used, the density of the gas and the applied electric field.

As the avalanche forms, the highly mobile electrons drift in the direction opposite of the electric field and diffuse radially outward giving the avalanche a teardrop shape. The large ions formed due to electron impact are relatively stationary compared to the mobile electrons and tend to trail the electrons as they drift and diffuse. This results in a region of negative charge in the head of

the avalanche and a positively charged region left in the trail of the electrons. When ions produced by the electron avalanches drift and eventually collide with the cathode, they can free electrons from the surface in a process called secondary electron emission.

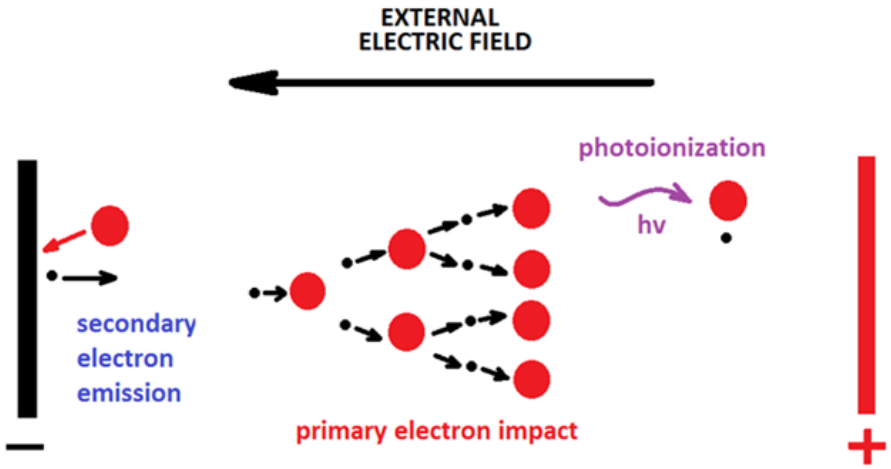


Figure 1.1: Electron production processes due to electron impact (primary processes) results in multiplication of electrons. The source electrons for the electron avalanche are produced by processes such as surface emission or photo-ionization (secondary processes).

Consider the case of two parallel metal plates separated by a gap and containing some gas. A constant electric field is applied between the two metal plates. Assume a single electron is liberated from the cathode and is accelerated by the electric field creating an electron avalanche. As the electrons fall towards the anode, the positive ions produced by the ionizing electrons fall towards the cathode. If the positive ions impact the electrode, they can knock more electrons free from the cathode which in turn create new electron avalanches. One can then imagine the breakdown of the gas as being due to

a sequence of electron avalanches which initially start at the electrode and drift towards the anode. At lower pressures, a plasma is typically sustained by multiple electron avalanches which are ejected from the cathode by ion or UV bombardment and drift in the electric field.

## 1.3 Streamer Theory

In this section, a brief review of streamer theory is presented (refer to [86] for a more detailed discussion or refer to the papers by [84] [57] which originally presented the theory). Like the classic Townsend theory, the concept of electron avalanches plays a central role. It differs in that there is a single large electron avalanche that dominates rather than a sequence of avalanches. The space charge produced by the dominant avalanche induces an electric field that is great enough to produce other secondary avalanches in the vicinity of the avalanche head which are then drawn towards the primary avalanche. The subsequent plasma discharge is referred to as a streamer and consists of two features: an active head region where ionization/photo-ionization and secondary avalanche production take place and an inert quasi neutral plasma tail left behind by the active region as it propagates.

The primary factor that governs whether an avalanche will transition into a streamer is the induced electric field of the electron avalanche. Consider the amplification factor $\exp(\alpha x)$ of electrons in an electron avalanche. If the gap distance, the gas pressure (density) or applied voltages are large then the amplification factor can become large. The charge produced by the electron

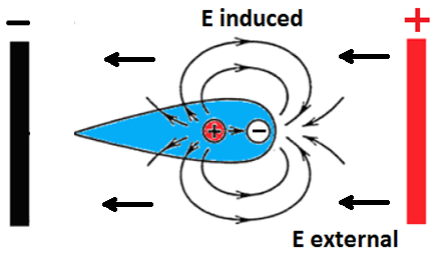


Figure 1.2: In an electron avalanche the mobile electrons drift radially outward giving the avalanche a teardrop shape. The slow moving ions lag behind the electrons inducing an electric field. When the induced electric field is of the same order as the external field, the avalanche transitions into a streamer.

avalanche can then become significant enough that the charge in the electron avalanche head distorts the externally applied field. The electric field due to the electrons produced by a streamer avalanche with a spherical streamer head can be written as [86]

$$E^i = \frac{eN_e}{R^2} = \frac{e}{R^2} exp(\alpha x) \approx E_0 \tag{1.3.1}$$

,

where $E^i$ is the electric field "induced" by the space charge, $E_0$ is the applied electric field, $\alpha$ is the effective ionization coefficient and R is the radius of the streamer. The criterion for an avalanche to form a streamer is that the induced electric field should be of the same order as the applied electric field. This will occur when the amplification factor $\exp(\alpha x)$ is large (as is the case for large Pd values or large voltages). From the previous section, it was mentioned that the mechanism that sustains the plasma at low pressures is the formation of new avalanches at the cathode due to ion bombardment at the cathode

surface. In streamer theory, the secondary avalanches are produced locally near the active region of the streamer head due either to electrons that drift from the primary avalanche or from electrons produced by photo-ionization.

Unlike the electron avalanche which propagates due to the drift of electrons in the field, the streamer propagation mechanism is wave like in nature and is driven by the exchange of energy from the ionization of charged particles (kinetic energy) and the subsequent displacement of the electrostatic field due to the new space charge (potential energy). Fig. 1.3 illustrates the mechanism by which a streamer propagates. Initially, the streamer head consists of a region of positive ions created by the primary avalanche which creates the induced electric field that locally generates other secondary avalanches. The electrons from the secondary avalanche drift towards the streamer head and neutralize the space charge in that region creating the quasi neutral plasma. The positive ions left behind by the secondary avalanches form the region of a new streamer head. The rate at which the streamer head propagates in space ($10^5 - 10^6 ms^{-1}$) is typically much greater than the drift velocities of ions (order of $10^3 - 10^4 ms^{-1}$) and often even the electrons (order of $10^4 - 10^5 ms^{-1}$).

Note that an electron avalanche can transition to a streamer from either the cathode, the anode or mid gap and can propagate in both directions. The location from where the streamers propagate is dependent on where the induced electric field of the primary avalanche reaches a level that is comparable to the externally applied electric field. Streamers that propagate towards the cathode are called positive or cathode-directed streamers while stream-

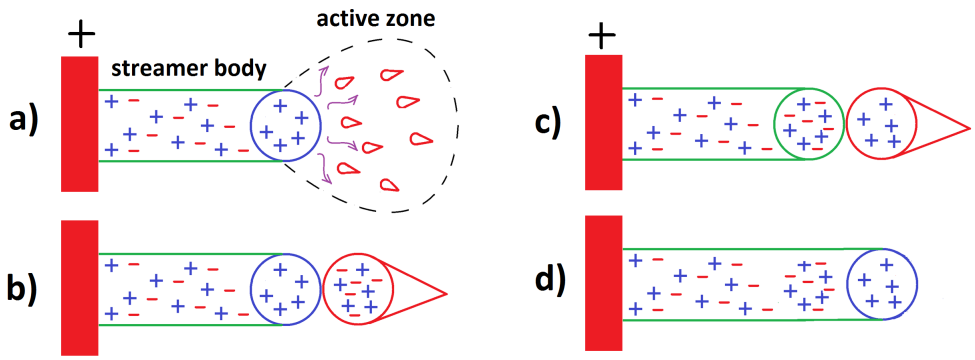


Figure 1.3: Streamer propagation is a wave phenomena governed by the rapid ionization of space charge due to self-induced electric fields. a) The positive space charge in the streamer head produces an electric field that generates smaller secondary avalanches which are drawn towards the head. b) Replace the many separate avalanches by a single "effective" avalanche. c) When the avalanche makes contact with the streamer head, the avalanche electrons move to neutralize the positive net space charge. d) The positive ions in the avalanche left behind by the electrons form a new streamer head.

ers that propagate towards the anode are called negative or anode-directed streamers. In practice, positive streamers are easier to form than negative streamers (requiring lower voltages) and all the results presented in this study are of positive (cathode directed) streamers.

## 1.4 Streamer Modeling

Streamers can be modeled mathematically using either a kinetic approach or a fluid model. Most modeling in the literature uses a fluid modeling approach consisting of conservation equations for the different plasma species coupled with the electrostatic potential equation. A simple fluid model for streamer propagation (for a plasma with a single ionized species) consist of

three equations : an equation for conservation of electrons and the ions and the self-consistent electrostatic potential equation. (e.g. Gallimberti 1972 [35])

$$\frac{\partial n_e}{\partial t} + \vec{\nabla} \cdot \mu_e E n_e - D\nabla\vec{n}_e = \alpha n_e \mu_e E \tag{1.4.1}$$

$$\frac{\partial n_i}{\partial t} = \alpha n_e \mu_e E \tag{1.4.2}$$

$$\nabla^2 \phi = \frac{e}{\epsilon_r \epsilon_0}(n_i - n_e) \tag{1.4.3}$$

Physically, the first equation represents conservation of electrons with a convection and diffusive flux term and production rate source term $\alpha n_e \mu_e E$ is the ionization rate. The second equation represents conservation of a single positively charged ion species. The ion drift velocities relative to the streamer propagation are low enough that they can be neglected and only the change in time due to production from electron impact collisions is considered. The third equation is the electrostatic Poisson equation for the self-consistent electric fields both external and induced. Note that physically, the above set of governing equations serve to model the production and transport of the electron avalanches both primary and secondary in the active zone of the streamer head. In addition to the above set of equations, a mechanism for producing the seed electrons needed for the secondary avalanches must be included. The model by Gallimberti included a photo-ionization mechanism but it is also possible to specify an initial electron background density. Although modern numerical models (such as the one in this study) can account for multiple species, more complicated chemistry, electron and ion energies and separate

equations for the ion momentum and photo-ionization, at their core they are essentially the same model as this one : charged species conservation equations coupled with the Poisson equation.

The above set of equations, despite their relatively simple form, were computationally prohibitive to solve in their given form until around the 1970s'-1980's. The simulation work by Gallimberti in 1972 [35] solved a simplified version of the above equations in one dimension by assuming that the secondary avalanches could be replaced with a single effective electron avalanche and then modelling energy conservation due to ionization and the electric fields for that single avalanche. Simuations were performed in one dimension and were found to be in good agreement with experiments.

It was not until the 1980's that it became feasible to solve the fluid equations with the Poisson equation in two-dimensions. The first two-dimensional simulations of streamers were performed for atmospheric nitrogen by Dhali and Williams ( [28] and [29] ). Since the 1990's multiple research groups have used two and three dimensional streamer models to simulate streamers of both polarities for numerous gas mixtures and electrode geometries.

## 1.5 Nanosecond Pulsing

At high pressures, a non-equilibrium plasma will typically transition to a thermal spark plasma unless there is some mechanism by which to prevent the transition. One such method is to cover one or both of the electrodes by a dielectric material which inhibits the flow of conduction current to the

plasma and prevents transition to spark. The other method which is of greater relevance to this work is the concept of nanosecond pulsing.

Using high voltage nanosecond pulsing to produce non-equilibrium plasma at high pressures is a concept introduced by [46], [72]. The basic premise is to apply a voltage greater than the required breakdown voltage over very short pulses. The high voltage results in very rapid ionization and the formation of non-equilibrium plasma over very short (1-10 nanoseconds) times. Limiting the pulse to nanosecond time scales prevents the plasma from transitioning into a thermal spark plasma.

Pulsing allows the electric fields and thus the electron energy distribution to be efficiently controlled. At low electron energies, vibrational excitation of molecules such as nitrogen and oxygen are dominant while at high energies electron impact ionization and dissociation reactions are dominant. Nanosecond pulsing preferentially heats the electrons to very high temperatures which gives the electron energy distribution function a high energy tail. Preferentially heating the high energy tail of the distribution function allows the deposited electric field energy to be utilized for ionization and dissociation reactions instead of being wasted on low energy vibrational excitation. Thus, nanosecond pulsing is an efficient technique for generating plasma at room temperature while minimizing energy lost to vibrational excitation or heat.

Once the plasma has been produced, it takes a finite amount of time ( microseconds) for the plasma electrons to recombine with the ions. By pulsing the voltage, a non-equilibrium plasma can be sustained at high pressures

with minimal energy expenditure. Fig. 1.4 illustrates the process by which pulsing the voltage sustains a non-equilibrium plasma. For most of the simulations in this work, the plasma discharge is simulated for a single nanosecond pulse event.

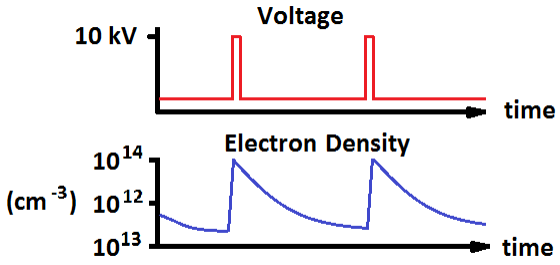


Figure 1.4: High voltage nanosecond pulses are applied to an atmospheric pressure gas (TOP). A non-equilbirium plasma forms during the time scale of the pulse and the plasma begins to recombine after the pulse is switched off while limiting energy expenditure lost to heating or vibrational excitation (BOTTOM).

## 1.6 Applications

In this section, several applications and relevant experimental and numerical studies on non-equilibrium discharges at atmospheric pressures are reviewed. This work focuses primarily on three such applications of interest. The first is ignition enhancement of supersonic combustible flow due to rapid production of combustion enhancing radical and metastable species. The second is ignition enhancement of lean fuel-air mixtures at high pressures (e.g. 10 atmospheres) for automotive combustion applications. The final application of interest is surface modification and biomedical plasma treatment of tissue

using non-equilibrium atmospheric pressure plasma jets.

### 1.6.1 Plasma Assisted Supersonic Ignition and Flow Actuation

Non-equilibrium plasma produced by high voltage nanosecond pulses have been investigated for applications involving flow actuation [111], [53], [106], [99], stabilization of lean air flames [81], [82], and ignition of supersonic flows [104].

Figure 1.5: Pulsed non-equilibrium plasma assisted ignition of ethylene-air mixture at 70 Torr in flow from experiments of [59].

There have been numerous experiments and numerical simulations [7], [6] [31], [30], [50], [59] which have investigated nanosecond pulsed plasma for combustion enhancement. The primary means by which such plasma is believed to enhance flow ignition is through production of combustion enhancing radicals such as O, H and OH in oxygen-hydrogen ($O_2-H_2$) gas mixtures. Plasma discharges produce radicals by thermal dissociation, electron impact dissociation or the excitation of metastable states. The timescale of thermal dissociation is long (milliseconds), and is therefore inefficient in the production of radicals to ignite a flow moving at supersonic speeds. Electron impact dissociation on the other hand, occurs on a much faster timescale (nanoseconds)

and therefore has the ability to significantly reduce ignition delay. A third mechanism by which the plasma can enhance combustion is through excitation of the bulk gas into long lived metastable excited states. The electron energy essentially gets stored by these metastable molecules which are then convected downstream of the discharge region. Experiments and simulations [17], [101], [103] have demonstrated that metastable oxygen produced by non-equilibrium plasma can reduce ignition delay of fuel-air mixtures. Other experiments [100] and simulations [8] have demonstrated that metastable species produced by the discharge (such as metastable nitrogen) can play a dominant role in the production of atomic oxygen radicals.

In addition to radical production for supersonic ignition, nanosecond pulse dielectric barrier discharges have shown promise as flow actuators. While it has been established by experiments and numerical simulations [34], [56] that the plasma produced by a dielectric barrier discharge can induce a net flow velocity due to the volumetric electrostatic forcing term, this mechanism is only effective at lower flow velocities. Recent experiments [87], have demonstrated that another mechanism by which plasmas can actuate flow is rapid (sub microsecond) gas heating which results in micro blast waves that efficiently transfer momentum to the boundary layer region and are potentially more effective at higher flow velocities.

### 1.6.2 High Pressure Ignition of Lean Mixtures

The conventional spark ignition (SI) device has been used for internal combustion (IC) engine ignition applications for well over a hundred years and has proved to be a reliable workhorse device with relatively few changes to the basic design over that period. The SI device produces a constricted arc plasma between two closely spaces electrodes resulting in a localized hot-spot with temperatures of order 1 eV. The high temperature thermally dissociates the gas into a near-equilibrium composition of combustion enhancing radicals such as O, H, and OH. The high gas temperatures drive chain initiation and chain branching reactions that result in combustion ignition and flame propagation. The high gas temperatures produced by the arc results in relatively large energy dissipation per spark pulse.

The use of non-equilibrium (cold) plasmas for combustion ignition in internal combustion engines has been a topic of significant recent interest ( [95]). In particular, these plasmas have shown the potential to improve combustion ignition characteristics in ultra-lean fuel-air mixtures with improvements to the engine thermal efficiency and decreased pollutant formation. Several studies have shown that the lean flammability limit in IC engines is significantly improved with non-equilibrium plasmas compared to conventional SI devices [96], [98]. Unlike an SI device that relies on a local thermal hot-spot to produce an ignition kernel, non-equilibrium plasmas cause negligible gas heating. Instead much of the electrical energy delivered to the devices is consumed in heating the electrons selectively to high temperatures which in turn

efficiently dissociates and ionizes the gas mixture to produce copious amounts of combustion enhancing radicals. The radicals in turn are believed to promote exothermic reactions that subsequently heat the gas to form a viable combustion ignition kernel. The detailed mechanistic explanation for why non-equilibrium plasmas are more effective at combustion ignition and flame stabilization compared to SI devices, especially under lean combustion conditions, is still elusive and is the subject of recent research. One explanation for the above is the formation of a larger effective ignition kernel due to the more voluminous nature of non-equilibrium plasmas compared to a localized SI arc. Other explanations allude to significant differences in the composition of combustion-enhancing radical species produced by a non-equilibrium plasma compared to an SI arc. Most of these explanations appear plausible but are invariably difficult to test in a real experimental setting owing to the complexity of the internal combustion engine geometry and operation, the localized placement of the ignition device within a cylinder bore, and the extremely small time scales associated with the plasma ignition event.

At the high pressures of interest to IC engines, non-equilibrium discharges tend to self-constrict and propagate as thin streamers. Fig. 1.6 illustrates two different non-equilibrium igniter configurations that have recently been investigated. Recent work by Shiraishi et al. [95] in collaboration with Gundersen and co-workers [98] have demonstrated non-equilibrium discharge sources that are compatible with requirements of ignition system in an IC engine. One of the sources is a coaxial electrode discharge driven by single high

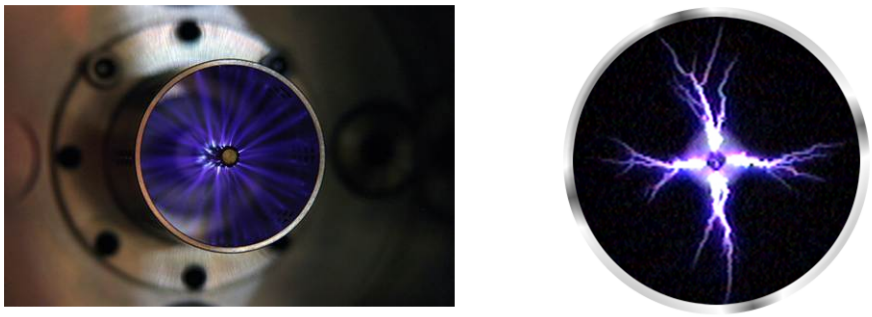

Figure 1.6: Example of a non-equilibrium plasma igniter for short gap (millimeters) (image from [2] ) (LEFT) and long gaps (centimeters) (image from [1]) (RIGHT).

voltage pulses (10s kV) per ignition cycle, with pulse durations of 10s of ns. A typical interelectrode gap of several mm was used with an inner electrode diameter of about 2 mm. Some of the reports on this discharge have also described the inner electrode as being decorated with screw threads that assist in electric field intensification for discharge breakdown. The authors refer to this source as a High-Speed Pulsed (HSP) igniter [96]. The other is a dielectric barrier discharge, referred to as Barrier Discharge Igniter (BDI) by the authors [95], which has a similar coaxial electrode geometry as the HSP with the addition of a dielectric covering to the inner powered electrode. The outer bare electrode of the BDI was also decorated with small protrusions (prongs) that presumably help in discharge breakdown and in spreading the discharge within the discharge gap. The discharge gap for the BDI was about 1 mm and the BDI is driven by high-voltage (10s kV), low radio-frequency (RF) ( 10 kHz) excitation in a continuous burst of 10s of waveforms per ignition cycle. The

function of a dielectric barrier is well known [94], [118]. The thin streamers that are formed during one half of the RF cycle (say positive voltage on the inner electrode) results in cathode directed streamers from the inner dielectric covered electrode to the outer grounded electrode. The outward propagating streamers deposits a negative charge on the dielectric covering at the foot of the streamer results in a localized self-induced electric field that opposes the imposed electric field from the inner electrode. During the next positive cycle the new cathode-directed streamers are forced to emerge from a different foot location than the streamers from the previous cycle thus lending to a relatively uniformly distributed discharge over period of several RF cycles. The overall negative charge on the inner dielectric due to the positive half cycles is balanced by positive charge deposition during the negative half cycle that results in either anode directed streamers starting from the inner electrode or cathode directed streamers starting from the outer bare electrode.

### 1.6.3 Atmospheric Pressure Plasma Jets

Cold atmospheric plasma jets have shown significant promise in applications such as biomedical surface modification [49], [48]. A typical configuration of the plasma jet might consist of a dielectric tube ( mm radius) through which a low speed jet ( 10 m/s) of noble gas such as helium or argon exhausts into ambient air. The jet is characterized by a fluid mechanical mixing layer where the noble gas and air species diffuse. High voltage sinusoidal or nanosecond pulse waveforms are then applied to an electrode wrapped around or embed-

ded within the tube. The resulting plasma forms along the jet axis extending as far as 5-10 cm downstream of the tube exit. A favorable characteristic of this type of discharge is the ability to deliver chemically reactive species at relatively long-distances downstream ( 1-10 cm) of the tube with negligible gas temperature increase; which makes them ideal for delicate material processing (e.g. treatment of human skin). Fig. 1.7 provides an example of one such device that uses helium as the working gas to produce an atmospheric pressure plasma jet in ambient air.

Figure 1.7: Example of an atmospheric pressure plasma jet from the experiments of [93]. Helium gas with flow rate of 15 l/min and voltage of 3.8 kV with rep rate of 25 kHz. Jet length is approximately 4 cm.

Recent experimental studies have increased the general understanding of the physical processes taking place within the discharge [49], [60], [109], [93], [71], [90], [114], [112]. It is now well established that cold plasma jets produced by nanosecond pulsed discharges in a region of inert gas are in fact a series of rapidly propagating streamer discharges that are guided parallel to the axis of the fluid mechanical helium jet as it diffuses into the stagnant ambient air. Short exposure imaging of the jet reveals a luminous zone confined to the head of the streamer that travels at very high speeds ( 100 km/s) and travels up to a few centimeters downstream of the jet nozzle exit, [60], [109] leading to

the common description of these structures as plasma bullets. Furthermore, imaging of the plasma jet along the axis reveals that the luminous zone is in fact ring-shaped, i.e. the peak luminosity occurs off the jet axis in a toroidal shape [71], [90].

To date, significant efforts to develop theories and numerical models to understand these experimental observations have been made. For instance, Sakiyama et al. [90] developed a one-dimensional model and showed that the ring-shaped luminous zone resembles the profiles of certain species (nitrogen ions and metastable helium atoms) leading to the conclusion that the Penning reactions play a vital role in the formation of such a luminous zone (also mentioned in [44]). Two-dimensional models developed by Boeuf and Pitchford [14] and Naidis [74] successfully simulated the ring-shaped luminous zone suggesting that the discharge was driven by electron impact in a streamer propagating along the interface of the helium-air mixing layer. Furthermore, the recent work by Naidis [75] has shown that the radial position where the concentration of electron and metastable nitrogen molecules reach a maximum coincides with the position where the air molar fraction is about 1 percent in the mixing layer. Naidis also concludes that the ring structure is attributed primarily to electron-impact ionization processes and not Penning reactions.

# Chapter 2

# Numerical Models

The problems of interest are typified by plasma kinetics coupled with fluid dynamics. The time and length scales that govern each phenomena can differ by several orders of magnitude. Two different simulation tools are utilized for this study: a plasma fluid solver and a compressible flow solver. The flow solver is responsible for determining the bulk flow kinetics of dominant neutral background species including mole fractions, gas temperature, pressure and velocity. The plasma solver determines the kinetics and energetics of the plasma species and accounts for finite rate chemistry.

## 2.1 Non-Equilibrium Plasma Governing Equations

The core of the model consists of solving multiple species continuity equations with the electrostatic potential equation. The current densities are assumed to be low enough that self-consistent magnetic fields can be safely neglected compared to the electric fields. There are two characteristic temperatures, a heavy species temperature and a separate electron temperature. Each temperature is obtained separately by solving energy conservation equations.

The model has been used to simulate a wide range of discharges and

previously published work in our group includes micro discharges [108], DC discharges for plasma actuators [66], streamer discharges for supersonic ignition [20], and atmospheric pressure plasma jets [21].

#### 2.1.0.1 Species Continuity

The number densities of the electrons, ions and neutrals are obtained by solving separate continuity equations for each gas species with finite rate source terms.

$$\frac{\partial n_k}{\partial t} + \vec{\nabla} \cdot \vec{\Gamma_k} = \dot{G_k}, \quad k = 1, 2, 3... \tag{2.1.1}$$

The species flux $\vec{\Gamma_k}$ can be obtained in two ways: by solving separate momentum equations for each equation or by using the drift-diffusion approximation. The drift-diffusion approximation assumes that the inertial terms of the momentum equation can be neglected and is valid when the mean free path is significantly smaller than the characteristic length scale of the problem [111]. This is typically the case at atmospheric pressures and length scales of the order of millimeters or greater.

The drift-diffusion flux consists of a mobility flux term (for charged species), a diffusive flux term, and the species flux due to the flow velocity field.

$$\vec{\Gamma_k} = n_k \vec{u_k} = Z_k \mu_k n_k \vec{E} - D_k \vec{\nabla} n_k + n_k \vec{v} \tag{2.1.2}$$

#### 2.1.0.2 Electrostatic Potential

The imbalance of net space charge due to the charged species densities will generate self-consistent electric forces. By assuming that the current densities are small (weakly ionized plasma), magnetic fields can be neglected and the Maxwell equations can be reduced to solving a single Poisson equation for the electric potential.

$$-\nabla^2\phi = \frac{e}{\epsilon_r\epsilon_0}\sum_k Z_k n_k \tag{2.1.3}$$

The electric field is obtained by taking the gradient of the potential

$$\vec{E} = -\vec{\nabla}\phi \tag{2.1.4}$$

$\epsilon_0$ is the permitivity of free space and $\epsilon_r$ is the relative permitivity (e.g. 1 for air), e is the electron charge in Coulombs and $Z_k$ is the charge number of species k (e.g. -1 for electrons). Note that the electrostatic potential is dependent on the charged species densities while the charged species motion is dependent on the electrostatic potential (electric field). In particular, the coupling of the highly mobile electrons to the potential equation results in a stiff set of equations which typically requires taking very small time steps. To alleviate the stiffness due to the coupling of the electrons and the electrostatic potential, the potential equation is solved in a semi-implicit manner as described in references such as [83] [39].

#### 2.1.0.3 Heavy Species Energy

It is assumed that all heavy species (ions and neutrals) are in thermal equilibrium with each other. When the plasma equations are solved in tandem with an external flow model, the complete bulk energy conservation is not solved. Instead, the gas heating source terms, $S_{T_g}$ are collected and communicated to the flow model which is then responsible for determining the bulk temperature.

$$S_{T_g} = \Psi \sum_{k_{ions}} Z_k \vec{\Gamma_k} \cdot \vec{E} + e \sum_{i_{rxn}} \Delta\varepsilon_i^e r_i + \frac{3}{2} k_b n_e \frac{2m_e}{m_{k_b}} (T_e - T_g) \nu_{e,k_b} \qquad (2.1.5)$$

Three gas heating source terms are calculated by the plasma solver. The first term is the ion Joule heating term due to the work done on the ions by the electric field. The term $\Psi$ is an efficiency factor specified to indicate the amount of Joule heating energy that is converted into thermal energy. This term is typically set to 1 when at higher (atmospheric) pressures or when energy loss to the wall by direct ion impact can be neglected [111]. The second term is the inelastic collisional heating term due to the quenching of electronically excited species such as nitrogen, oxygen and helium metastables. The last term is the elastic collisional heating term due to elastic electron impacts with the background gas.

#### 2.1.0.4 Electron Energy

The electron temperature can be obtained by solving a conservation equation for the mean electron energy.

$$\frac{\partial \epsilon_e}{\partial t} + \vec{\nabla} \cdot \vec{\Gamma_\epsilon} = S_{T_\epsilon} \tag{2.1.6}$$

The term $\vec{\Gamma_\epsilon}$ represents the flux of electron energy due to convection and diffusion

$$\vec{\Gamma_\epsilon} = (\epsilon_e + p_e)\vec{u_e} - k_e \nabla \vec{T_e} \tag{2.1.7}$$

On the left hand side, the first term is the unsteady term, the two terms contained within the divergence operator represent convection of energy and diffusion of energy (through Fouriers heat conduction law).

This flux can be re-expressed in terms of the mean electron energy $\epsilon_e$ and the electron species transport properties $D_e$ and $\mu_e$.

$$\vec{\Gamma_\epsilon} = -\frac{5}{3}\mu_e \vec{E} \epsilon_e - \frac{5}{3} D_e \nabla \vec{\epsilon_e} \tag{2.1.8}$$

The energy source term $S_{T_e}$ consists of three terms: Joule heating due to the electric field, as well as inelastic and elastic collisional energy loss due to the electrons colliding with the heavy species. All three source terms are written below as

$$S_{T_e} = -e\vec{\Gamma_e} \cdot \vec{E} - e\sum_{i_{rxn}} \Delta\varepsilon_i^e r_i + \frac{3}{2}k_b n_e \frac{2m_e}{m_{k_b}}(T_e - T_g)\nu_{e,k_b} \tag{2.1.9}$$

Finally, a mean electron temperature can be defined using the relation $\epsilon_e = \frac{3}{2}k_b T_e$.

#### 2.1.0.5 Air Photoionization

The propagation of fast ionization waves is dependent on seed electrons, and when the direction of propagation is in the direction opposite to the drift-electrons, an external source of electron seed charge is required. The main source of seed electrons, particularly in air, is the ionization of oxygen molecules due to the emission of photons from nitrogen molecules that have been electronically excited by the ionization wave front. The entire process can be expressed as a single reaction whose rate we wish to determine ($O_2$ + h$\nu$ $->$ E + $O_2^+$).

A common approach to calculating this source term is to use an integral model where the ionization at one point is dependent on a quadrature of an emission and absorption function taking over a part of or the entire domain of interest. The integral model of Zheleznyak [69] is a commonly used integral model for air photo ionization. The advantage of the integral model is its simplicity and its high degree of accuracy. The major disadvantage of the integral model is that it is computationally expensive, with a cost on the order of $n^2$ calculations every solution step (where n is the number of cells). In

addition to the classic integral model of Zheleznyak, there are several approximate photo ionization models developed in recent years from which to choose from. Segur and coworkers [76] proposed models that are approximations to radiative transfer equations known as the Eddington and $SP_3$ approximations. Luque and coworkers [4] proposed a method where the problem of solving the Zheleznyak integral of the classical integral model [69] model can be reposed as a problem where two Helmholtz differential equations are solved. Bourdon et al. [3] performed a series of verification tests and found that the three-term Helmholtz model and $SP_3$ model are in close agreement with the Zheleznyak integral model, particularly in regions away from walls.

*Zheleznyak Model*

For this study, a three-term version of the Helmholtz model described in Bourdon et al. [3] along with relevant fit data and parameters for air was chosen. From the model of Zheleznyak, the photo ionization source term at a point in space $\vec{r'}$ can be expressed as an integral over the domain of interest.

$$S_{ph}(\vec{r}) = \int_V \frac{I(\vec{r'})g(R))}{4\pi|\vec{r} - \vec{r'}|^2} dV \tag{2.1.10}$$

R = $|\vec{r} - \vec{r'}|$ is the distance between the location of the emitter species ($N_2$) at $\vec{r'}$ and the absorber species ($O_2$) at $\vec{r}$. $I(\vec{r'})$ is an emission function that characterizes the intensity of radiation from emitting species (($N_2 -> N_2 +$ E + h$\nu$) in this case).

$$I(\vec{r'}) = \frac{P_q}{P + P_q} \xi S_i(\vec{r'}) \tag{2.1.11}$$

where it is assumed that photon emission is proportional to the rate of ionization $S_i(\vec{r'})$ of the emitting species ($N_2$), $\xi$ ( 0.02) is an efficiency factor and $\frac{P_q}{P+P_q}$ is a quenching factor, where $P_q$ is found from experiments ( 30-60 Torr) and P is the total gas pressure.

The kernel function $g(R)$ is measure of the transport of radiation and determines the absorption of photons by oxygen molecules and is dependent on the partial pressure of the absorbing species ($P_{O_2}$). The absorption function when divided by the partial pressure of oxygen can be expressed as

$$\frac{g(R)}{P_{O_2}} = \frac{e^{-\chi_{min}(P_{O_2}R)} - e^{-\chi_{max}(P_{O_2}R)}}{(P_{O_2}R)ln(\frac{\chi_{max}}{\chi_{min}})} \tag{2.1.12}$$

where the $\chi_{max}$ and $\chi_{min}$ are obtained experimentally.

*Three-Term Helmholtz Model*

For the Helmholtz model, the primary idea is to approximate the source term by a summation of three(or more) terms

$$S_{ph}(\vec{r}) = S^1_{ph} + S^2_{ph} + S^3_{ph} \tag{2.1.13}$$

The absorption function $\frac{g(R)}{P_{O_2}}$ can be approximated by fitting a series of exponentially decaying functions written as $\frac{g(R)_j}{P_{O_2}} = (A_j P_{O_2})e^{\lambda_j P_{O_2} R}$ where$\lambda_j$ and $A_j$ are parameters. The parameters $\lambda_j$ and $A_j$ are obtained by fitting the summation of the three exponential functions terms in the $S_{ph,j}$ terms to experimental data obtained for the original absorption function of air $\frac{g(R)}{P_{O_2}}$.

| | $A_j(cm^{-1}Torr^{-1})$ | $\lambda_j(cm^{-1}Torr^{-1})$ |
|---|---|---|
| $S^1_{ph}$ | 0.0067 | 0.0447 |
| $S^2_{ph}$ | 0.0346 | 0.1121 |
| $S^3_{ph}$ | 0.3059 | 0.5994 |

Table 2.1: Air photo-ionization absorption parameters

Bourdon et al. [3] performed a curve fit for three exponential functions and obtained values for $_j$ and $A_j$ which are tabulated in Table 2.1.

The key reason for approximating the absorption function using several exponential functions is that the individual photo ionization source terms now have the form

$$S^j_{ph} = \int_V \frac{I(\vec{r})}{4\pi R} A_j P^2_{O_2} e^{-\lambda_j P_{O_2} R} dV \tag{2.1.14}$$

which is the integral solution to a Helmholtz equation. Hence the original integral problem can be reposed as a problem where three or more Helmholtz equations are solved over the domain

$$\nabla^2 S^j_{ph} - (\lambda_j P_{O_2})^2 S^j_{ph} = -A_j P^2_{O_2} I(\vec{r}) \tag{2.1.15}$$

It is important to note that the contribution of helium photons to the process of photo ionization has been neglected. The primary consequence of neglecting the contribution of helium photo ionization will be that the simulated speed of the propagating discharge when helium is present will be under predicted.

#### 2.1.0.6 Transport Properties

The transport coefficients for species drift and diffusion $\mu_k$ and $D_k$ and the thermal conductivity $K_k$ are derived using a hard sphere collision model. It is assumed that the plasma product species drift in a predominatly neutral gas mixture consisting of background gas particles with a density $n_b$. The collision frequency of a species k with the background gas is

$$\bar{\nu}_{e,k_b} = n_b \bar{g} \sigma \tag{2.1.16}$$

Where $n_b$ is the total background density, $\bar{g}$ is the mean thermal velocity, and $\sigma$ is the total momentum transfer collision cross section. Once the collision frequency of a species k with the background is known, the mobility and diffusion coefficients are derived using the following equations.

$$\mu_k = \frac{Z_k e}{m \bar{v}_{e,k_b}} \tag{2.1.17}$$

$$D_k = \frac{k_b T_k}{m \bar{v}_{e,k_b}} \tag{2.1.18}$$

The thermal conductivity coefficient of the electrons and the heavy gas species is found from

$$K_k = \frac{5}{2} \frac{k_b D_k}{m_k} \tag{2.1.19}$$

As an alternative to the hard sphere model, the transport coefficients can be derived from experimentally provided mobilities. The mobility and diffusion coefficients for different ions in different mixtures are often available as a function of the reduced electric field (E/N) or the mean electron energy which can be tabulated in look-up tables. The diffusion coefficient can then be calculated from the mobility coefficient using Einsteins relation, $D_k = \frac{kT}{e}\mu_k$.

The average species flow velocity transport variable, $\vec{v}$, is obtained by solving the Navier-Stokes equations for the background species separately from the plasma governing equations.

### 2.1.1 Boundary Conditions

Boundary conditions are imposed by specifying flux boundary conditions at the boundaries of the problem domain.

#### 2.1.1.1 Fixed Value

If a fixed value (Dirichlet) boundary condition is to be imposed, a flux is derived using the value of the imposed variable at the boundary and the value of the variable in the cell interior adjacent to the boundary in much the same manner as how the face fluxes are computed in the domain interior. Examples of this boundary condition include the specification of fixed temperatures or a fixed voltage (e.g. ground at the far-field boundaries).

#### 2.1.1.2 Symmetry

Often a symmetry boundary condition is imposed. This is most often the case for open boundaries or boundaries that lie along a plane of symmetry. This boundary condition simply states that the value of the conserved variable is the same on both sides of the boundary face. Note that although the gradient of the variable is zero, the flux itself need not be zero (as would be the case for a zero-flux boundary condition).

#### 2.1.1.3 Solid Surface Fluxes

At surface boundaries, the flux is dependent on the state of the conserved variables in the cells adjacent to the boundary (such as temperature for the flux of species) or some quantity on the face itself (surface charge for the case of electrostatic potential). The solid surface flux boundary conditions for different equations are listed in this sub section.

*Species Densities*

For solid surfaces, electron number density flux $\vec{\Gamma_e}$ is calculated using the equation

$$\vec{\Gamma_e} \cdot \hat{n}_s = \frac{1}{4} n_e \sqrt{\frac{8 k_b T_e}{\pi m_e}} - \sum_k \gamma_k \vec{\Gamma_k} \cdot \hat{n} \tag{2.1.20}$$

The electron flux to a surface contains two terms. The first term represents a Maxwellian flux to a surface $\frac{1}{4} n_k \bar{c}$ as a function of the electron temperature. The second term accounts for secondary electron emission from the surface due to bombardment of ionized particles. The wall surface normal

direction $\hat{n}$ is directed int the wall. The variable $\gamma_k$ is the secondary emission coefficient and physical represents the percentage of ion impacts that result in an electron being emitted from the surface.

For neutral species, heavy ions and metastables the flux $\vec{\Gamma_k}$ is specified in much the same way as for the electrons,

$$\vec{\Gamma_k} \cdot \hat{n}_s = \frac{1}{4} n_e \sqrt{\frac{8 k_b T_e}{\pi m_e}} + (0, n_k Z_k \vec{E} \cdot \hat{n}) \tag{2.1.21}$$

where neutral and metastable species fluxes consist entirely of the Maxwellian flux which is a function of the heavy species temperature. For charged species if the product of the electric field normal into the wall and the charge number ($Z_k \vec{E} \cdot \hat{n}$) are greater than zero (indicating bombardment to the surface), then the second term is included.

*Electrostatic Potential*

When a solid surface is a dielectric, charge that is deposited to the surface will remain trapped at the surface which in turn result in a jump boundary condition for the electrostatic potential at the surface.

The charge that accumulates on the surface $\rho_s$ due to the flux of all charged species k with charge number $Z_k$ is given by

$$\frac{\partial \rho_s}{\partial t} = e \sum_k Z_k \vec{\Gamma_k} \cdot \hat{n_s} \tag{2.1.22}$$

which depends on the charge accumulation at the surface as a function of the net charged species fluxes to the surface.

The electrostatic potential at the dielectric surface $\phi_d$ is then calculated using Gauss Law

$$\phi_d = \frac{\phi_c + \frac{\delta x}{\epsilon_0}(\rho_s + \frac{\epsilon_d \epsilon_0}{d}\phi_b)}{1 + \frac{\delta x}{d}\epsilon_d} \tag{2.1.23}$$

where $\phi_b$ is a potential specified on the opposite side of the dielectric, $\phi_c$ is the potential at the cell center adjacent to the boundary, $\delta x$ is the distance from the cell center to the face, d is the thickness of the dielectric, and $\epsilon_d$ is the relative dielectric constant.

*Electron Energy*

Electron energy can be lost or gained due to due to the flux of electrons to the wall or the secondary emission of electrons from the wall. The net electron energy flux to the wall $\vec{\Gamma_\epsilon}$ is obtained through the equation

$$\vec{\Gamma_\epsilon} \cdot \hat{n}_s = (2k_b T_e)\vec{\Gamma_e} - \sum_k e\Delta E_{\epsilon,k}\gamma_k \vec{\Gamma_k} \cdot \hat{n} \tag{2.1.24}$$

The first quantity is the energy per electron that is lost to the surface ($2k_b T_e$) due to the net electron species flux to the surface ($\vec{\Gamma_e}$). The second term takes into account the energy an electron acquires ($\Delta E_{\epsilon,k}$ in eV) when it is emitted from the surface due to secondary electron emissions.

### 2.1.2 Numerical Approach for Plasma Governing Equations

In this section we discuss the numerical techniques used to solve the plasma fluid equations. The plasma fluid equations are solved on an unstructured mesh framework using the finite volume method.

Each equation can be expressed as a scalar convection-diffusion equation with source terms. When solving vector-equations (e.g. momentum) each term in the vector is solved separately from the others. For finite volumes, the governing equation can be expressed in integral form as.

$$\frac{\partial}{\partial t}\int_V \phi dV = \int_{\delta V} (\vec{C}\phi - D\vec{\nabla}\phi)\cdot d\vec{S} = \int_V S dV, \tag{2.1.25}$$

where $\phi$ is the conserved variable of interest, $\vec{C}$ is the convective transport vector, D is the diffusion coefficient (expressable as a scalar or obtainable from a vector or tensor), and S is the source term. For the case of non-linear convection (e.g. the $\vec{\nabla}\cdot\vec{u}\vec{u}$ term in the fluid momentum) the equation is linearized by assuming the convection velocity is fixed and using the convection value from the previous time step. It is assumed that the conserved variable and the source terms are piece wise constant in each cell. The convective-diffusive fluxes are assumed to be constant over each separate cell face. The equation for each cell can subsequently be written as

$$\frac{\partial \phi_i}{\partial t}\Delta V_i = \sum_{f=1}^{N_f} (\vec{C}\phi - D\vec{\nabla}\phi)_f \cdot A_f \hat{n}_f + S_i \Delta V_i \tag{2.1.26}$$

.

where $N_f$ is the total number of cell interior and boundary faces, $A_f$ is the area of each face and $\hat{n}$ is the face unit outward normal vector.

Due to the stiffness of the plasma fluid equations, the different equations are solved in a decoupled manner where each solution variable (the potential, the densities and the temperatures) are updated separately. This allows different time steps to be used for each of the equations dependent on stability criterion for each criterion $min(\frac{\Delta x}{|\vec{C}|}, \frac{\Delta x^2}{D})$. As each equation is solved, the solution variable is updated and used by the subsequent equations (e.g. first the electrostatic potential is updated, then the electron density, then the electron thermal energy, then the ion species, the neutral species, and finally the heavy species thermal energy).

#### 2.1.2.1 Flux Discretization

The convective and diffusive flux terms must be calculated at cell faces. One of the challenges in solving plasma numerical is that number densities in adjacent cells can vary by several orders of magnitude. A common approach to discretizing the species density face fluxes for the plasma fluid equations is to use the Scharfetter-Gummel scheme [91]. This first order scheme combines the convective and diffusive flux by using the left and right cell variables, $\phi_L$ and $\phi_R$, and from the value of the convective and diffusive transport variables at the face, $\vec{C}$ and D fits the 1-D convection-diffusion solution to all points between the left and right cell center. The value of the flux at the face is then taken to be the value from the convection-diffusion equation solution at

the face. Other schemes that can be used include simple upwinding and other schemes discussed in the book by Patankar [80].

#### 2.1.2.2 Implicit Time Integration

For equations where the unsteady term is included (e.g. species continuity and the energy equations), time integration is performed using a backward Euler scheme. The new time is denoted by $t_{j+1}$, the previous time by $t_j$ and the time step size by $\Delta t$

$$\phi_i^{t_{j+1}} \frac{V_i}{\Delta t} = \phi_i^{t_j} \frac{V_i}{\Delta t} + \sum_{f=1}^{N_f} (\vec{C}^{t_j} \phi^{t_{j+1}} - D^{t_j} \vec{\nabla} \phi^{t_{j+1}})_f \cdot A_f \hat{n}_f + S(\phi)_i^{t_{j+1}} + S_i^{t_j} \quad (2.1.27)$$

The above equation can be written out as an Ax=b linear system for all the cell center solution variables $\phi$. Different terms can be treated implicitly if they are a function of the solution variable by taking their value at $t_{j+1}$ and shifting them to the A matrix (left hand side). Terms that are on the right hand side of the linear system (the b vector) are said to be explicit.

The combined convective-diffusive flux, $\vec{C}\phi - D\vec{\nabla}\phi$ can be expressed as a function of the cell center solution variables of the adjacent cells when using the Scharfetter-Gummel or upwind scheme. The flux terms are treated implicitly by setting their time value to $t_{j+1}$ and shifting the flux to the left hand side of the equation. The values of the transport variables $\vec{C}$ and $\vec{\nabla}\phi$ from the previous time step $t_j$ are used.

If the source term is linearly dependent on the solution variable or can be linearized, it can be moved to the left hand side of the equation and treated implicitly. This is done when the addition of the source terms to the left hand side A matrix increases the diagonal dominance of the matrix. In practice, the chemistry destruction term is linearized and treated implicitly while chemistry production source terms are treated explicitly (right hand side b vector).

In addition to treating the convection-diffusion flux and source terms implicitly, some boundary conditions can be treated in an implicit manner. This allows the boundary flux contribution to be added to the diagonal of the A matrix to increase the diagonal dominance of the linear system. A notable example is the surface flux boundary condition of the electron energy equation. By treating the Maxwellian thermal flux term $\frac{1}{4} n_e \sqrt{\frac{8 k_b T_e}{\pi m_e}}$ implicitly, it can be moved to the LHS of the equation. For problems where the discharge is sensitive to the wall boundary, the stability of the equation can often be improved allowing larger time steps taken.

#### 2.1.2.3 Semi-Implicit Poisson Equation

All the governing equations (electrostatic potential, species densities, species energies) are solved in a segregated matter as separate, decoupled linear systems. In reality however, the electrostatic potential, electron density and electron energy equations are closely coupled due to the dependence of the electric field on the charge distribution and vice versa.

The numerical time step is limited either by the cell CFL number

$min(\frac{\Delta x}{|\vec{C}|}), \frac{\Delta x^2}{D}$, or by the dielectric relaxation time of the plasma $\frac{\epsilon}{\sigma}$ where $\sigma$ is the conductivity of the plasma. The relaxation time is dependent on the coupling between the electrostatic potential equation and the electron density source term and is the characteristic time that it takes for a perturbation in the electron densities to relax back to equilibrium.

The dielectric relaxation time constraint can be partially alleviated by using a semi-implicit approach to re-couple the electrostatic potential equation with the electron species equation. The system of equations is made semi-implicit by using a predictor step for the electron densities in the source term of the Poisson equation, as shown in the equation below.

$$\sum_{f=1}^{N_f} \epsilon_r \vec{E} \cdot A_f \hat{n}_f = \frac{e}{\epsilon_0}(\sum_k Z_k n_k^{t_j} - n_e^{t_{j+1}}) \tag{2.1.28}$$

The electron predictor step can be written out as

$$n_e^{t_{j+1}} = n_e^{t_j} - \frac{\Delta t}{\Delta V} \sum_{f=1}^{N_f} (\mu^{t_j} n_e^{t_j} \vec{E}^{t_{j+1}} - D^t \nabla \vec{n}_e{}^{t_j})_f \cdot A_f \hat{n}_f + \Delta t \dot{G}_k{}^{t_j} \tag{2.1.29}$$

and then substituted back into the Poisson equation to yield

$$\sum_{f=1}^{N_f} (\epsilon_r - \frac{\Delta t}{\Delta V} \mu^{t_j} n_e^{t_j}) \vec{E}^{t_{j+1}} \cdot A_f \hat{n}_f = \frac{e}{\epsilon_0}(\sum_k Z_k n_k^{t_j} - n_e^{t_j}) - \frac{e}{\epsilon_0}(\frac{\Delta t}{\Delta V} \sum_{f=1}^{N_f} D^{t_j} \nabla \vec{n}_{ef}{}^{t_j} \cdot A_f \hat{n}_f + \Delta t \dot{G}_k{}^{t_j}) \tag{2.1.30}$$

Note that this effectively modifies the diffusion coefficient of the original Poisson equation with the addition of the electron mobility flux terms. This in turn, increases the diagonal dominance of the A matrix of the linear Ax=b system of equations which increases the stability of the numerical solution. In practice, using the semi-implicit approach enables the numerical time step to be increased by as many as one to two orders of magnitude.

### 2.1.3 Linear Solver

Each governing equation forms a linear Ax=b system which must be solved at each time step. In general, the A matrix is sparse and non-symmetric. The linear system is solved using the Portable Extensible Toolkit for Scientific Computing (PETSc) software library [10]. Options exist to use iterative Krylov solver methods such as Conjugate Gradient and Generalized Minimum Residual (GMRES) or sparse direct solvers such as SuperLU Distributed and MUMPS.

#### 2.1.3.1 GMRES with pre-conditioning

The default linear solver of choice used to solve the linear equations in this study was GMRES with block Jacobi preconditioning. A detailed discussion of the algorithm and how it works can be found in the book by Saad [89]. The basic approach is to search for an approximate solution $x^*$ to Ax=b in an orthogonal subspace V of the Krylov space $K_m = x, Ax, A^2, A^3x, ...A^{m-1}x$ of A where m is the number of search directions, n is the size of the marix and m

$<$ n. Search directions are generated in the Krylov space by orthogonalizing each search direction with the previous search directions and storing them using either the Gram-Schmidt or modified Gram-Schmidt algorithm. The system of orthogonal vectors from the Krylov space form the column of a matrix V. The solution vector is then written as a linear combination of the search vectors $x^* = Vy$. The best solution in the sub-space of orthogonal direction vectors is then found by minimizing the error of the solution residual $r = b - Ax_n$ in the $L_2$ norm and finding the weighting vector y. A single iteration consists of generating the search vector $Ax^n$ (requiring matrix-vector multiplications) followed by orthogonalizing the vector with all previous search direction vectors (requiring vector dot products) and then finding the vector that minimizes the $L_2$ norm of the residual. The process is repeated until the residual error falls under a specified tolerance. The default tolerance used for all simulations in this work is $10^{-6}$ of the final residual vector $(b - Ax^*)$ with respect to the initial residual vector.

Multiple factors influence the rate of convergence of the GMRES algorithm. The most important factor influencing the rate of convergence is the choice of pre-conditioner. Choices include simple pre-conditioners such as block Jacobi to more advanced pre-conditioners such as incomplete lower-upper factorization. In this work, block Jacobi was used as the default pre-conditioner for all parallel computing results reported here but other choices exist for parallel such as the Additive Schwarz method (ASM). By default, left preconditioning is used.

Besides the choice of pre-conditioner, other factors can influence the rate of convergence. Each new search direction must be orthogonalized with respect to all previous search directions so they must all be stored in memory and the algorithm will take longer as more vectors are found. In practice, only a certain number (the default for PETSc is 30) of search vectors are stored. After that number has been reached, the algorithm will be restarted and the last search vector will be used as an initial guess vector and a new set of orthogonal vectors will be generated in reference to that vector. The choice of how many search directions to store before restarting will impact the rate at which the algorithm converges. The choice of orthogonalization algorithm (regular or modified Gram-Schmidt) also impacts the convergence rate of GMRES. The PETSc user manual indicates that regular Gram-Schmidt is faster but modified Gram-Schmidt can be more stable. Finally, the specified tolerance of the error in the residual (relative error in the residual) will impact how many search iterations the solution takes to converge.

#### 2.1.3.2 Direct Solvers

PETSc can interface with several parallel direct solver software packages. For this work, the SuperLU Distributed [51] and MUMPS (MUltifrontal Massively Parallel Solver) [9] software packages were also investigated. Both packages can be solved in parallel on distributed memory systems. They are interfaced with PETSc by being applied as exact left pre-conditioners. Either solver is used to generate the exact inverse matrix $A^{-1}$ which is then applied

to the Ax=b linear system as single solve iteration.

## 2.2 Navier-Stokes Governing Equations

The Navier-Stokes equations are a coupled set of equations consisting of mass conservation, momentum conservation and energy conservation. For simulations in this work, the Navier-Stokes equations are solved in two-dimensional Cartesian or axisymmetric form as described in the book by Blazek [13].

The two-dimensional Navier-Stokes equations can be expressed in integral form as

$$\int_V \frac{\partial U}{\partial t} dV + \int_{\delta V} (\vec{F_i} - \vec{F_v}) \cdot \vec{n} dA + \int_V S dV \tag{2.2.1}$$

For some problems, (e.g. a stagnation flow jet) it is practical to use the axi-symmetric form of the Navier-Stokes equations

$$\int_V \frac{\partial U}{\partial t} dV + \int_{\delta V} (\vec{F_i} - \vec{F_v}) r \cdot \vec{n} dA = \int_V S dV \tag{2.2.2}$$

,

where r is the radial distance of the cell from the axis of symmetry.

The vector of conserved variables, U, is

$$U = \begin{pmatrix} \rho \\ \rho u \\ \rho v \\ \rho E \\ \rho Y_1 \\ ... \\ \rho Y_{N-1} \end{pmatrix} \tag{2.2.3}$$

The variables are the density $\rho$, the flow velocity u and v, the energy per unit mass E, and the mass fraction of species i, $Y_i$. It is assumed that the different species of interest can be treated as calorically perfect gasses. The energy per unit mass can be written in terms of the primitive flow variables as $E = \frac{P}{\rho(\gamma_a - 1)} + \frac{1}{2}(u^2 + v^2)$ and $\gamma_a = \frac{\sum_{i=1}^{n} Y_i C_{p,i}}{\sum i{=}1^n Y_i C_{\nu,i}}$ is the ratio of the mass averaged constant pressure over constant volume specific heats. For n species there will be n-1 mass fraction equations that are solved. The mass fraction for the last species, n, is found using the equation $Y_N = \rho - \rho \sum_{i=1}^{N-1} Y_i$.

The inviscid flux term $\vec{F_i}$ is written below

$$\vec{F_i} = \begin{bmatrix} \rho u \\ \rho u^2 + P \\ \rho u v \\ (\rho E + P)u \\ \rho u Y_i \\ ... \\ \rho u Y_{N-1} \end{bmatrix} \hat{x} + \begin{bmatrix} \rho v \\ \rho v u \\ \rho v^2 + P \\ (\rho E + P)v \\ \rho v Y_i \\ ... \\ \rho v Y_{N-1} \end{bmatrix} \hat{y} \tag{2.2.4}$$

The species mass fraction fluxes are simply the species mass flux multiplied by the species mass fraction. P is the gas static pressure. For the axi-symmetric case x is the axial coordinate and y is the radial coordinate.

The viscous flux term $\vec{F}_v$ is written out below

$$\vec{F}_v = \begin{bmatrix} 0 \\ \tau_{xx} \\ \tau_{xy} \\ \theta_x \\ \rho D_i \frac{\partial Y_1}{\partial x} \\ ... \\ \rho D_{N-1} \frac{\partial Y_{N-1}}{\partial x} \end{bmatrix} \hat{x} + \begin{bmatrix} 0 \\ \tau_{yx} \\ \tau_{yy} \\ \theta_y \\ \rho D_i \frac{\partial Y_1}{\partial y} \\ ... \\ \rho D_{N-1} \frac{\partial Y_{N-1}}{\partial y} \end{bmatrix} \hat{y} \tag{2.2.5}$$

The viscous stresses can be found using the formula $\tau_{i,j} = \mu(\frac{\partial x_i}{\partial x_j} + \frac{\partial x_j}{\partial x_i}) + \lambda \delta_{ij} \vec{\nabla} \cdot \vec{V}$ where  is the coefficient of viscosity and  is the bulk viscosity coefficient. Stokes theorem is used to express the bulk viscosity term as $\lambda = -\frac{2}{3}\mu$. For the axi-symmetric case x is the axial coordinate and y is the radial coordinate.

The viscous energy flux terms $\theta_x$ and $\theta_y$ can be expressed as $\theta_i = u\tau_{x,i} + v\tau_{i,y} + k\frac{\partial T}{\partial x_i} + \sum_{k=1}^{N} \rho h_k D_k \frac{\partial Y_k}{\partial x_i}$. The coefficient $D_k$ is the diffusion coefficient of species mass fraction k into the total mixture and there are N total species.

The final term in the Navier-Stokes system of equations is the source term due to the plasma and electric fields. The discharge affects the flow kinetics via gas heating and electrostatic forcing.

$$S = \begin{bmatrix} 0 \\ f_x \\ f_y \\ S_{T_g} + \vec{f}_{ES} \cdot \vec{V} \\ 0 \\ ... \\ 0 \end{bmatrix} \tag{2.2.6}$$

The electrostatic forcing due to the electric field acting on the ions are accounted for as the terms $f_x$ and $f_y$. The heavy species energy is modified due to ion Joule heating and collisional heating from electron impacts which is accounted for by the term $S_{T_g}$ from the plasma bulk energy equation. The electrostatic forcing term, $\vec{f}_{ES} \cdot \vec{V}$ due to the electric field can add or remove energy from the ionized heavy particles. It is assumed that the bulk flow species that are solved for are chemically inert and finite rate chemistry is not accounted for during the flow solver integration.

When solving the Navier-Stokes in axisymmetric form, the additional term $\frac{P}{r}$ in the radial (r-direction) momentum equation appears due to taking the divergence of the pressure tensor in cylindrical coordinates.

### 2.2.1 Boundary Conditions

There are two types of boundary conditions of interest: natural boundaries such as solid walls and artificial boundaries such as inflow and outflow boundaries. Boundary conditions are applied using the concept of ghost cells, a layer of cells located adjacent to the domain boundaries. Instead of applying boundary conditions directly to the boundary faces, the conservative variables are specified in the ghost cells and the boundary fluxes are evaluated using the same discretization schemes used to evaluate the interior cells. Ghost cell variables are indicated by the subscript g (e.g. $u_g$) while interior cell variables are indicated by the subscript i (e.g. $u_i$).

#### 2.2.1.1 Solid Surfaces

All physical boundaries are assumed to be viscous boundaries, and are governed by the imposition of a no-slip boundary condition.

$$u = v = w = 0.0 \tag{2.2.7}$$

This condition is applied to the boundary face by setting the velocity components in the ghost cell to be equal and opposite to the velocities in the neighboring interior cell, e.g.

$$u_g = -u_i, v_g = -v_i, w_g - w_i \tag{2.2.8}$$

The pressure at the wall $P_w$ is set by assuming that the gradient of pressure normal to the boundary is zero. This can be applied by setting the ghost cell pressure to be equal to the interior cell pressure

$$P_g = P_i \tag{2.2.9}$$

Finally, the wall can be modeled as either an adiabatic (zero energy flux) boundary or as a constant temperature surface.

*Adiabatic Wall*

If the wall is specified as adiabatic, then the gradient of temperature at the wall is zero. This boundary condition can be imposed simply by setting the ghost cell temperature equal to the interior cell temperature

$$T_g = T_i \tag{2.2.10}$$

Note that this also implies that the ghost cell density is equal to the interior cell density via the ideal gas law.

*Constant Temperature Wall*

If the wall temperature is specified, then in general there will be a non-zero temperature gradient normal to the wall. The ghost cell temperature is specified by first determining the gradient of temperature between the interior cell center and the boundary face center assuming the boundary face temperature is the specified wall temperature. Once the gradient is known, a ghost cell center temperature is specified such that the gradient between the interior cell and the ghost cell centers is the same as the gradient between the interior cell center and the boundary face center.

The ghost cell density is found using the calculated ghost cell temperature, the ideal gas law and the assumption that the ghost cell pressure is identical to the interior cell pressure

#### 2.2.1.2 Inflow and Outflow Boundaries

Inflow and outflow boundaries are imposed using characteristic based boundary conditions and ghost cells. In general, the Navier-Stokes equations will have five different wave characteristics and wave speeds determined from the eigenfunctions and eigenvalues of the convective flux Jacobian. Depending

on the Mach number and direction of the flow, one or more characteristics will go into or out of the domain.

*Supersonic Inflow and Outflow*

For supersonic flow, all the flow characteristics travel in one direction. For an inflow boundary all the characteristics flow into the domain and the boundary condition can be specified by specifying all five conserved variables and the inflow mass fractions at the ghost cell.

For supersonic outflow, all characteristics flow out of the domain, and the ghost cell conserved variables are assumed to be the same as the variables of the interior cell located adjacent to the ghost cell.

*Subsonic Inflow and Outflow*

For flow that is subsonic, four of the flow characteristics will propagate in one direction and one characteristic will propagate in the other direction. This implies that four flow variables will be specified on one side of the boundary while the fifth flow variable will be interpolated from the other side.

For subsonic inflow, four primitive variables (the density and velocities) are specified at the ghost cell. The fifth variable, pressure is interpolated from the interior cell assuming zero pressure gradient (e.g. $P_g = P_i$).

For subsonic outflow, a pressure is specified for the far field and imposed in the ghost cell. The remaining four variables (density and the velocities) are set equal to the interior cell density and velocities.

### 2.2.2 Numerical Approach for Flow Model

The compressible Navier-Stokes equations are solved using a finite volume schemes on an unstructured, mixed mesh. The system of equations for finite volumes is written out below and consists of cell volume averaged unsteady and source terms combined with flux terms evaluated at cell faces. Variables with bar denote cell averaged values.

$$\frac{\partial}{\partial t}\bar{U}V_i = \sum_{f=1}^{N_f} \vec{F_i} \cdot A_f \hat{n}_f = \sum_{f=1}^{N_f} \vec{F_v} \cdot A_f \hat{n}_f + \bar{S}V_i \tag{2.2.11}$$

#### 2.2.2.1 Discretization in Space and Time

The inviscid flux terms (velocity and pressure) are discretized in the interior domain of the simulation using a first order advection upwind splitting method (AUSM) scheme. The main idea behind the scheme is to treat the velocity and pressure flux terms separately. For a detailed discussion of the AUSM scheme refer to [54], while for a general overview of AUSM and other flux schemes refer to the book by Blazek [12]. Viscous fluxes are discretized in space using central differences or the method of Haselbacher and Blazek (refer to [41]).

Time integration is performed using explicit dual time stepping with local time steps for each cell. A fourth order Runge-Kutte scheme is used to advance the solution in pseudo time.

#### 2.2.2.2 Evaluation of Boundary Conditions

When evaluating boundary conditions, a ghost cell approach is used. The primary idea is to specify values in the ghost cell and evaluate the flux at the face using the same flux discretization scheme used to evaluate the interior cell face fluxes.

For open boundaries such as inflow and outflow, primitive variables such as density, temperature, velocity and pressure are specified. A characteristic based approach is used dependent upon whether the velocity at the face is subsonic or supersonic. For supersonic flow, the primitive variables at the upwind cell are used to evaluate the flux at the face. If the flow is subsonic, four variables are specified at the ghost cell and a fifth primitive variable (pressure) is interpolated based on the value at the interior.

For solid walls, the ghost cell velocity, pressure and density are specified such that the velocity at the face is zero and there are no density/pressure gradients. For temperature, an adiabatic (zero heat flux) or constant temperature boundary condition can be specified.

## 2.3 Plasma-Flow Coupling

The characteristic timescales of the phenomena governing the plasma discharge formation and flow kinetics vary by several orders of magnitude. Each set of equations is solved separately using separate time steps sizes characterized by stability criterion (e.g. CFL number) for the equations of interest.

Typically, the plasma time steps are several orders of magnitude smaller than the flow time steps. For example, the electron plasma time step is typically on the order of picoseconds ($10^{-12}$) while the flow time steps are on the order of microseconds ($10^{-6}$). Thus, there can be many plasma time steps during which the plasma governing equations are solved between each solution of the flow governing equations. In practice, there are typically 100-1000 plasma solve time steps between each flow solve time step.

The plasma governing equations and Navier-Stokes flow governing equations are weakly coupled. The plasma governing equations affect the flow kinetics via the inclusion of electrostatic forcing and heating source terms. The heating source terms are due to Joule heating of ions and collisional heating of the background species by the much hotter electrons. The forcing source terms are due to the electrostatic force imparted on the ion species which in turn collide with the neutral background particles imparting momentum. The plasma governing equations are affected by the flow kinetics due to the change in the background gas pressure, mole fraction concentration and bulk velocity.

The solution process can be thought of as a cyclical process where the flow and plasma equations are solved in series, each updating the set of variables required by the other. First the background pressure, mole fractions and velocity field are updated by the flow solver. The plasma solver then uses those values for the next 100-1000 electron plasma time steps assuming the flow is frozen at those values. The plasma heating and electrostatic forcing terms are then passed to the flow solver which then solves for the updated pressure,

mole fraction and velocity fields. The entire process is then repeated.

# Chapter 3

# Scaling and Grid Resolution

## 3.1 Parallel Scaling

Both the plasma solver and compressible Navier-Stokes solvers are parallelized using a domain decomposition approach. The numerical mesh is partitioned among the different processors using ParMetis and solved in parallel with communication between the processors using MPI communication. It is of interest to determine how the codes scale as the number of processors increases. For the scaling studies presented herein, only the plasma solver is considered as it is the most expensive of the two solvers from a computational standpoint.

### 3.1.1 Strong Scaling

Strong scaling is a measure of the parallel performance of a code in which the size of the problem (total mesh cell count) is held fixed while the number of processors is increased. The strong scaling study was performed using the same 80,000 cell mesh presented for the atmospheric pressure plasma jet study presented in chapter 6 for atmospheric pressure plasma jets. All scaling simulations were for 500 numerical time steps and the number of processors was varied from 1 to 720.

The simulations were performed on the Lonestar supercomputer in the Texas Advanced Computing Center. The Lonestar supercomputer consists of 1,888 compute nodes each of which has two Xeon Intel Hexa-Core 64-bit Westmere processors at 3.33 GHz with 6 cores per processor for a total of 12 cores per node.

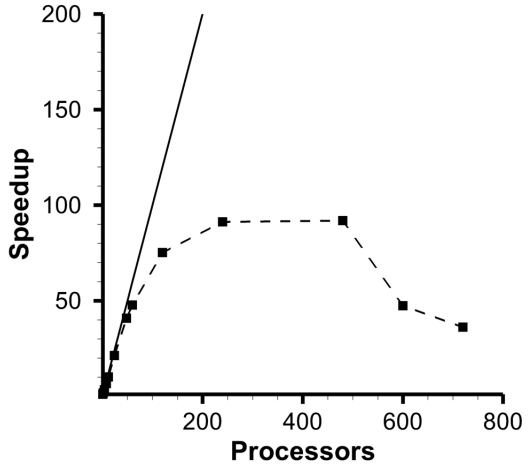


Figure 3.1: Strong scaling speedup after 500 iterations on an 80,000 mesh.

From Fig. 3.1 it can be seen that the given problem scales well up to approximately 100 processors. After 200 processors the speedup curve levels out and after 400 processors speedup drops significantly.

It is possible to consider individual sections of the code and look at how they scale. The most computationally expensive operations performed by the plasma solver include : the assembly and solution of the Poisson equation, the assembly and solution of the electron density and energy equations, and the calculation of the gas chemistry kinetics. The relative computational cost of

these different computations is shown in Fig. 3.2.

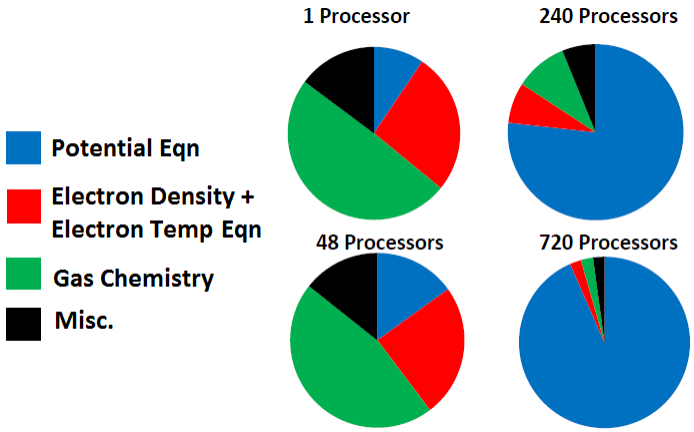


Figure 3.2: Comparison of relative solve time of plasma numerical solver calculations for 500 iterations on an 80,000 mesh for 1, 48, 240 and 720 processors.

For a single processor, it can be seen that the calculation of the finite rate gas chemistry is the most expensive calculation requiring almost half the computation time. When the number of processors is increased to 48, the relative costs of the different computations remains approximately the same. When the number of processors is increased to 240 and 720 respectively, the numerical solution solve time is dominated by the time required to assemble and solve the Poisson equation.

The speedup scaling curves are plotted in Fig. 3.3 comparing the speedup of the Poisson equation, electron density/temperature, gas chemistry and the total speedup.

Although gas chemistry is initially the most expensive computation, it scales almost linearly even up to 720 processors because no communication is

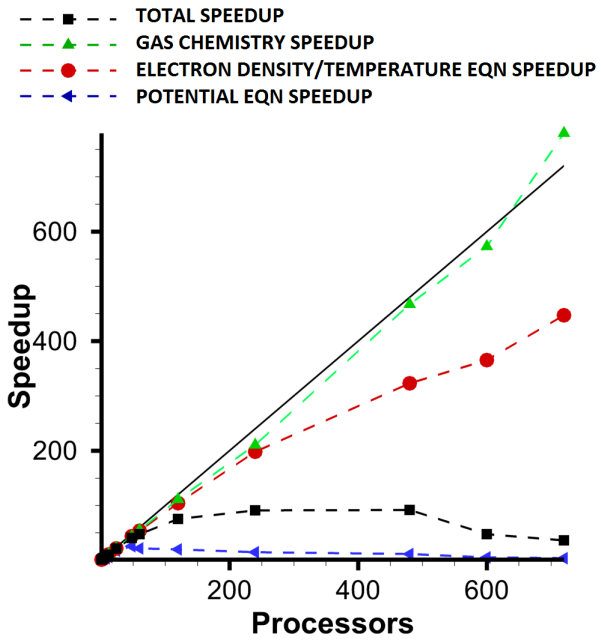


Figure 3.3: Comparison of strong scaling of different plasma solver calculations for 500 iterations on an 80,000 mesh.

required at cell faces (e.g. chemistry is localized to individual finite volume cells).

The electrostatic Poisson equation on the other hand requires multiple communications at processor boundaries for the electron predictor step when assembling the A matrix and b vector. When solving the linear system with GMRES, typically 500 iterations or more are required to achieve convergence each time step. Each iteration involves matrix vector multiplications and dot products in parallel. The resulting communication costs required for both the matrix assembly and iterative solver solution of the Poisson equation result in significant slowdown above 200 processors.

The electron density and electron temperature equations are somewhat similar to the Poisson equation in that they require assembly of an A matrix and b vector as well as solving the system iteratively using GMRES. The amount of data that must be communicated across the processors is lower for these equations and in practice they both converge in 1-2 iterations each time step resulting in much better scaling from 1 to 720 processors.

Typically, the Poisson linear system of equations can take several hundred iterations to converge (with a tolerane of $10^{-6}$) when using GMRES with block Jacobi preconditioning. A different preconditioner (additive Schwarz) and two different direct solvers (SuperLU and MUMPS) were used to solve only the Poisson linear system to determine if speedup could be improved. All other governing equation linear systems used GMRES with the default setting

The left side of Fig. 3.4 compares the speedup of the Poisson equation when using GMRES with block Jacobi and ASM preconditioners as well as when using two different direct solver packages (SuperLU Distributed Memory and MUMPS). In addition, the total time (in seconds) required just for the solution of the assembled linear system for the different solver options is shown on the right in Fig. 3.4.

It can be seen that MUMPS is faster than GMRES for the Poisson solve. It should also be noted that even at low processor counts (serial) that the solve time required by MUMPS is many orders of magnitude lower than the other options. Consequently, it appears that when the iteration count required by GMRES is large ($> 500$) it may be practical to use a sparse direct

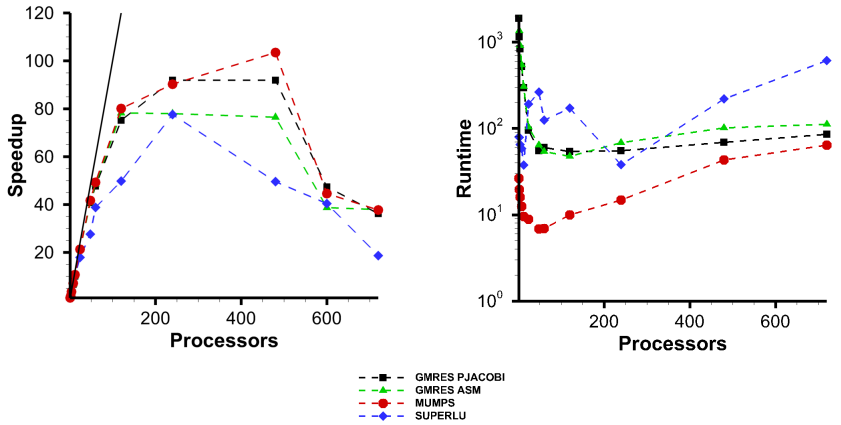


Figure 3.4: Comparison of the total problem speedup using different solver options (LEFT) and the computation time in seconds required to solve the Poisson linear system (RIGHT).

solver. One option would be to dynamically choose the linear solver based on the number of iterations and allow the solver to switch over to MUMPS when the iteration count for GMRES is large (e.g. $> 500$). Another option would be to find a good pre-conditioner that is scalable to large numbers of processors.

### 3.1.2 Weak Scaling

Weak scaling is a measure of the parallel performance of a code in which the size of the problem increases such that the amount of work per processor (number of cells solved on each processor) is held fixed. Fig. 3.5 compares the relative speedup (left) and solve time (right) of the different code components for 500 solver time steps. The problem size is fixed at 2000 cells per processor. The number of processors was varied from 1 to 192.

The three components compared are the Poisson equation, the com-

bined electron density and temperature equations, and the calculation of the finite rate chemistry calculations. It can be seen from the right side of Fig. 3.5 that the electron/density equations and gas chemistry solve times do not increase considerably as the number of processors is increased. The large increase in the solve time required by the Poisson equation is due to the large number of communications required as the number of processors and hence the number of communications required increase.

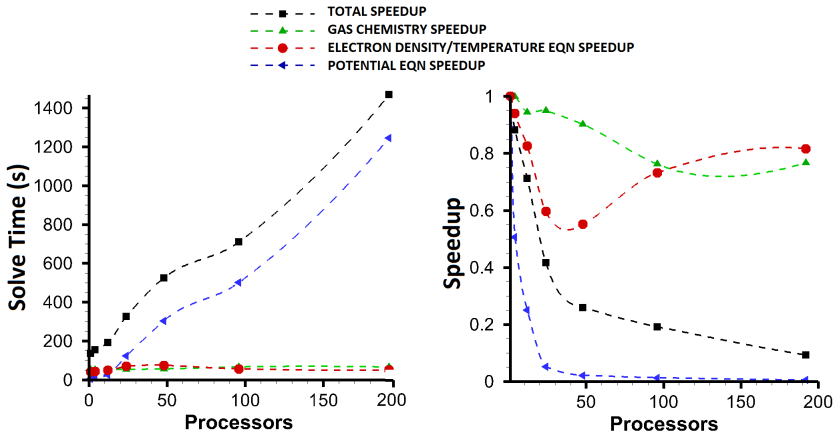


Figure 3.5: Comparison of the weak scaling performance of different code components as the overall size of the problem increases with the processor count. Weak scaling speedup relative to serial computation (LEFT). Weak scaling solve time required as problem size increases with processors (RIGHT).

From both the strong and weak scaling studies, it can be concluded that the current bottleneck to scaling the plasma solver to large numbers of processors is the assembly and solution of the Poisson equation.

## 3.2 Grid Resolution

The numerical methods used to solve the governing equations obtain an approximate solution that is defined at discrete locations in space. For finite volume methods, the domain of interest is discretized and a solution is obtained by solving for a cell averaged value which is associated with the cell center. At the same time, the flux of the solution variable at the cell faces must be computed in order to calculate the fluxes entering and leaving each cell. The discretization method used to obtain the cell flux at the faces when the solution variables are located at the cell centers will depend on the size of the cell, and the solution will change depending on how coarse or refined the mesh is. The purpose of this study is to determine how much of an impact the mesh resolution has on the formation and propagation of the plasma discharge.

### 3.2.1 Point-to-Plane Streamer in Air

The first mesh refinement test case presented is for a simple point-to-plane streamer in air. A sharp prong (point) is placed 5 mm from an infinite grounded plane. The gas in the gap region is assumed to be standard temperature and pressure air. A 30 kV square pulse is applied to the prong. It is assumed that the discharge is symmetric about the axis of the pin. Fig. 3.6 shows the simulated domain as a red dotted line. Three different meshes are compared: a coarse 6,250 cell mesh with a cell size of 40 microns up to a fine 100,000 cell mesh with a cell size of 10 microns.

The solution for the different mesh resolutions are compared by look-

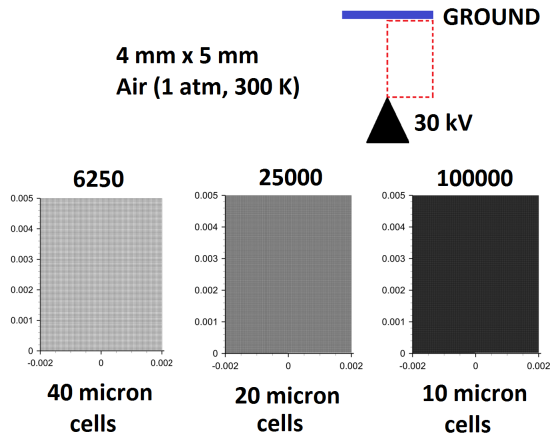


Figure 3.6: A sample streamer problem between a point located at the bottom and a plane located at the top of the mesh. The different meshes correspond to 6,250 cells (40 micron cell), 25,000 cells (20 micron cell) and 100,000 cells (10 micron cell).

ing at the electron impact production rate. Fig. 3.7 compares the electron production rates in the streamer head between one and five nanoseconds for the different meshes. From the images it can be seen that the streamer propagation speed is impacted by the mesh coarseness. The streamer propagation speed is dependent on the production rate of electrons in the streamer head which is dependent on the electric field. Coarsening the mesh introduces numerical dissipation which smears the electrostatic potential gradient (electric field) which is why the streamer speed and peak electron production rates are lower on coarse mesh. The structure of the streamer is not significantly impacted by the mesh resolution, and the spatial distribution of the production rate and the streamer radius are nearly the same for all cases.

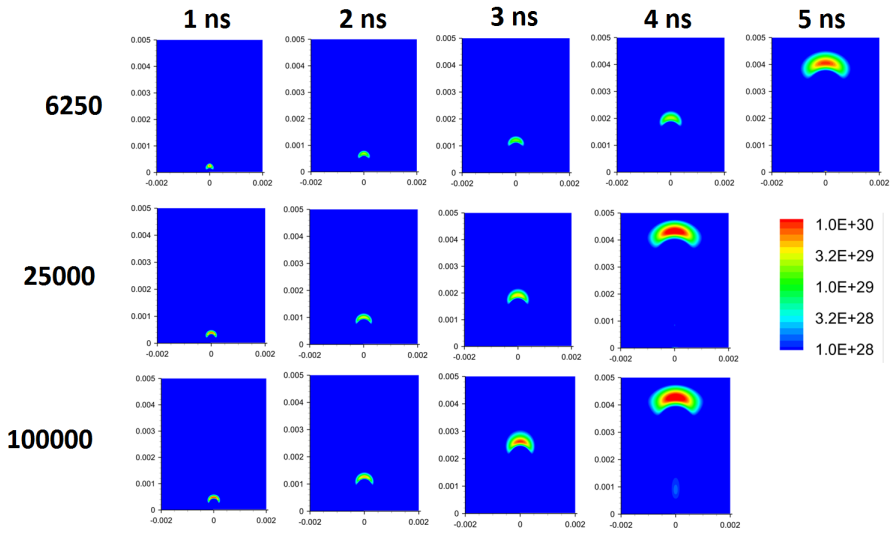


Figure 3.7: Comparison of electron production rates in streamer head for 6250 mesh (TOP), 25,000 mesh (MIDDLE) and 100,000 mesh (BOTTOM).

### 3.2.2 Atmospheric Pressure Plasma Jet

The second mesh refinement test case is for the atmospheric pressure plasma jet simulations which are presented in chapter 6. The default mesh used for the simulations presented in this work consists of 80,000 cells with cell sizes varying from 20 to 50 microns in the region of the plasma. To determine the impact of mesh refinement, a simulation was performed on a 600,000 cell mesh with a uniform cell size of 10 microns in the vicinity of the discharge region.

Fig. 3.8 compares the electron production rate for the coarse (80k) and refined (600 k) mesh. The streamer propagation speed increases on the refined mesh, but the overall structure is comparable for both cases which indicates

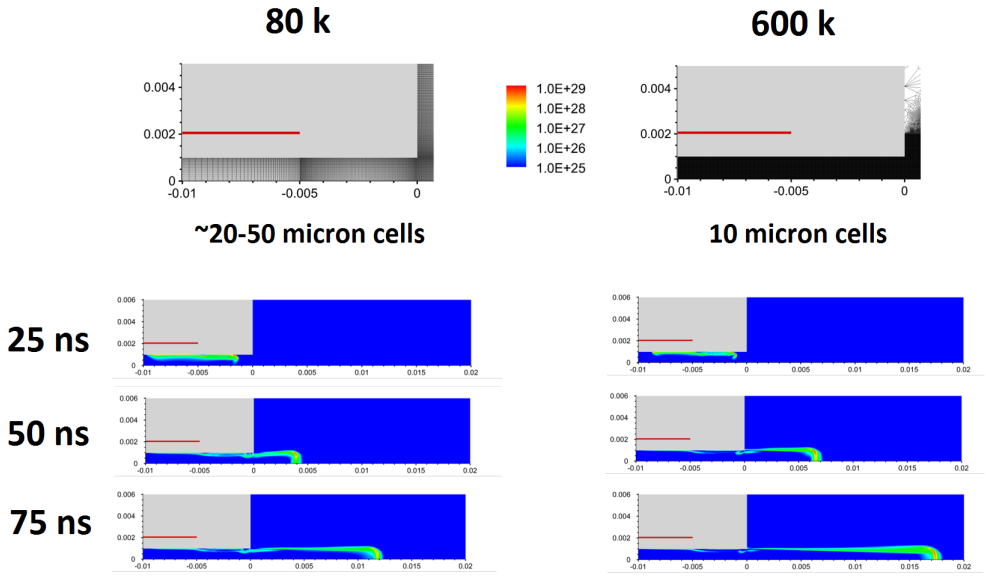


Figure 3.8: Comparison of electron production rates in streamer head for 80,000 mesh (LEFT) and 600,000 mesh (RIGHT).

that the default 80k mesh is adequate to capture the physics of the plasma jet.

# Chapter 4

# Supersonic Ignition and Aerodynamic Flow Actuation

The goal of this study is to provide a comprehensive understanding of the plasma dynamics, radical production, and gas heating mechanisms in a single nanosecond pulse applied to a premixed supersonic flow stream. The non-equilibrium plasma solver is coupled with the compressible Navier-Stokes solver to capture the combined plasma-flow kinetics. The simulations utilize a detailed high pressure $O_2$-$H_2$ chemistry to model the production of combustion enhancing species such as ground-state O atoms and excited metastables of O and $O_2$ at different pulse voltages and polarities. Simulations in pure argon under identical geometry, flow, and pulsing conditions are also performed to elucidate the effect of chemistry on discharge phenomena.

## 4.1 Discussion of Chemistry

### 4.1.1 Oxygen-Hydrogen Plasma Chemistry

A detailed oxygen-hydrogen plasma reaction mechanism consisting of 16 species: electrons, $O_2$, $H_2$, O, H, OH, $O^+$, $O_2^+$, $O_4^+$, $O^-$, $O_2^-$, $H^+$, $H_2^+$, $O(^1D)$, $O_2(a^1{}_g)$ and $O_2(b^{1+}_g)$, is used in this work. The mechanism consists of 87 reversible and irreversible reactions which include electron ionization, elec-

tron dissociation, electronic excitation of metastables, attachment, ion-ion, ion-neutral, metastable quenching, as well as metastable and neutral combustion reactions (see Appendix B). The reaction rate coefficients of all activated electron-impact reactions were calculated using an offline Boltzmann solver, BOLSIG+ [40] using cross-section data compiled by [42], and tabulated as a function of the mean electron temperatures. The remaining rate coefficients were compiled from a variety of sources and are shown in Appendix B.

Reactions G5-G11 account for energy lost due to rotational, vibrational and electronic excitation of oxygen and hydrogen. The relaxation rates for vibrational and the electronically excited oxygen and hydrogen are much greater than the nanosecond time scales of a single pulse and therefore all electron energy that goes into vibrational and electronic excitation (G6, G7, G8, G10, G11) is lost to convection. The exception is the excitation of metastable species where energy transfer is taken into account by separate excitation and quenching reactions. It is assumed that rotationally excited oxygen and hydrogen are immediately de-excited and return their energy to the bulk gas. Metastable and ion quenching can contribute to inelastic collisional heating of the background gas which is modeled by including separate reaction rates for metastables and ions with neutral species. Note that although combustion reactions are included, exothermic heat release in neutral reactions is not explicitly modeled since these reactions occur on time scales much larger than the nanosecond pulsed discharge phenomena. Consequently, the gas heating seen in the results section is due entirely to plasma chemical reactions.

The primary focus is to accurately model the production of radical and metastable species during the plasma discharge event. Most experiments of nanosecond pulse plasmas for ignition enhancement investigate formation of combustion enhancing radicals such as O, H, and OH. Other experiments such as [16] [103] and numerical simulations such as [17] have investigated the effects of metastables on combustion enhancement, primarily the oxygen metastables $O(^1D)$, $O_2(a^1{}_g)$, and $O2(b^1{}_g^+)$. The metastables are modeled as separate species (see Appendix A) while the higher energy electronically excited states such as the Herzberg state (4.5 eV) are combined into the reaction rates $G_7$ and $G_8$ and act to remove energy from the electrons.

Combustion species such as $H_2O$, $H_2O_2$, and $HO_2$ are not produced in significant amounts during the short time scales of a nanosecond discharge. Therefore, all the combustion species except O, H and OH are neglected for the simulations performed in this work. To model the plasma itself, $O^+$, $O_2^+$, $O_4^+$, $O^-$, and $O_2^-$ ions are included in the chemistry. From previous simulations it is known that $O_2^+$ is the dominant ion in the plasma. $O_4^+$ is produced by three-body reactions involving $O_2^+$ and can be significant at higher pressures. Dissociative reactions are dominant at high E/N so reactions involving $O^+$ ions ware included. Oxygen discharges are typically electronegative and so $O^-$ and $O_2^-$ ions are included. Ion-neutral, ion-ion, metastable-ion and quenching reactions for all species have been included in addition to ionization reactions.

### 4.1.2 Argon Chemistry

The purpose of the argon simulations is to provide insights into nanosecond pulsed plasma discharge in the chemically inert argon gas and the chemically reactive $O_2$-$H_2$ mixture. The argon simulations utilize a high-pressure chemistry mechanism used in previous work to model micro-cavity discharges [27]. The mechanism consists of 6 species and 14 irreversible reaction rates tabulated in Appendix C.

## 4.2 Simulation Configuration

A configuration similar to that used in the experiments by the Mungal and Cappelli group at Stanford University is utilized for all simulations performed in this part of the work [31]. These experiments involved high voltage (10 kV) repetitive pulses of duration 10-20 ns applied at a pin electrode flush mounted on a flat plate with a parallel $O_2$-$H_2$ premixed free stream. A similar flat plate geometry representation in two-dimensional planar coordinates is used for our study. A planar pin electrode with a high ballast resistance (30 kilo-ohms) connected to the powered electrode is used in our work. The ballast resistance is required to limit the peak current draw in the simulation to tens of mA; necessitated primarily by numerical stability requirements.

Fig. 4.1 shows flow simulation results (without discharge) and the mesh representation for the simulations. Two contiguous subdomains are utilized for all simulations: a flow-only subdomain upstream of the electrode where only the flow equations are solved and a plasma-flow subdomain in the

region downstream of the flow-only subdomain where both plasma and flow equations are solved. The plasma-flow subdomain is 2.5 mm long, 0.5 mm high, and consists of 8,000 cells. It is centered on a single powered electrode that measures 0.2 mm in length along the flow direction. This split in the overall simulation domain is required because of the limited spatial extent of the plasma discharge compared to the flow. For all simulations, it is assumed that the grounded electrode is downstream of the powered electrode outside of the computational domain. For the short duration nanosecond pulse, it is found that the dielectric surface surrounding the powered electrode acts as a virtual grounded electrode and hence it is not necessary to explicitly model the grounded electrode.

For all flow simulations, a uniform incoming Mach 3 flow with a static pressure of 225 Torr (30 kPa) and static temperature of 300 K was fixed. The flow solver is used to obtain a steady-state flow over an adiabatic flat plate boundary. A laminar boundary layer forms as seen in Fig. 4.1. A leading edge oblique shock forms as the laminar boundary layer begins to develop on the plate. The boundary layer thickness at the location of the pin electrode is comparable in thickness to the flow-wise length of the electrode.

A 10 ns trapezoidal pulse with 2.5 ns rise and 2.5 ns fall time is applied for all test cases. The electrode is assumed to have a secondary electron emission coefficient of 0.015 corresponding to tungsten metal [52]. The wall is modeled as a thin dielectric layer with a thickness of 1 mm and a dielectric constant of 8.0. Secondary electron emission from the surface was completely neglected

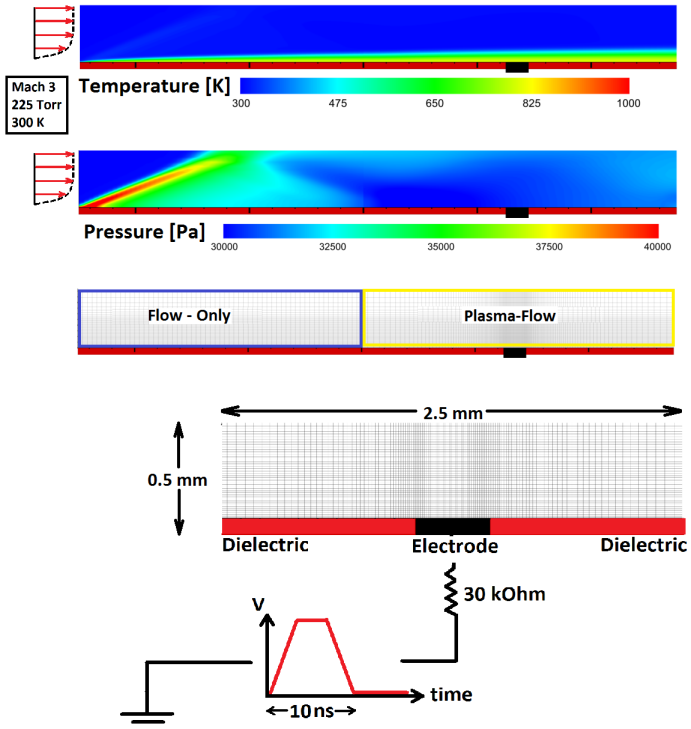


Figure 4.1: The top two images show temperature and pressure profiles in supersonic flow across the flat plate without the pulsed discharge. The bottom image shows the mesh utilized in the simulation and the external circuit configuration for powered electrode.

($\gamma = 0$). The gas boundaries are modeled using inflow/outflow boundary conditions and symmetry boundary conditions are used for the voltage. An initial seed electron density of $10^{14}$ $m^{-3}$ was assumed in the entire plasma domain and was chosen for all simulations performed.

## 4.3 Results

The nanosecond pulsed discharge in this study are characterized by formation of streamers. Several recent computational studies have modeled streamer discharges in air [79] [78] [47] [61] [73] including those for plasma actuator applications [111], [53]. Here the focus is on the production of combustion enhancing species and mechanics of gas heating in the discharge and its effect on the flow. Comparisons are made for different voltage polarities, different voltage magnitudes (4 to 8 kV), different chemistries ($O_2$-$H_2$ versus pure argon), and the effect of flow. Both anodic (positive) and cathodic (negative) pulse voltages are considered.

### 4.3.1 Voltage Polarity: $O_2$-$H_2$

#### 4.3.1.1 Plasma Formation

Figs. 4.2 and 4.3 illustrate the formation of the plasma, as indicated by the dominant $O_2^+$ ion densities and electron densities, respectively, at different time instances for a positive (anodic) and negative (cathodic) polarity pulses applied at the electrode. The pulse peak voltages are +4 kV and -4 kV for the anodic and cathodic pulse discharges, respectively. For the anodic pulse, two cathode-directed streamers are initiated at the electrode edges and propagate away from the powered electrode, parallel to the dielectric surface, but at a small distance away from the surface. The peak electron densities are localized to the propagating streamer heads with the ion densities tracing the path followed by the electrons. For the cathodic pulse, the discharge is

also initiated at the electrode edges. At the early stages of the pulse a pool of electrons rapidly drifts away from the cathode and deposits a negative charge on the dielectric surface (Fig. 4.3). The slower positive ions then follow the path of the electrons and propagate over the dielectric surface while being attracted by the negative charge on dielectric surface. The positive ions deposit a positive charge that neutralizes the existing negative charge from the initial electron propagation event. The cathodic pulse therefore behaves like a surface discharge. In addition to the dielectric surface discharge, two cathode-directed streamers are observed to form and begin propagating above the electrode towards the electrode center but are terminated quickly at the end of the pulse. Gas breakdown and plasma formation take place entirely within the fluid mechanical boundary layer, and the two discharges which form at the electrode edges are nearly symmetrical in both the upstream and downstream directions indicating that the flow does not affect plasma processes on the time scale of the pulse itself.

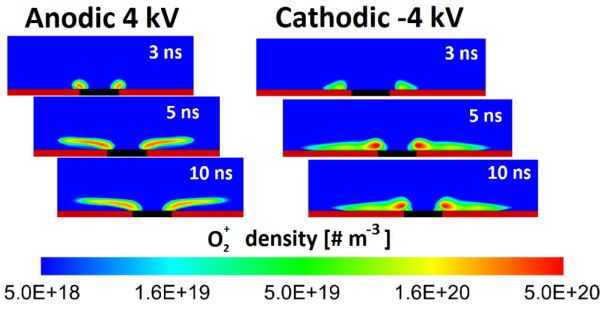


Figure 4.2: Dominant $O_2^+$ ion density profiles indicating plasma formation for anodic pulse (LEFT) and cathodic pulse (RIGHT).

Most of the streamer propagation/plasma formation takes place during

the first 3 to 5 ns of the pulse. The dominant positive charge carrier is $O_2^+$ while the dominant negative charge carrier in the plasma bulk is $O_2^-$ , both of which are on the order of $10^{20}$ $m^-3$. The peak electrons for both anodic and cathodic pulses are of order $10^{19}$ $m^{-3}$. In the streamer channels, the reduced electric field E/N is much lower and electrons are lost due to attachment reactions which form $O_2^-$. The competing processes of ionization and electron attachment at high versus low E/N essentially sets a floor on the minimum E/N for which the streamers will propagate, as discussed by Raizer [86].

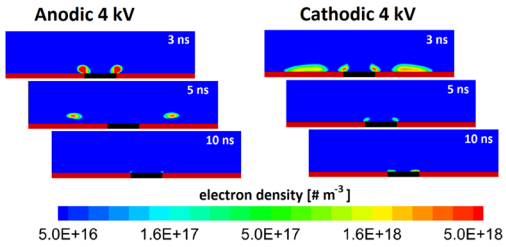


Figure 4.3: Electron number densities in 4 kV anodic and -4 kV cathodic pulses over 10 ns simulation time.

Fig. 4.4 plots the electrical power computed as the surface integral of the particle current times the electric potential at the electrode and dielectric surfaces at each time instance. The potential at the surface of the electrode is plotted by the black dashed lines. Gas breakdown is observed to take place at approximately 3 kV for the anodic pulse and approximately -3.5 kV for the cathodic pulse. Note that power deposition is greater for the cathodic pulse, but that the peak power for both pulses is approximately the same order of magnitude. For the anodic pulse, a large electron current at the electrode characterizes the positive electrode power, while ion current at the dielectric

surface characterizes the negative dielectric power. The ion current pulse lasts longer than the electron current owing to longer drift time scales associated with the ions. Note that much of the power deposition takes place during pulse ramp-up phase, which also corresponds to time when much of the streamer propagation occurs. For the cathodic pulse, a large ion current flows to the electrode and electrons to the dielectric, with corresponding power deposition transients at two surfaces. The longer ion power deposition transient in the cathodic pulse also results in greater gas heating as will be shown later.

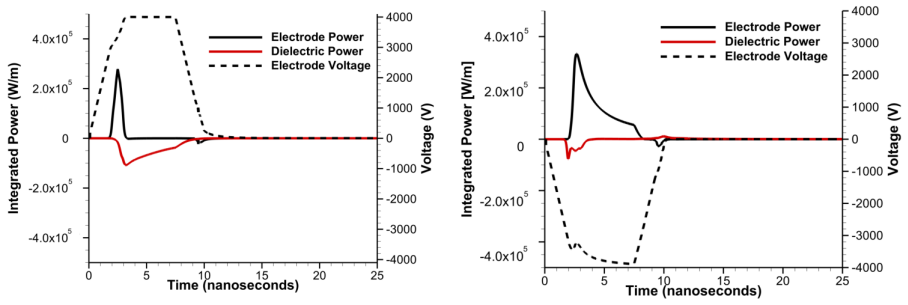


Figure 4.4: Voltage and particle conduction power per unit depth at electrode and dielectric surfaces for anodic pulse (LEFT) and cathodic pulse (RIGHT) in $O_2$-$H_2$ gas. Dashed line represents voltage while solid lines are particle conduction power per unit meter depth into the surface.

Significant quantities of combustion enhancing radical and metastable species are produced by the resulting plasma discharge. A snapshot of the radical and metastable species number densities at the end of the 4 kV anodic pulse is shown in Fig. 4.5. For pulses of both polarities, the dominant combustion radical is atomic oxygen with densities of the order of $10^{21}m^{-3}$. H and OH radical and $O_2(a^1{}_g)$ and $O_2(b^{1+}_g)$ species densities are comparable and of

the order of $10^{20}m^{-3}$. Radicals form in the plasma above the dielectric surface for the cathodic pulse, but the peak densities are approximately an order of magnitude less than the peak densities within the cathode-directed streamers. During the pulse, $O(^1D)$ is produced in greater quantities than the molecular oxygen metastables but is rapidly quenched after the pulse to form $O_2(a^1{}_g)$, $O_2(b^{1+}_g)$ and O.

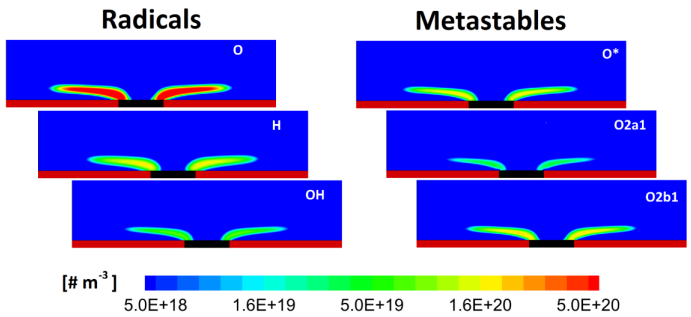


Figure 4.5: Snapshot of radical and metastable species densities at end of 4 kV anodic pulse (10 ns).

For the 4 kV pulses, the peak O mole fractions are approximately 4 x $10^{-3}$ which is about 0.5% of the mixture by mole fraction. It is believed that increased O radical densities, even in quantities as low as 0.5%, are the primary means which lead to a faster initiation of chain reactions and a reduced ignition delay [8]. It is difficult to compare these results with those from experiments and simulations in the literature, as most data is for air-fuel mixtures where nitrogen contributes significantly to O radical production. Experiments and simulations such as in [110] and [8] using methane-air mixtures detected O radicals with mole fractions of order $10^{-4}$ to $10^{-3}$.

#### 4.3.1.2 Gas Heating

Fig. 4.6 shows the time evolution of the temperature and pressure fields for 200 ns simulation time for a cathodic pulse. Gas temperature increase is on the order of 100-400 K at the electrode edges and within the plasma. The most intense heating takes place at the electrode edges and the streamer heads where the electric fields are greatest with the dominant heating mechanism being ion Joule heating ( 90%). Other heating mechanisms such as inelastic collisional heating due to quenching reactions accounts for 10% of the total heating and elastic collisional heating due to electron-heavy particle collision is negligible (<1%).

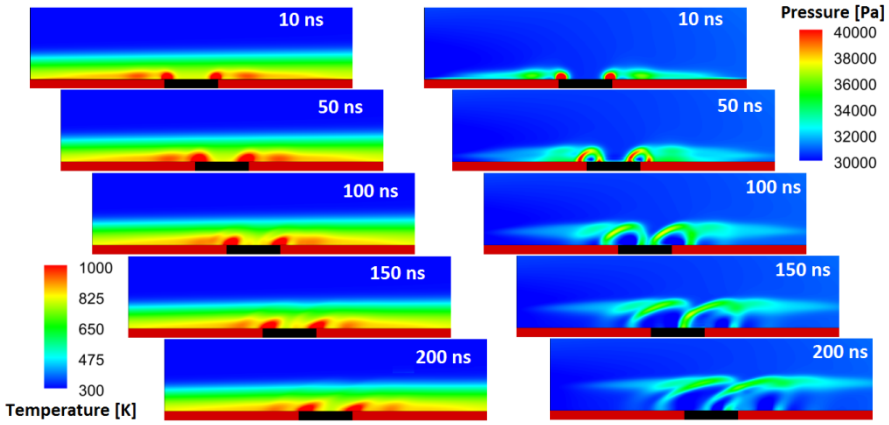


Figure 4.6: Gas temperature and pressure contours from end of cathodic pulse (10 ns) to 200 ns after pulse.

The gas flow responds to the rapid gas heating through the formation of micro blast waves which originate at the electrode edges and the streamer filaments and propagate into the flow as seen in Fig. 4.6. Such micro blast waves

have been observed experimentally by Adamovich et al [6] and Starikovskii et al [107] and have been predicted in computational modeling work by Unfer et al [111]. Although gas heating is observed during the pulse and can be significant (of the order of 100s of Kelvin), the elevated temperatures only persist for several microseconds and quickly dissipates as the flow convects downstream. The overall gas heating and micro blast wave formation behavior for anodic pulses is similar to the cathodic pulses, except for somewhat lower heating and less intense blast wave owing to the lower power deposition in the case of anodic pulses.

### 4.3.2 Dependence on Pulse Voltage Magnitudes

For both anodic and cathodic pulses, increasing the voltage increases the volume of gas that is ionized by the discharge (see 4.7). For anodic pulses, the streamer propagation distance for 8 kV is approximately three times the propagation distance at 4 kV. For cathodic pulses (not shown), increasing the voltage increases the distance from the electrode over which plasma forms on the dielectric surface, but has little effect on the streamers that propagate to the center of the electrode.

For the largest voltage case of an 8 kV anodic pulse, a secondary breakdown is observed between the streamer column and the dielectric surface during the ramp-down phase of the pulse (7-10 ns). This is owing to the fact that the plasma potential does not collapse immediately when the electrode potential is brought to ground at the end of the pulse, resulting in a rapidly

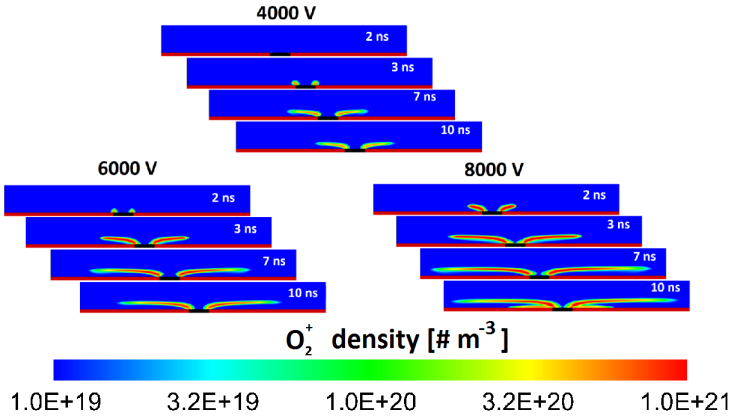


Figure 4.7: Snapshots of $O_2^+$ ion densities illustrating extent of streamer propagation for 4 kV, 6 kV and 8 kV anodic pulses, respectively.

rising reverse electric field that exceeds the breakdown threshold in this region between the streamer column and the dielectric surface. As shown in Fig. 4.8, the consequence is a secondary surface discharge at the end of the anodic pulse that resembles the structure of cathodic pulse.

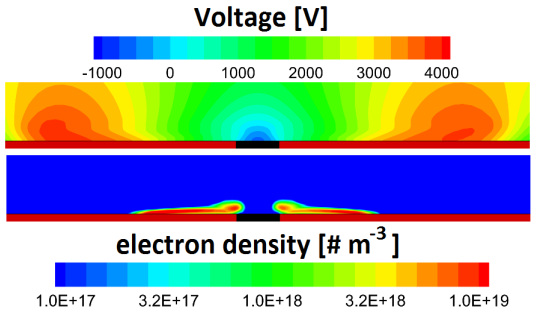


Figure 4.8: Voltage and electron densities 10 ns after start of 8 kV anodic pulse. Note the similarity to the -4 kV cathodic pulse.

Fig. 4.9 compares the temperature and pressures profiles for the anodic pulse simulations after 50 nanoseconds from start of pulse. Increasing

voltage from 4 to 6 kV doubles the peak temperature due to gas heating, from 1200 K to 2400 K. In addition, a much larger volume of gas is heated due to heating taking place within the streamer channels. Gas temperatures are also observed to increase with increasing voltage in the cathodic pulses. Increasing the voltage from 6 to 8 kV did not result in a significant increase in peak temperature compared to the 6 kV case, although the volume of gas which is heated is increased.

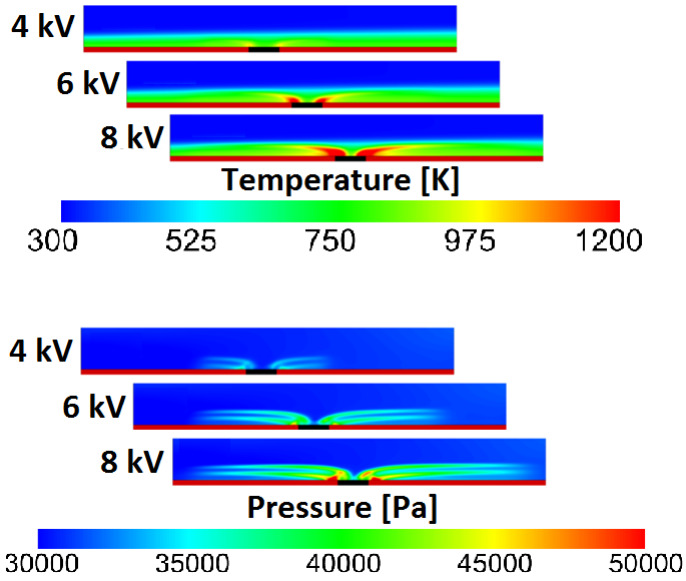


Figure 4.9: Comparison of temperature and pressure fields of anodic pulses of different peak voltages 40 ns after end of pulse.

Increasing voltage results in an increase in peak species densities for both the anodic and cathodic pulses. Increasing the voltage has the most dramatic effect on peak O radical densities, which increase by a factor of nearly three as the voltage is increased from 4 kV to 8kV. The peak densities of the

plasma species on the other hand, only increase moderately as the voltage increases.

### 4.3.3 Chemistry: Argon versus $O_2 - H_2$

The nanosecond pulsed plasma in an argon supersonic flow will now be discussed; the purpose being to elucidate the role of reactive plasma chemistry on the streamer discharge structure. Fig. 4.10 illustrates the formation of the argon plasma for a 4 kV anodic and cathodic pulses, respectively. The structure of the argon discharge is qualitatively similar to the $O_2 - H_2$ cases. The anodic pulse plasma in argon forms cathode directed streamers which propagate away from the electrode over the dielectric surface but without contact with the dielectric. The cathodic pulse plasma in argon also evolves in the same manner as in the $O_2 - H_2$ case, with a pool of electrons that drift rapidly away from the electrode and deposit a negative charge on the dielectric surface. The argon ions subsequently propagate over the dielectric surface (attracted by the negatively charge dielectric) while neutralizing the negatively charged dielectric. However, compared to the $O_2 - H_2$ case, breakdown in argon occurs at lower voltages and since electrons are not consumed by volumetric attachment processes and the streamers propagate much farther compared to the highly electronegative $O_2 - H_2$ plasma. The argon streamers for both anodic and cathodic pulses propagate at significantly greater distances above the surface and above edge of the flow boundary layer. The $O_2 - H_2$ streamers on the other hand, propagate closer to the surface and are entirely confined

within the boundary layer. Note from Fig. 4.10 that electron densities in the anodic pulse peak after the end of the pulse (15 ns run time) due to the reverse electric field induced by the rapid down ramping of the pulse.

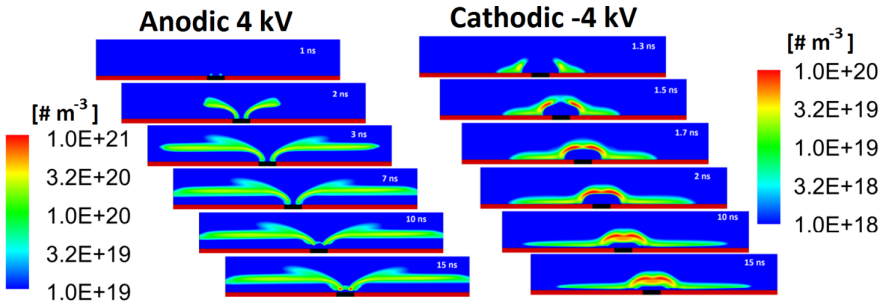


Figure 4.10: 4 kV anodic (LEFT) and cathodic (RIGHT) pulse electron number densities over 15 ns.

Fig. 4.11 shows the particle conduction power for both anodic and cathodic argon pulses per unit meter depth basis. It can be seen that power deposition for the anodic pulse is approximately an order of magnitude greater than the cathodic pulse. The disparity in power deposition into the plasma results in a peak cathodic pulse plasma density approximately one order of magnitude lower than the anodic pulse peak plasma density. Most of the ion Joule gas heating in the anodic pulse takes place after the pulse, indicated by (ion) particle current flux into the electrode in Fig. 4.11 (a). There is no noticeable gas temperature increase for the cathodic pulse.

The difference in power deposition for the anodic and cathodic pulse cases translates into dramatically different heating profiles. For the anodic pulse, most gas heating takes place after the pulse, as seen below in Fig. 4.12. Peak gas temperatures for the 4 kV anodic pulse ( 4000 K) are more than

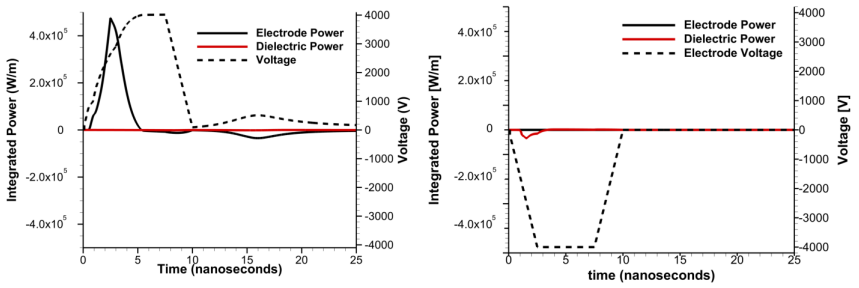


Figure 4.11: Anodic (a) and cathodic (b) pulse instantaneous particle conduction power. The dashed line represents voltage at the electrode while solid lines represent power due to particle fluxes at the electrode and dielectric surfaces.

double the peak gas temperature of the $O_2 - H_2$ 4 kV anodic pulse ( 1200 K). For the argon cathodic pulse on the other hand, the negligible power deposition results in virtually no gas heating. This trend is opposite to that seen for $O_2 - H_2$ where cathodic pulses produce higher gas temperatures.

Fig. 4.12 shows snapshots of the gas temperature profile at the end of the pulse and 10 ns after the end of the pulse. No heating is observed to take place within the argon plasma streamer channels, which is in contrast to the $O_2 - H_2$ case where significant heating is observed to occur along the streamer channels. Note also that gas heating peaks approximately 10 ns after the pulse has ended. Since the argon streamers propagate above the boundary layer in a higher density region of the flow, the reduced electric fields are weaker and ion Joule heating in the argon streamers is lower compared to the $O_2 - H_2$ streamers. This results in relatively little gas heating during the initial streamer propagation phase. The reverse electric field induced by the rapid down ramping of voltage on the other hand, exceeds the electric fields

seen in the propagating streamer heads. Due to the large amount of space charge in the streamer channels (compared to the $O_2 - H_2$ pulse), this electric field persists for approximately 10-15 ns after the end of the pulse. During this time, intense ion Joule heating increases the temperature of the gas in the electrode near field region by several thousand degrees.

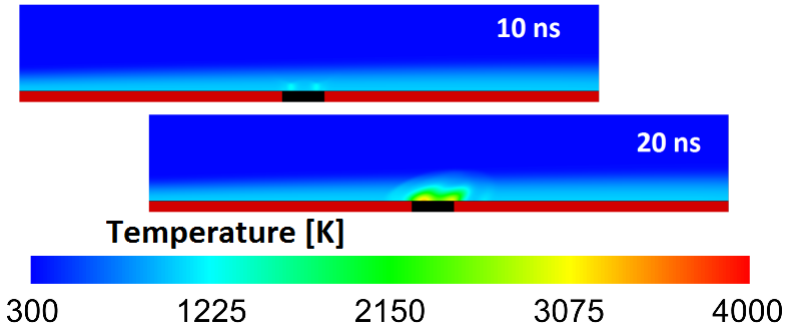


Figure 4.12: Gas temperature profile for argon anodic (4 kV) pulse 10 ns and 20 ns after start of pulse.

### 4.3.4 Flow Effects

An adiabatic wall boundary condition is used for the flow. This boundary condition results in the formation of a thermal boundary layer with a wall recovery temperature of approximately 800 K compared to a free stream temperature of 300 K. The increase in temperature results in a decrease in the background gas number density within the boundary layer region to almost a third of the value in the free stream. Consequently, the primary effect that the flow has on the nanosecond pulsed plasma is a relative increase in the reduced electric field which encourages plasma formation within confines of the boundary layer. In the presence of flow, the $O_2 - H_2$ gas breakdowns down and forms

plasma entirely within the lower density region of the boundary layer. In the absence of flow a uniformly high background density in the entire domain results in lower reduced electric fields for a given electrode voltage. This results in an absence of breakdown and plasma formation for both the 4 kV and the 6 kV cases; the threshold for breakdown being higher than the highest voltage cases explored in this study. It is only when the voltage is increased to 8 kV or higher that breakdown was observed for the cases without flow.

The time scale for the plasma formation is significantly smaller than the time scale of bulk flow convection. As a result, the flow is essentially frozen during the time period of the plasma pulse phenomena. For time scales much greater than the duration of the pulse bulk flow effects start having a noticeable effect on the longer lived plasma species and their transport. Fig. 4.13 shows evolution of the O radical densities produced by a 4 kV anodic pulse in $O_2 - H_2$ mixture over a time duration of 200 ns. The initial O radical distribution during the pulse is symmetric about the electrode geometry. For later times, flow convection effects start becoming important and result in the transport of the O radicals in the downstream direction.

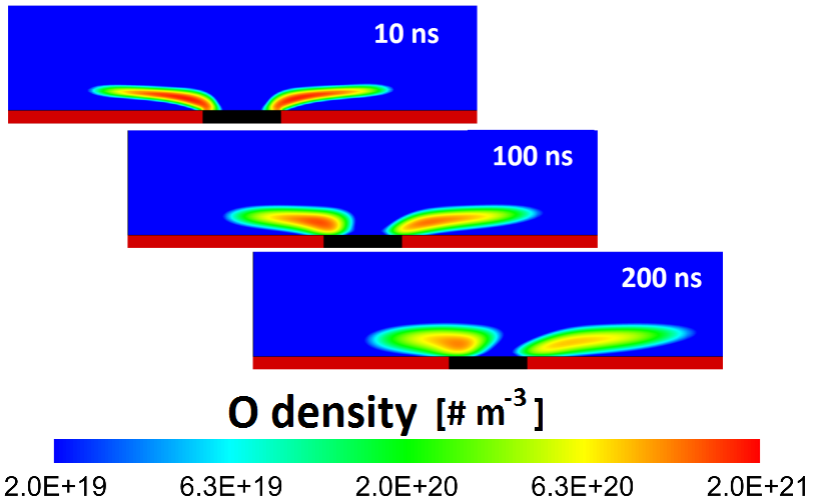


Figure 4.13: Convection of atomic oxygen radicals over 200 ns for the 4 kV anodic pulse.

## 4.4 Summary and Conclusions

A detailed computational modeling investigation of nanosecond pulsed surface plasma discharge interacting with a supersonic premixed flow stream is performed in this work. Anodic and cathodic pulses at voltages ranging from 4 kV to 8 kV are studied. A comparison of pulsed discharge in premixed $O_2 - H_2$ stream with a pure argon stream is made to quantify the effect of reactive chemistry in these discharges.

For both gases, the anodic pulse forms cathode directed streamers which propagate away from the electrode. The cathodic pulse plasma forms as a surface discharge which propagates over the adjacent dielectric surface due to charge trapping, with the dielectric itself acting as a virtual electrode. The $O_2 - H_2$ plasma formed by both pulse types is highly electronegative.

Oxygen radicals with peak densities of $2\text{x}10^{21}$ $\text{m}^{-3}$ (mole fraction of 4x10-3) are the dominant species produced in the 4 kV anodic and cathodic pulses. O radicals are convected downstream of the discharge region over microsecond timescales.

Rapid gas temperature increase of 100s of Kelvin due to ion Joule heating at the electrode edges was observed, which results in micro blast waves for both anodic and cathodic $O_2 - H_2$ pulses. Gas heating was higher for the cathodic pulse. Gas heating due to inelastic collisions was also observed within the plasma during and after the pulse, but at an order of magnitude lower than ion Joule heating. Increasing voltage results in an increase in plasma propagation distance, peak species number densities, and gas heating for anodic and cathodic pulses.

Reactive chemistry of the gas can result in dramatically different plasma dynamics and gas heating. The streamers propagate above the boundary layer and over greater distances than for the $O_2-H_2$ cases. Gas temperature increase of thousands of Kelvin was predicted for the argon 4 kV anodic pulse, but no heating at all was observed in the 4 kV cathodic pulse in argon. Unlike the $O_2 - H_2$ pulse, the electric fields induced by the rapid down ramping of the pulse exceed the electric fields of the initial propagating streamers and persist over a longer period of time due to the larger amount of space charge in the streamers. As a result, the most intense gas heating is observed after the pulse is terminated.

Overall, the results indicate that most of the radicals and metastable

species that eventually lead to combustion enhancement are produced within the streamers. Anodic pulse streamers are found to propagate at a certain distance away from the surface compared to the cathodic pulse streamers, which remain in contact with the surface throughout their lifetime. Consequently, it is anticipated that radical species produced by anodic pulsed streamers are less likely to be quenched at the surface and can be carried further into the free stream where they can participate in combustion enhancement processes, i.e. anodic pulsing is a more efficient strategy for combustion enhancement using surface mounted pin electrodes.

# Chapter 5

# High Pressure Streamer Discharges for Automotive Combustion Ignition Applications

The first stage (transient plasma formation) is simulated for single high voltage nanosecond pulses. The primary objective is to quantify the production of different radical species produced by the resultant plasma discharge. Due to the short duration of the simulations performed in this work (10-20 ns), it is assumed that the gas temperature remains fixed for the duration of the simulation. This assumption is valid based on the experimental observations of [98], [116] that gas temperature increase during the initial transient plasma stage is negligible.

## 5.1 Discussion of Chemistry : Methane-Air

The gas chemistry mechanism is for lean and stoichiometric methane-air mixtures. The following species are modeled : electrons (E) , O, $N_2$, $O_2$, H, $N_2^+$, $O_2^+$, $N_4^+$, $O_4^+$, $O_2 + N_2$, $O_2^-$, $O^-$, $O_2(a1)$, $O_2(b1)$, $O_2^*$, $N_2(A)$, $N_2(B)$, $N_2(C)$, $N_2(a1)$, $CH_4$, $CH_3$, $CH_2$, $CH_4^+$, $CH_3^+$, $CH_2^-$, and $H^-$ (see Appendix E). A description of the lumped molecular excited states in the above species list and the corresponding original excited states and their excitation energies

is shown in Appendix A.

The gas chemistry mechanism consists of 85 reaction pathways as shown in Table 3. Approximately half of the reactions (G1 to G43) are electron impact reactions that depend on the electron temperature. The reaction rate coefficients for these reactions are calculated offline using the zero-dimensional Boltzmann solver (BOLSIG+) [40] using reaction cross-section data from the literature. The remaining reaction rate coefficients between heavy species such as ions and neutrals are modeled using the standard Arrhenius form, where T is the temperature of the background gas. Species indicated by the suffix (rotational), (vibrational), and (electronic) are the corresponding excited species that are not explicitly tracked as excited species but are simply lumped as species in the ground state with only the energetics of formation of these species accounted for in the reaction.

## 5.2 Geometric Configuration

Two geometric configurations are considered in this study: a coaxial electrode geometry similar to HSP discharge geometry investigated by [95] and [98] where the inter-electrode distance is of order a few mm and a corona geometry where a single powered electrode is placed in fee space, i.e. the second electrode is a virtual ground at infinite distance from the powered electrode.

### 5.2.1 Coaxial Electrode Geometry

The coaxial electrode geometry comprises two concentric cylindrical electrodes with an inner powered electrode of radius 1.2 mm and the outer grounded electrode of radius of 4 mm. The inner electrode surface is modified with small roughness tips to concentrate the local electric field which serves to pin the location of the streamer formation at this electrode. A uniform square voltage pulse of magnitude of 40 kV is applied to the inner electrode for all simulations. The physical time simulated ranges from 10 to 15 nanoseconds.

As mentioned earlier, the nanosecond pulsed discharge in a coaxial electrode configuration was experimentally found to have numerous individual unbranched streamers that nearly uniformly fill the inter-electrode gap [98]. The focus is on a single steamer event within the coaxial electrode gap.

Several simplifying assumptions are made for the simulations. Only a two-dimensional planar geometry with a 20 degree sector of the coaxial electrode gap is simulated as shown in Fig. 5.1. A single streamer propagates in this gap through the duration of the transient and the location of streamer initiation on the inner electrode is ensured by a single roughness tip (tip angle of 27 degrees) placed within this 20 deg. sector (Fig. 5.1). Furthermore, we assume that the dynamic of the single streamer propagating in the gap is unaffected by other streamers that propagate simultaneously in the real coaxial gap; essentially we assume that characteristic distance between multiple streamers defined by the 20 deg. sector is large enough that the streamers do not interact with each other. As discussed below, we perform simulations

to justify these assumptions. The computational mesh itself consists approximately of 60,000 finite volume cells.

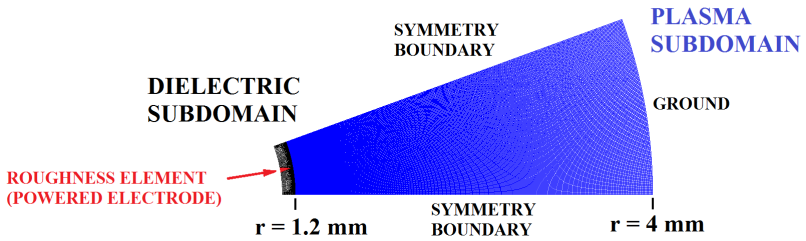


Figure 5.1: Coaxial electrode discharge mesh geometry used in the simulations (20 deg.).

The background pressure and temperature are assumed to be 10 atmospheres and 700 K, respectively, resulting in a background density of 1.026 x $10^{26}$ $m^{-3}$. As noted earlier these conditions are typical of an IC engine environment. Two cases for air-to-fuel stoichiometry were studied: one a lean mixture with air/methane (A/F) molar ratio of 40:1 and a stoichiometric A/F ratio of 17.2:1. The corresponding molar fractions of the $CH_4$ : $O_2$ : $N_2$ is 0.02439: 0.204878: 0.770732 in the lean case and 0.054945 : 0.198462: 0.746539 in the stoichiometric case

### 5.2.2 Corona Geometry

The numerical mesh and boundary conditions for the corona geometry are shown in Fig. 5.2. A single powered electrode is assumed to be a sharp tip (38.85 deg. angle). As in the coaxial electrode geometry we assume two-dimensional planar domain. Since the streamer in a corona geometry

propagates in an unconfined domain, it is computationally infeasible to represent a large enough domain where the outer ground (zero potential) plane is at an asymptotically large distances. To overcome this computational challenge, we have used an inset subdomain approach where only the Poissons equation for the electrostatic potential in the entire domain (shown in red and black in Fig. 5.2) which is made large enough that the outer ground boundary is at sufficiently large distance from the power electrode. The entire set of plasma governing equations, including the Poissons equation) are solved in a subset of the large domain (shown in red in Fig. 5.2) where the steamer propagates for the time duration of the simulation. Outside of this plasma subdomain the Poissons equation is transformed into the Laplace equations, because of absence of space charge. The overall computational load using this inset subdomain approach makes the simulation time more feasible. A similar inset subdomain approach in the context of a flow-plasma problem is discussed in detail in Ref. [67] and the previous chapter of this dissertation.

For the geometry shown in Fig. 5.2, the gap separation distance between the tip of the powered electrode and the outer grounded shell is 4 cm. The entire numerical mesh consists of 75,779 mixed quad and tri cells. To reduce the computational cost of the simulation, the domain was decomposed into two separate domains. A plasma domain (shown in red) extending 1 cm from the prong tip consisting of 66,780 cells surrounded by a dielectric domain (shown in black) consisting of 8,999 cells.

The background pressure is set to 10 atmospheres (background density

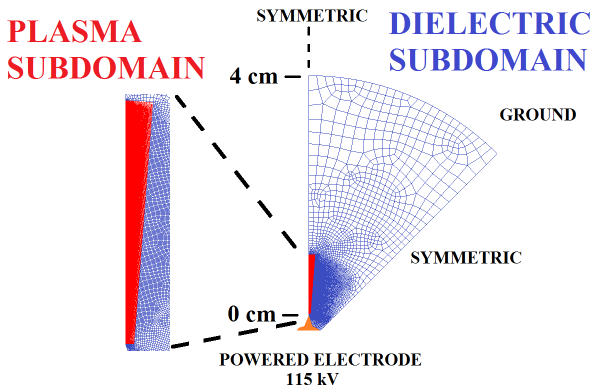


Figure 5.2: Corona discharge geometry and mesh. Blue indicates dielectric subdomain and red indicates the inset plasma sub domain.

of 1.026 x $10^{26}$ $m^{-3}$) and the background gas temperature is set to 700 K. Two conditions of air/methane (A/F) ratios corresponding to a lean stoichiometry of 40:1 and stoichiometric A/F of 17.2:1 were studied. A uniform square voltage pulse of 115 kV is applied at the powered electrode for a physical time duration of 30 ns.

## 5.3 Results

### 5.3.1 Coaxial Electrode Geometry

The pulse duration in the coaxial electrode geometry of 10 ns was sufficient for the streamers emerging from the inner electrode to bridge the interelectrode gap of about 2.8 mm. The following assumptions were made in the choice of simulation domain for this discharge: A 30 deg. sector domain was chosen instead of the entire coaxial electrode geometry with the assumption that streamer discharge phenomena within this sector can be studied in

isolation from the remainder of the geometry. Furthermore a single roughness element was used to pin the location of the streamer initiation on the inner electrode. Fig. 5.3 shows results for the electron density profiles in the streamer discharge at two different physical times in the transient (3.5 ns and 7.5 ns) for the cases with a single roughness element and multiple (eight) roughness elements placed on the inner electrode. Individual streamers are observed to be initiated at each of the roughness elements for both the single and the multiple roughness element cases. For the single roughness element case the individual streamer propagates radially outwards until it eventually reaches the outer ground electrode. In the multiple roughness element case, the individual streamers formed at each of the roughness element are observed to interact strongly at the initial stages of the transent, so much so that it is difficult to distinguish between the individual streamers owing to the diffuse seed electron cloud created around the streamers due to photo-ionization. The streamers were observed to quickly merge with each other a few ns into the transient and subsequently continue to propagate in the discharge as a single streamer until the interelectrode gap is bridged a the end of the transient. The overall properties of the individual streamer formed by the multiple roughness element case is nearly indistinguishable from the single roughness element case for much of the discharge transient. These results indicate that overall dynamics of the streamer propagation in the discharge is insensitive to the details of discharge initiation at the inner electrode. Use of a single roughness element is therefore reasonable. Importantly, the single roughness

element pins the location of the streamer propagation to the center radial line along the sector domain preventing interaction of the streamer with the side boundaries. Another important conclusion can be made from these results, i.e. that the 20 deg. sector domain is sufficiently large to capture the dynamics of a single streamer propagating along the coaxial electrode gap without interactions from other streamers that may propagate simultaneously in the case of the full coaxial electrode geometry.

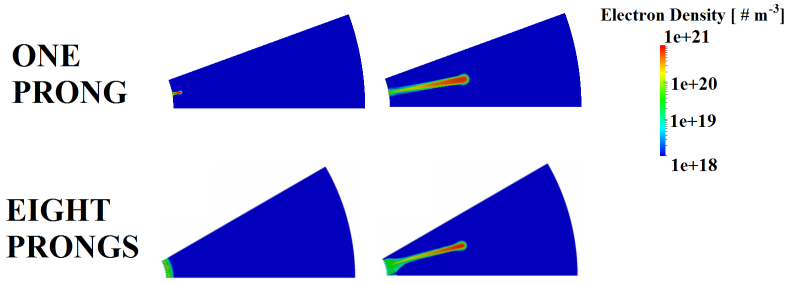


Figure 5.3: Streamer propagation from single and multiple roughness elements on the inner powered electrode of the coaxial electrode discharge.

Next, the dynamics of the streamer propagation in the coaxial electrode geometry are discussed in detail. For the baseline operating conditions (10 atm, 700 K, 40 kV, 40:1 A/F ratio) gas breakdown occurs at the single roughness element after about 2 nanoseconds of the square wave pulse being switched on. Here gas breakdown is defined as the induction time between the start of the excitation pulse and the observation of a large electron density (above threshold value of $10^{19}$ $m^{-3}$) in the vicinity of the roughness element. The resulting streamer propagates radially outwards to the outer grounded electrode and bridges the gap after about 10 nanoseconds. The

average streamer propagation speed is about 280 km/s. The streamer dimension in the transverse direction (width) is about 200-300 microns. Fig. 5.4 shows time snapshots of the electron densities (top) and electron temperatures (bottom) for each slice starting from the right and increasing in time in the clockwise direction.

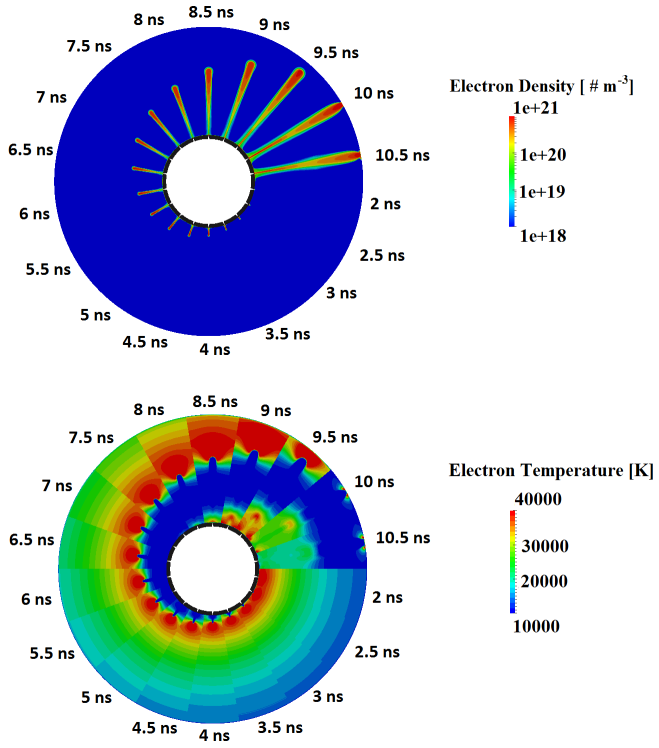


Figure 5.4: Time snapshots of electron density and electron temperature over 10.5 nanoseconds of simulation time. The transient is indicated by snapshots of a 20 deg. subset of the domain placed in the clockwise direction starting from 2 ns after the pulse is switched on.

There are two discernible stages of the streamer discharge. For the first 8 nanoseconds of the discharge transient, plasma (charged species) production

only takes place within the localized region around the streamer head (the leading edge of the streamer column). This is called the primary streamer. As the streamer approaches the grounded outer shell, a secondary streamer forms at the base near the roughness element and propagates into the gap in the wake of the primary streamer. The location of the plasma production in the primary streamer and the formation of secondary streamer in the latter part of the transient is clearly discernable through the electron temperature profiles, that indicate high values of order 4 eV and higher at the primary streamer head at the base of the primary streamer column once the secondary streamer is formed. The bulk of the streamer column has a lower temperature of less than 1 eV where plasma production is negligible. Peak electron densities in the streamer is of order $10^{21}$ $m^{-3}$.

The dynamics of secondary streamer formation in the wake of the primary streamer has been discussed in the literature. For example, a detailed study on the physics of streamer discharge propagation in short air gaps and the transient processes leading to spark formation including the formation of primary and secondary streamers can be found in [68], [68]. In these studies, the formation of the primary streamer and secondary streamer is compared to the formation of a transient positive column of a glow discharge with a cathode fall region. The secondary streamer acts as a luminous positive column that forms when the primary streamer reaches the target electrode, with the cathode fall at this electrode. An alternative viewpoint is presented in Ref. [97], suggests that the secondary streamer is in fact not a distinct streamer at

all but simply a luminous plasma that forms in the channel due to an attachment instability in oxygen. For reasons discussed below we take the former viewpoint that a distinct streamer does indeed form during the latter part of the transient and hence can be called the secondary streamer.

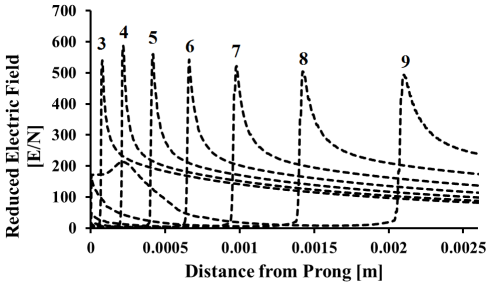


Figure 5.5: Reduced electric field (E/N) along the centerline of the streamer in the coaxial electrode geometry for various times (in nanoseconds) during the transient.

The reduced electric field (E/N) (defined as the ratio of the magnitude of the local electric field to the background density) along the center-line streamer is shown in Fig. 5.5 at several time instances during the transient. At any given time instance the E/N is a maximum of 500-600 Td (1 Td = $10^{-17}$ V-cm$^2$) at the location of the streamer head and decreases sharply within the vicinity of the streamer column behind the heard to values of order 10 Td or less. In front the streamer head (undisturbed gas), the E/N asymptotes to the value close to the vacuum E/N of order 100-200 Td (i.e. the reduced electric field in the gap without the streamer). Note that the breakdown threshold of lean fuel-air mixtures is of order 100 Td [105]. The structure of the streamer is therefore such that the electric fields are significantly over-volted

(higher than the breakdown threshold) within the streamer head resulting in rapid ionization of the gas in this region and significantly under-volted (below breakdown threshold) within the streamer column so that the plasma cannot be sustained and is essentially decaying within the column. During the latter part of the transient (greater than 8 ns), the E/N at the inner electrode once again exceeds the breakdown threshold resulting in the secondary streamer. These results therefore justify the observations that a self-sustaining secondary streamer does indeed form in the latter part of the transient.

For all subsequent simulations, regardless of temperature, pressure or applied voltage, it was observed that the magnitudes of the reduced electric fields in the primary and secondary streamers are approximately the same as they are for the above baseline case. The width of the streamer and the streamer propagation velocities differ depending on the specific conditions of the discharge.

The yield of charged species and radicals from a non-equilibrium discharge is widely assumed to be the basis of combustion ignition enhancement [95], [105]. The O radical has specifically been identified as the most important radical in the combustion ignition enhancement process. Fig. 5.6 shows the time evolution of the O radical densities during the streamer discharge transient. The O radicals are formed in the high electron temperatures regions of the streamer head through electron impact dissociation processes and remain nearly constant in the streamer column as the streamer sweeps through the gas mixture. Toward the end of the transient high O radical densities are

observed close to the inner electrode corresponding to the formation of the secondary streamer. The peak O radical densities are of order $10^{23}$ $m^{-3}$. In the context of the above result it is worth noting the transient plasma ignition experiments discussed in Ref. [98] where a coaxial electrode configuration similar to our geometry was used to ignite an atmospheric pressure $C_2H_4$-air mixture. These authors report that flame ignition occurs at the base of the streamer (in the vicinity of the inner powered electrode) and propagates outwards (see Fig. 3 in their paper). Correlating the location of flame ignition kernel location to regions of high radical densities, it is reasonable to assume that radicals (particularly the O radicals) are highest in the vicinity of the inner electrode, thus providing an indirect validation of the predictions made in this study.

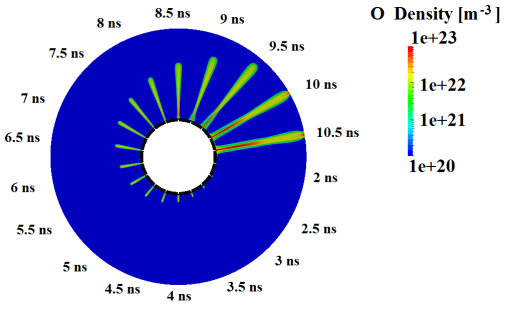


Figure 5.6: Time snapshots of oxygen radical densities over 10.5 nanoseconds of simulation time.

The total yield of charged and neutral radical species in the single streamer discharge near the end of the transient at 9.5 ns is shown in Fig. 5.7. To aid in the comparison of the radical yields of the coaxial and corona

simulations, the species densities are averaged using a canonical streamer geometry. First, the species densities are averaged over the entire computational domain. The volume is then re scaled assuming the densities are spread uniformly over a canonical streamer volume with a 200 micron width and 4 mm. All subsequent species density histograms and transients are scaled for this canonical streamer geometry.

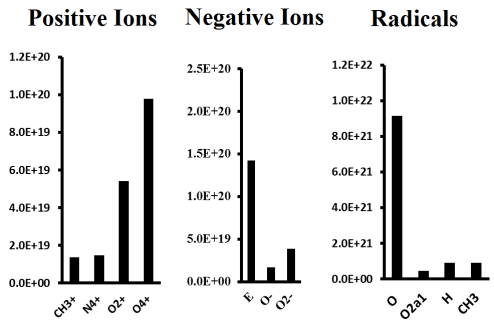


Figure 5.7: Volume averaged species densities for coaxial electrode geometry under lean stoichiometry conditions at 9.5 ns (after the average species densities are evenly distributed over canonical streamer geometry of 200 micron width and 4 mm length).

The $O_4^+$ cluster ion is found to be the dominant positive ion species, followed by the dimer ion $O_2^+$, $CH_3^+$ and $CH_4^+$ in decreasing magnitude. The electron is the dominant negative charged species with a volume average density which is slightly higher than the $O_4^+$ cluster ion. Other important negative ions are $O_2^-$ and $O^-$; the remaining negative ions being negligibly small compared these ions. The neutral radical pool is dominated by O radicals followed by H, $CH_3$, and singlet delta oxygen that have about an order of magnitude lower densities compared to O. Within the primary streamer column peak O

radical densities are on the order of 2x10$^{22}$ m$^{-3}$. Peak O radical densities in the secondary streamer are as high as 6x10$^{22}$ m$^{-3}$.

Fig. 5.8 shows transient evolution of the volume averaged radical densities as a function of time for the canonical streamer volume. Most of the radical production is observed to occurs after approximately 8 nanoseconds, which corresponds with the emergence and propagation of the secondary streamer. This implies that the efficiency of the coaxial electrode geometry for non-equilibrium plasma combustion ignition applications depends strongly on the pulse duration, with the pulse duration required to be long enough for secondary streamer formation with the concomitant large radical formation.

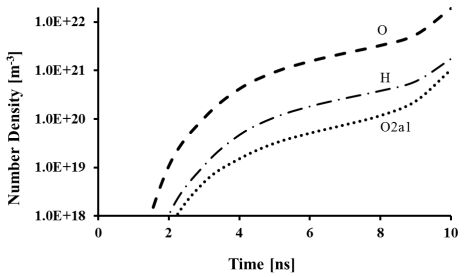


Figure 5.8: Transient evolution of the volume averaged radical densities for the coaxial electrode geometry with lean stoichiometry (after the average species densities are evenly distributed over canonical streamer geometry of 200 micron width and 4 mm length).

Fig. 5.9 compares the electron densities profiles in the streamer for the lean and stiochiometric at the instance where the streamer head reaches the outer grounded electrode. For the stoichiometric condition this instance is reached at 8.8 ns compared to 9.7 ns for the lean condition, indicating that the average streamer propagation speed increases slightly with increasing fuel

mole fraction. From the figure it can be seen that the width of the streamer is slightly lower (100-200 microns) and the electron density is slightly higher in the stoichiometric case compared to the lean case. The higher electron density is attributed to the lower oxygen densities in the stoichiometric case which in turn result in lower electron attachment. The decrease in the width of the streamer is attributed to the higher electron densities which lowers the Debye length in the streamer head region which in turn affects the size of the non-zero space charge region in the head.

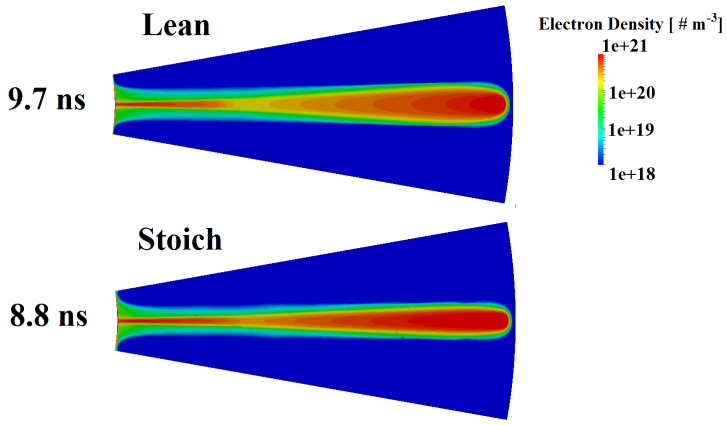


Figure 5.9: Electron density for lean (TOP) and stoichiometric (BOTTOM) fuel-air mixtures

The volume averaged charged and radical species densities in the stoichiometric case are presented in Fig. 5.10 and can be compared to the same densities for the lean case in Fig. 5.7. Overall the positive and negative charged species densities for the stoichiometric case is very similar to the lean case; the $CH_3^+$ ion densities are observed to be marginally higher in the stoichiometric case compared to the lean case. The dominant O radical is

observed to be slightly lower in the stoichiometric case compared to the lean case because of the lower oxygen background densities.

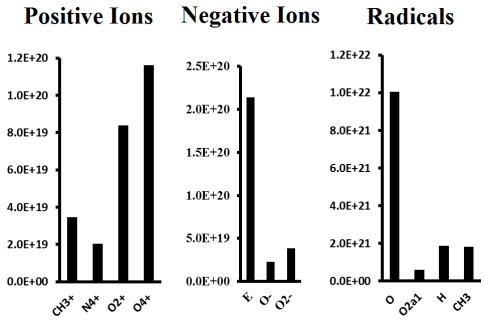


Figure 5.10: Volume averaged species densities for coaxial electrode geometry under stoichiometric conditions at 8.8 ns (after the average species densities are evenly distributed over canonical streamer geometry of 200 micron width and 4 mm length).

### 5.3.2 Corona Geometry

We now present results for the corona geometry. Here the gap is infinitely large in the physical system resulting in different streamer discharge dynamics compared to the finite gap coaxial electrode geometry. Longer pulse times of 30 ns are considered for this geometry. The presence of the sharp powered electrode tip anchors the location of the single streamer formation and propagation into the discharge volume.

Fig. 5.11 shows transient snapshots of the electron density profiles for the lean (A/F 40:1) and stoichiometric (A/F 17.2:1) cases. For both cases the streamer is observed to propagate about 5 mm into the open fuel-air mixture in the 30 ns transient time. The propagation speed of the streamer for both

cases is around 180 km/s with the streamer speed for the stoichiometric case being slightly higher than the lean case. Note that the average propagation speed for the corona geometry is lower that the coaxial geometry where speed of around 280 km/s were observed. The width of the streamer is about 40-50 microns which is significantly thinner than the coaxial electrode streamer. The electron temperatures in the streamer head (not shown) are of the order of 8-10 eV in the streamer head, which is again similar to the streamers in the coaxial electrode geometry. One important distinguishing factor between the streamer in the corona geometry and the coaxial electrode geometry is the absence of any secondary streamer and the corresponding lack of electron density increase in the vicinity of the powered electrode during the latter part of the transient. This feature is clear from the transient profiles of the reduced electric fields along the length of streamer.

In Fig. 5.12 it is seen that the reduced electric fields E/N in the streamer head are on the order of 500-600 Td for both the lean and stoichiometric mixtures. The E/N within the streamer column is below threshold at around 10 Td. The slightly high streamer propagation speed in the stoichiometric case is also clearly evident from this figure. The features of the streamer in the corona geometry are essentially the same as in the coaxial electrode geometry with one important exception being the complete absence of secondary streamer as is evident from the absence of any increase in the E/N at the powered electrode throughout the transient.

Finally, the charged and radical species yields from the corona discharge

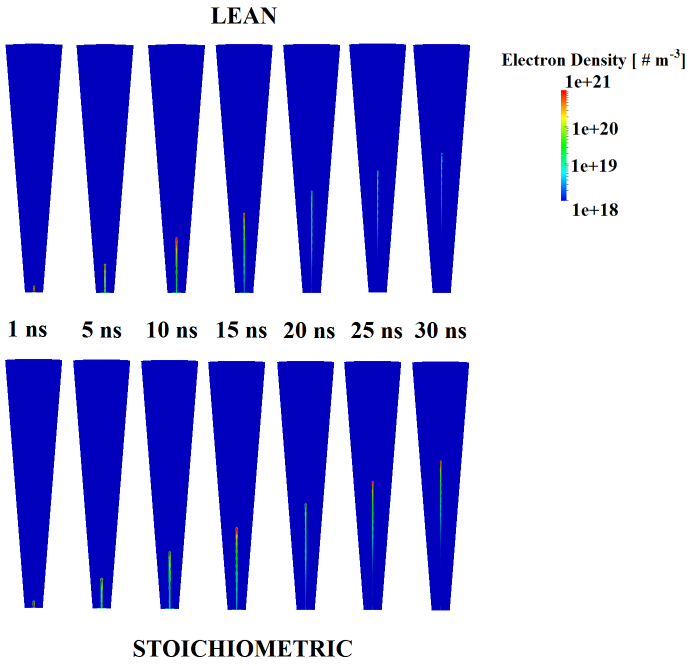


Figure 5.11: Electron number densities snapshots in streamer channel over pulse duration for lean (TOP) and stoichiometric (BOTTOM) mixtures.

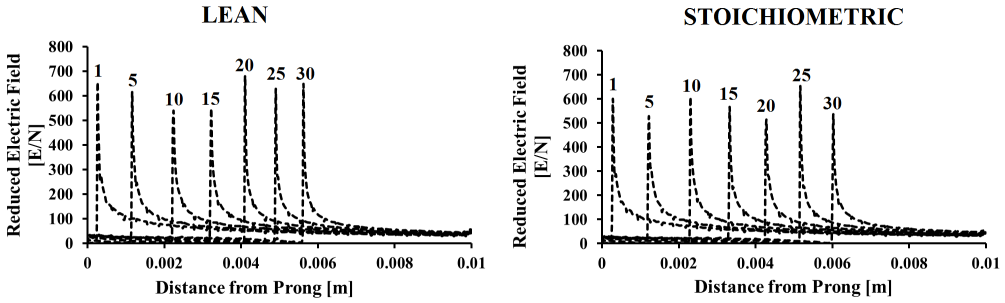


Figure 5.12: Reduced electric field (E/N) for lean (LEFT) and stoichiometric (RIGHT) fuel mixtures along streamer centerline as function of time (in nanoseconds).

are discussed. Fig. 5.13 shows profiles of the O radical densities at the end of the 30 ns transient time for both the lean and stoichiometric cases. Within

the streamer columns, both lean and stoichiometric cases have approximately the same quantity of O radicals (order 4x$10^{22}$ $m^{-3}$) which is higher than in the primary streamer column of the coaxial electrode case (order 2x$10^{22}$ $m^{-3}$).

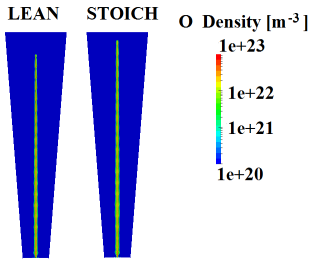


Figure 5.13: O radical distribution in streamer channels at end of simulation (30 ns) for lean (LEFT) and stoichiometric (RIGHT) cases.

The volume averaged densities in the corona case of charged and neutral radical species for the canonical streamer geometry (4 mm long and 200 microns wide) is shown in Fig. 5.14. In the lean case the $O_4^+$ is the dominant positive ion, but the $CH_3^+$ ion density is comparable in magnitude. In the stoichiometric case the $CH_3^+$ ion is the dominant ion with $O_4^+$ ion density being slightly lower. These results are in contrast to the coaxial electrode geometry streamers where the $O_4^+$ ion was clearly much more dominant than the rest of the positive ions. For negatively charged species, the electron reattach to form negative ions and the plasma is predominantly electronegative except in the vicinity of the streamer head. In the case of neutral radicals, the O radicals are the dominant radicals and with with some $CH_3$ and H radicals densities about an order of magnitude lower. The neutral radical composition is similar to those seen for the coaxial electrode geometry.

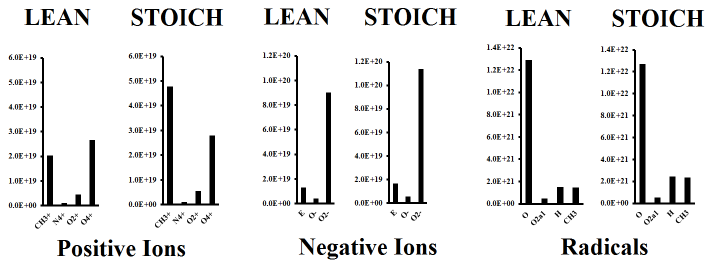


Figure 5.14: Volume averaged charged and radical species number densities for the corona streamers after 30 ns (after the average species densities are evenly distributed over canonical streamer geometry of 200 micron width and 4 mm length).

Fig. 5.15 displays the volume averaged transient evolution of the primary radicals for the corona geometry assuming the species densities are distributed evenly over a canonical streamer volume of 200 micron width by 4 mm length. As was the case for the coaxial discharge, O radicals dominate and the net radical pool increases in time as the streamer propagates further into the volume. Comparing the time averaged radical yield of the corona (Fig. 5.15) to the coaxial discharge (Fig. 5.8), it is seen that the net yield of O radicals is greater for the corona discharge.

### 5.3.3 Summary and Conclusions

Simulations of corona discharges at high pressures (10 atm) in methane-air mixtures were performed for both short gap (2.8 mm) and long gap (4 cm) cylindrical geometries with an inner powered electrode and a grounded outer shell. For the short gap simulations, it was found that the plasma bridges the gap after approximately 10 nanosecond and is followed by a secondary streamer

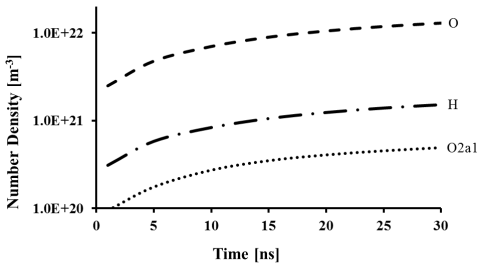


Figure 5.15: Transient evolution of the volume averaged radical densities for the corona geometry with lean stoichiometry (after the average species densities are evenly distributed over canonical streamer geometry of 200 micron width and 4 mm length).

that forms in the plasma channel left behind by the primary streamer.

It was found that most of the radicals (particularly O radicals) are formed in the secondary streamer channel and are localized near the anode which is consistent with experimental observations. For the long gap simulations, the plasma propagates as a single long streamer. It was found that while the plasma produces a relatively uniform density channel of O radicals, peak radical production is localized near the prong tip where the electric fields are highest. For both the long and short gap simulations, it was found that varying the fuel-air ratio has little impact on the plasma discharge or radical yield other than slightly modifying the ratios of the oxygen to fuel radicals. The net radical yield is greater for the corona discharge than for the coaxial discharge, though the width of the corona streamer (about 40 microns) is less than the coaxial streamer (about 200 microns). The resulting simulations are consistent with experiments using similar geometries where it was observed that ignition kernels form near the high reduced electric fields of sharp geometric features

such as pins or roughness elements.

# Chapter 6

# Atmospheric Pressure Plasma Jets

The simulations of an atmospheric pressure plasma jet in an open air gap is presented. Parametric studies of several key factors are performed: gas composition in the inert gas/ambient gas, the size of the tube, the geometry of electrode (thickness of the electrode), the growth rate of the diffusional mixing layer between the jet and ambient gases and the plasma chemical kinetics. In addition to open air gaps, simulation results for laminar flow impinging on a target plate are presented along with the relevant quantities of interest such as the flux of radical and ionized species delivered to the target.

## 6.1 Discussion of Chemistry: Helium-Air

The plasma chemistry mechanism used in this study consists of 16 species and 40 reactions shown in Appendix D. The air (oxygen-nitrogen) chemistry sub-mechanism was taken from [45] and the helium and helium-nitrogen chemistry sub-mechanism was taken from [117]. The entire chemistry consists of the following species: E, O , $N_2$, $O_2$, $N_2^+$ , $O_2^+$, $N_4^+$, $O_4^+$, $O_2 + N_2$, $O_2^-$, $O^-$, He, $He^+$, $He_2^+$, $He^m$, and $He_2^m$. $O_2 + N_2$ is an intermediary species for reactions involving nitrogen and oxygen ions. For all but

one simulation presented in this work, it was assumed that Penning ionization reactions involving helium and nitrogen are dominant and Penning ionization between helium and oxygen was neglected. The tabulated reaction rates are given in Arrhenius form. For (air) reactions involving electron impact with heavy species, an offline zero-dimensional Boltzmann solver BOLSIG+ [40] was used to obtain a polynomial curve fit of the reaction rates of those reactions versus mean electron temperature (in pure air). The helium electron impact reactions from [117] are given as Arrhenius reactions, and were not explicitly recalculated using BOLSIG+. The production rate due to photo-ionization is dependent on the production rate of $N_2^+$ ions but is otherwise solved independently of the finite-rate chemistry.

## 6.2 Geometric Configuration

### 6.2.1 Imposed He-Air Diffusion Zone

The first set of simulations are for a two-dimensional axisymmetric geometry shown in Fig. 6.1. Pure helium flows through a dielectric tube with a radius between 0.5 to 2 mm. The helium or helium/air mixture (1% air, $O_2$ and $N_2$), issues into a stagnant air ambient at the tube exit (at x = 0 in Fig. 6.1). The simulation domain extends to an axial distance of 2 cm from the tube exit. For prescribed tube exit velocities of the order of 10 m/s the fluid mechanical jet flow remains laminar in practice and the species diffusion mixing layer profile in the air ambient can be approximated as shown in the bottom half of Fig. 6.1. The mixing layer is an important feature of the

jet, since it defines the spatial region where cross reactions between helium and air species can occur. Given the highly disparate velocity scales of the nanosecond plasma discharge phenomena (streamer propagation velocity) and the fluid flow phenomena, it is possible to ignore fluid flow velocity completely in our simulations and to retain only the background species concentration profiles.

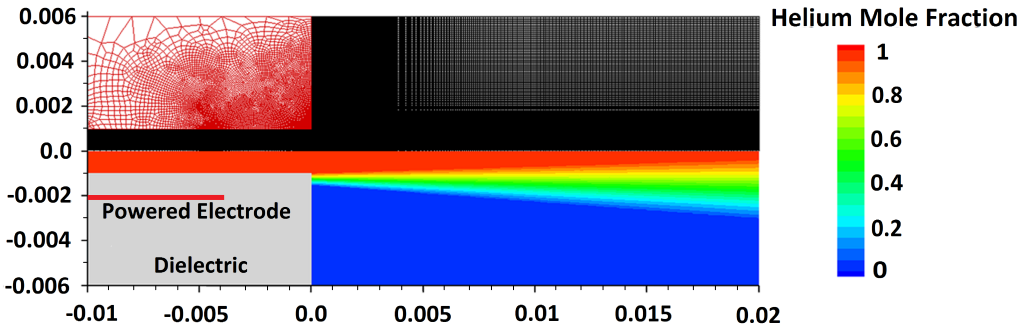


Figure 6.1: Computational mesh and prescribed helium mole fraction in the diffusion zone.

The discharge is generated by a thin embedded foil electrode (10 micrometers thick) in the matrix of the dielectric tube at a radial distance of 2 mm and it terminates 5 mm away from the tube exit (the red line shown in Fig. 6.1). The computation mesh used to discretize the governing equations was generated using a third-party mesher and is shown in the top panel of Fig. 6.1 and comprises a total of 85,000 unstructured cells split among a plasma and a dielectric subdomains. The mesh resolution was determined to be sufficient to describe the cold plasma jet phenomena with the travelling streamer. A 10 kV positive voltage is applied at the embedded electrode to

initiate the plasma discharge. The voltage is applied as a square wave pulse, i.e. the peak voltage is applied instantaneously at the beginning of the simulation and remains constant for the simulation duration (100-200 ns). The electrostatic potential for the far field boundaries of the stagnant air ambient region are grounded for all simulations presented. A discharge generated by a single pulse is simulated; in practice, the pulse is repeated at high repetition rate (typically  kHz) to produce a continuous (albeit pulsed) plasma jet. The jet flow velocity is very low, and some of the metastable and radical products (particularly those with long life times like singlet delta oxygen) will persist through multiple pulses. These species will in turn affect the discharge characteristics of subsequent pulses. Although this affect can be significant, only the very first pulse in a pulse train is considered for this work.

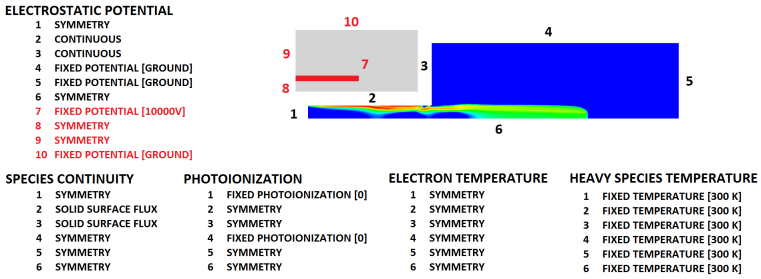


Figure 6.2: Specification of boundary conditions for all conservation equations solved in the dielectric and plasma subdomains.

The boundary conditions of all the governing equations for the cold plasma jet simulation are shown in Figure 6.2. The numbers indicated in black are boundaries surrounding the plasma subdomain while numbers in

red indicate boundaries located around the dielectric subdomain. For the potential equation, the embedded electrode is kept at a constant 10 kV for all simulations while the far field boundaries of the air ambient (4 and 5) act as the ground. For the species continuity equations, solid surface flux boundary conditions were imposed with oxygen secondary electron emission coefficients set to 0.05 and all other ion secondary emission coefficients set to 0.1 along the dielectric while the axis and other boundaries have symmetry boundary condition [25]. Along the walls, it was assumed that all ions, electrons and metastable species are quenched upon impact with the surface. For photo-ionization, symmetry is imposed at the walls and either symmetry or zero photo-ionization in the far field. For the electron temperature, a zero-flux boundary condition is imposed. The background gas temperature was held at a constant 300 K for all simulations. These conditions define a baseline case for the simulation study.

Unlike glow discharges, which are very sensitive to wall effects such as secondary electron emission, streamer discharges do not appear to be very sensitive to wall conditions. In the nanosecond pulse DBD simulations of Unfer and Boeuf [111], it was observed that streamer discharges along dielectric surfaces appear to be insensitive to secondary electron emission. As a test, simulations using an electron energy wall flux boundary condition [25] were performed. The same simulation was performed with the electron temperature wall flux condition changed to a symmetry condition.

### 6.2.2 Plasma Jet Impinging on a Wall

The overall configuration of the simulations consists of an axisymmetric dielectric tube with a thin electrode embedded in the dielectric and a dielectric surface displaced downstream of the tube exit. The powered electrode is 10 micron thick and displaced a distance of 2 mm from the axis of symmetry (1 mm from the tube inner radius). Outside the tube is an ambient air gap region with a solid dielectric surface placed 0.5 and 2 cm from the tube exit. The target surface dielectric is assumed to be 1 mm thick with a dielectric constant of 6.

Figure 6.3 illustrated the overall problem configuration with boundary conditions for the plasma discharge and gas flow for a 2 cm ambient gap and a 1 mm thick dielectric plate. The mesh used for the plasma discharge has approximately 80,000 cells. This configuration acts as the baseline case against which other cases can be compared to.

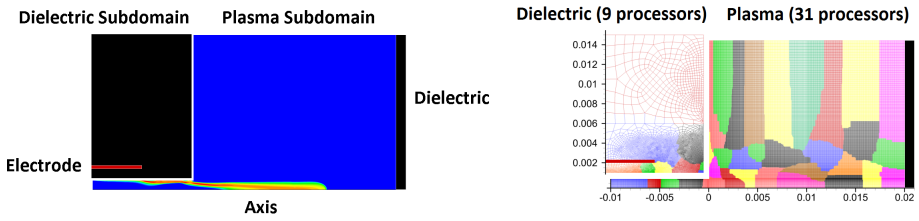


Figure 6.3: Decomposition of solution domain into dielectric and gas (plasma) region is illustrated in the left figure. The right figure illustrates the decomposition of the domain amongst 32 total processors.

For the numerical computations, two distinct subdomains are specified. The plasma subdomain, indicated by the blue region in the top of Figure 6.3,

is the region where the full plasma and flow equations are solved. For the dielectric region, indicated in black with the red dielectric embedded within the region, only the electrostatic potential equation is solved.

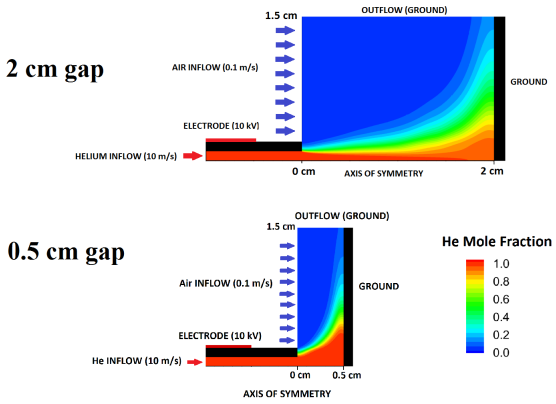


Figure 6.4: Steady state helium mole fraction profile for 2 cm gap (LEFT) and 0.5 cm gap (RIGHT).

The flow and plasma solver boundary conditions along with the steady state helium-air mole fraction profile are shown above in Fig. 6.4. Solid surface flux boundary conditions are imposed on the dielectric (black) surfaces while for the flow the surfaces are modeled as viscous and thermally insulated. A 150 nanosecond, 10 kV trapezoidal pulse with a 10 nanosecond rise and fall time is applied to the embedded electrode. The ambient far field (the outflow and the region behind the target dielectric) acts as the electrical ground.

In addition to the baseline case, three different variations are investigated: a case where the dielectric thickness is increased to 1 cm, a case where the dielectric is placed closer to the tube (0.5 cm vs 2 cm), and a case where

the voltage polarity is switched from positive to negative 10 kV.

## 6.3 Results : Imposed He-Air Diffusion Zone

Fig. 6.5 shows the overall structure of the cold plasma jet for the baseline case. Snapshots of some selected properties: a) electron density, b) ionization rate, c) photo-ionization rate, d) voltage, e) the reduced electric field (i.e. E/N), and f) mean electron temperature, which characterize the discharge, are shown 75 ns after the start of the pulse. A cathode-directed streamer propagates parallel to the geometry axis outside of the dielectric tube. The streamer is a traveling ionization wave without any bulk material transport. At 75 ns, the streamer has propagated to a distance of about 1.2 cm from the tube exit and the radius of the streamer is close to the tube radius of about 1 mm. From Fig. 6.5(a), the peak electron densities in the streamer are seen to be about $10^{20}$ $m^{-3}$ with relatively high electron densities through the entire length of the streamer body (from the streamer head to the interior of the dielectric tube). The total ionization rate (including chemical ionization and photo-ionization) shown in Fig. 6.5(b) is sharply localized at the streamer head with slightly lower ionization rates occurring at the radial edge along the body of the streamer. The peak total ionization rate is about $10^{28}$ $m^{-3}s^{-1}$. The photo-ionization source is also peaked at the streamer head with a peak photo-ionization rate of about 5x$10^{23}$ $m^{-3}s^{-1}$, which is much lower than the total ionization rate. However, photo-ionization occurs over a diffuse region that extends to a significant distance (2 mm) ahead of the streamer

head. The photo-ionization therefore acts as a source of pre-ionization which results in the relatively high electron densities ahead of the streamer head seen in Fig. 6.5(a). The streamer propagation is aided by this photo-ionization process. As shown in our previous work [18], the photo-ionization results in a significant increase in the streamer propagation speed, but it is not essential to streamer propagation. The entire body of the streamer extending from the leading edge (head) of the streamer to the interior of the dielectric tube is nearly equipotential at about 7,500 V. Consequently, the electrostatic field at the head of the streamer is high and the reduced electric fields (Fig. 6.5(e)) are sufficient (about 200 Td) to ionize the gas in front of the streamer head. Utilizing BOLSIG+ [40], it was found that the breakdown threshold for pure He gas is on the order of 10 Td while the breakdown threshold for pure air is on the order of 30-40 Td. Furthermore, for the reduced electric fields typically observed in the streamer/bullet head (200 Td) the ionization rate of pure helium is approximately an order of magnitude greater than the ionization rate in pure air for the same E/N. The presence of photo-ionization generated electrons ahead of the streamer head provides seed electrons to further aid in this electric-field driven ionization within the streamer head. The electron temperature is shown in Fig. 6.5(f) and has a peak value of about 8 eV at the streamer head.

Further insights into the discharge structure can be obtained from Fig. 6.5(b). The peak ionization rate is located off the jet axis and is similar to experimental observations of ring (toroidal) shaped luminous plasma bullets

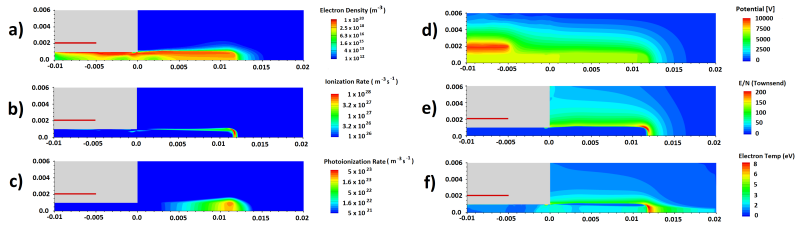


Figure 6.5: Plasma properties 75 ns after start of pulse excitation: a) electron densities, b) total ionization rate, c) air photo-ionization rate, d) electrostatic potential, e) reduced electric fields, f) mean electron temperatures.

[71], [90]. This is in contrast to a streamer propagating in a single component gas (e.g. pure air) where the peak ionization occurs along the axis of the streamer. The off-axis ionization of the streamer begins at the start of the pulse as a surface discharge within the inner walls of the dielectric tube (see Fig. 6.5(a)). This phase of the discharge occurs in the pure helium gas in the tube. Once the surface discharge reaches the tube exit plane (x=0), it transition into a streamer and continues to propagate axially away from the tube, guided by the mixing layer and maintaining the off-axis peak ionization profile for most of its lifetime. Both experiments [49], [60], [109], [71], [90] and models [14] [74], have emphasized the importance of the helium-air mixing layer in guiding the motion of the streamer/plasma bullet off the axis.

A distinctive feature of the mixing layer is the occurrence of cross reactions between helium and air species (e.g., charge exchange and Penning ionization reactions). Fig. 6.6 show line plots of important contributions to the total ionization rate at time 75 ns after start of the pulse (a) along the axial direction and (b) radial direction at the location of the streamer head

(x=1.2 cm). The electron impact ionization of He atom (He + E $\rightarrow$ $He^+$ + 2E) and $N_2$ molecules (E+$N_2$ $\rightarrow$ 2E + $N_2^+$) clearly dominate in the streamer head. The maximum ionization rate occurs off-axis at a radial location of about 0.8 mm from the axis. Penning ionization (green line) is the principal contributor to ionization within the body of the streamer behind the streamer head. This is due to the high density and long life time of metastable helium. Finally, while photo-ionization plays a negligible role within the streamer, its influence extends over a large region in front of and around the propagating streamer head. This creates a low density cloud of seed electrons that significantly modify the speed of the discharge as mentioned earlier. Further observations can be made about the radial location of the streamer head. The peak electron density of the propagating streamer occurs at a location where the air mole fraction is 1-2%, which is consistent with simulation results by Naidis [75] who observed peak electron densities on the 1% air mole fraction line.

To examine the role of these reactions in the streamer propagation, additional simulations (not shown) were performed that disabled all cross reactions between helium and air species ($G37$ to $G40$ in Appendix D). It was seen that the overall structure of the streamer propagation indeed remains unchanged and nearly the same ionization profile is recovered suggesting that the helium-air cross reactions do not play a significant role in the ring shaped-ionization wave [18].

From the above results it is evident that the induced electric field at the head of the streamer plays the key role in its propagation, while its confinement

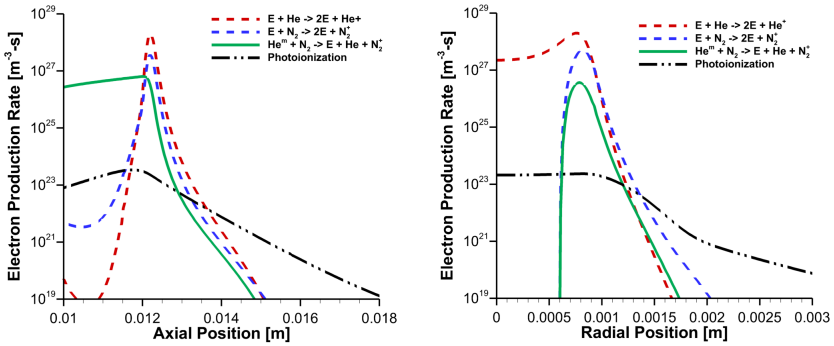


Figure 6.6: Axial and radial variations of contributions to the ionization rates due to different processes 75 ns after the start of the discharge pulse: a) ionization rates along axial direction, b) ionization rates along radial direction at x=1.2 cm.

to the helium core and the distinctive ring shape are due to the fluid mechanical structure of the helium jet with a mixing layer between the helium and air species. The relatively high ionization threshold for air species compared to helium [33] serves to confine the streamer propagation to within the core of the helium jet. A clearer understanding of the role of the helium-air mixing layer is gained by a simulation of the discharge without the presence of the air ambient, i.e. a helium jet issuing into stagnant helium gas. The top panel in Fig. 6.7 shows a snapshot of the electron density for pure helium case 70 ns after the start of the pulse, and the bottom panel is for the baseline case at the same time. In the absence of the air ambient, the plasma surface discharge continues to propagate along the surface beyond the tube exit wall without transitioning into a streamer discharge. This simulation emphasizes the role of air ambient in guiding the streamer away from the tube exit; a feature that

is critical to the remote plasma-type applications for cold plasma jets.

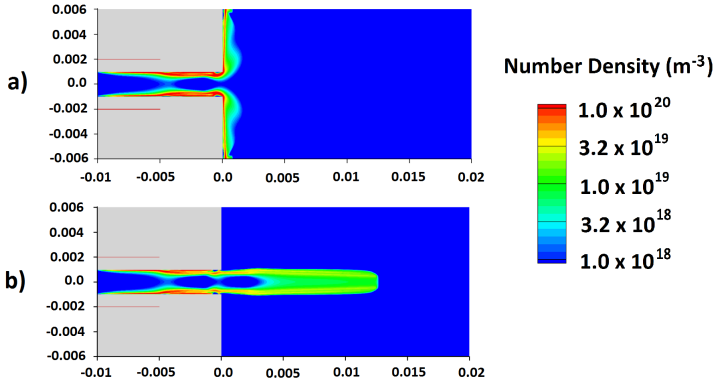


Figure 6.7: Comparison of electron number densities in the plasma discharge structure for a) pure helium ambient, b) helium jet exhausting into air ambient

Fig. 6.8 show a collage of images for the total electron ionization rate as a function of time for the pure helium (top) and helium-air (bottom) cases. During the time the discharge is confined to the tube (up to 30 ns), both cases show identical discharge structure. The top inset image of Fig. 6.8(a) zooms in on the discharge at 20 ns and shows the discharge consists of two distinct ionization regions: a surface discharge driven by charge trapped on the dielectric surface, and a streamer-like discharge away from the wall that is driven by the induced electric field of the space charge in the streamer head. Once the discharge leaves the tube, the pure helium discharge retains the characteristics of a surface discharge as it propagates along the dielectric tube in the axial direction and then turns the corner of the tube and propagates radially along the tube surface. With the air ambient, the discharge transitions into a streamer that moves rapidly along the axial direction as discussed earlier.

The streamer head propagation speed is about 400 km/s, which is consistent with the experimentally observed plasma bullet propagation speed [60].

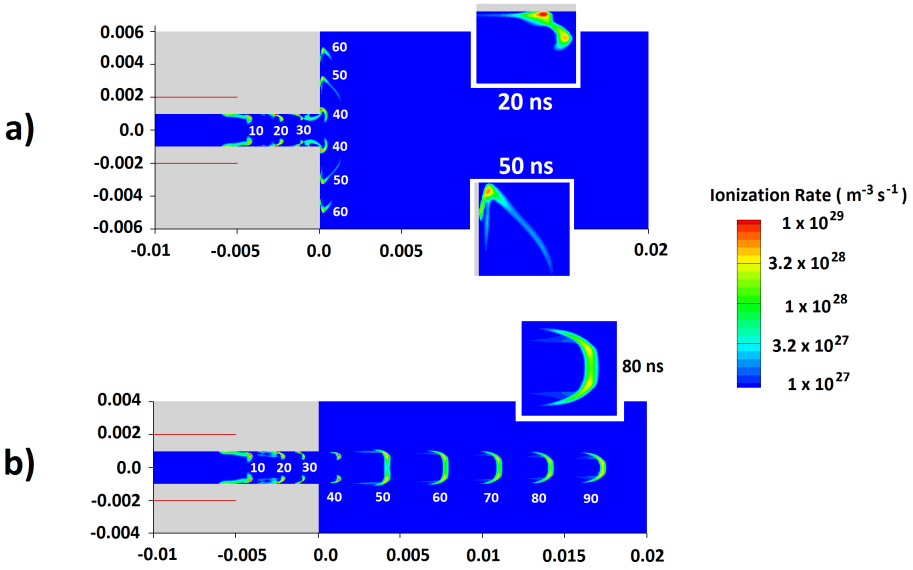


Figure 6.8: Time snapshots of the ionization rate for pure helium (TOP) and helium exhausting into ambient air (BOTTOM).

The streamers are observed to propagate axially out to a finite distance before they are extinguished. Experimental studies have reported the helium mole fraction along the axis at the location of the streamer extinction to be in the range 0.3-0.6 for voltages between 3-7.5 kV [44]. The experiments also report a trend that indicates the helium mole fraction at the axial location where streamer extinguishes decreases with increasing voltage, i.e. the streamer propagates further downstream with increasing voltages. An additional simulation was performed with a significantly larger domain size extending to an axial distance of 8 cm beyond the tube exit (see Fig. 6.9). The on-axis helium mole

fraction at the end of the domain (x = 8 cm) was 0.15 (top panel of Fig. 6.9 shows the helium mole fraction in the domain). The propagation speed of the streamer head and the on-axis helium mole fraction are shown in the bottom panel of Fig. 6.9. As the streamer discharge propagates from the helium core to the region where air densities become significant, the propagation speed of the streamer head is observed to decrease. In addition it was observed from time snapshots of the electron density contours that the radial location of the peak electron densities in the streamer head moves towards the axis, eventually resulting in peak electron densities on axis just prior to extinction. For the electrode voltage of 10 kV, the streamer reaches a maximum axial distance of 4.5 centimeters which corresponds to an on-axis helium mole fraction of 0.8.

### 6.3.1 Role of (Air) Photo-ionization

Fig. 6.10 shows a collage of images for the total electron ionization rate as a function of time for two cases with the photo-ionization model switched ON and switched OFF. The basic phenomena of streamer propagation along the jet axial direction are preserved for both cases. Furthermore, the off axis peak in the ionization rate is observed for both cases. These observations affirm that photo-ionization is not an essential process for streamer propagation in cold plasma jets. However, an important difference between these two cases is the propagation speed of the streamer: the photo-ionization OFF case is significantly slower than the photo-ionization ON case. The photo-ionization OFF case shows a much sharper profile for the ionization rate compared to

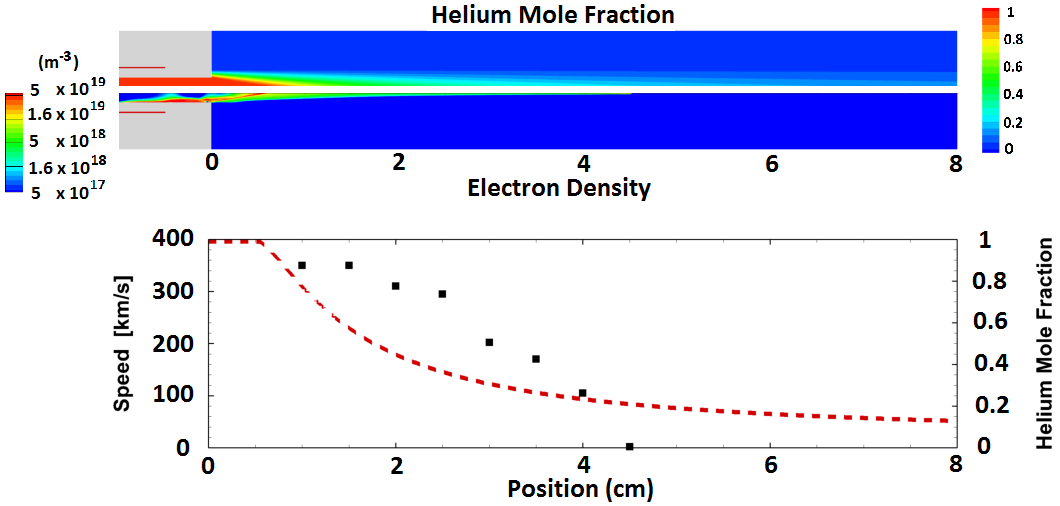


Figure 6.9: Comparison of helium mole fraction (TOP) with electron densities (BOTTOM) after streamer propagation has ceased. The plot displays the streamer head (plasma bullet) speed as a function of axial position compared to helium mole fraction ratio along the center axis. The solid squares are streamer speeds at different gap positions and the red line is the helium mole fraction.

photo-ionization ON case. In the latter case, photo-ionization processes create a weakly ionized plasma cloud ( $10^{12}$-$10^{14}$ $m^{-3}$) surrounding the primary ionization processes in the streamer head. This cloud is responsible for providing seed electrons that significantly enhance streamer propagation speed.

The streamer propagation speeds for cases with photo-ionization switched ON and OFF are shown in Fig. 6.10. The propagation speeds are of 100s km/s, which is consistent with the experimentally observed plasma bullet propagation speed [60]. For the first 30 ns the streamers propagate within the tube and appear to slow down with increasing time. However, the streamers accelerate rapidly once they exit the tube and stabilize to a nearly constant speed

in the ambient. The stable streamer speed in the ambient with the photo-ionization ON is about 400 km/s and almost twice the speed of the streamer with the photo-ionization switched OFF (about 200 km/s)

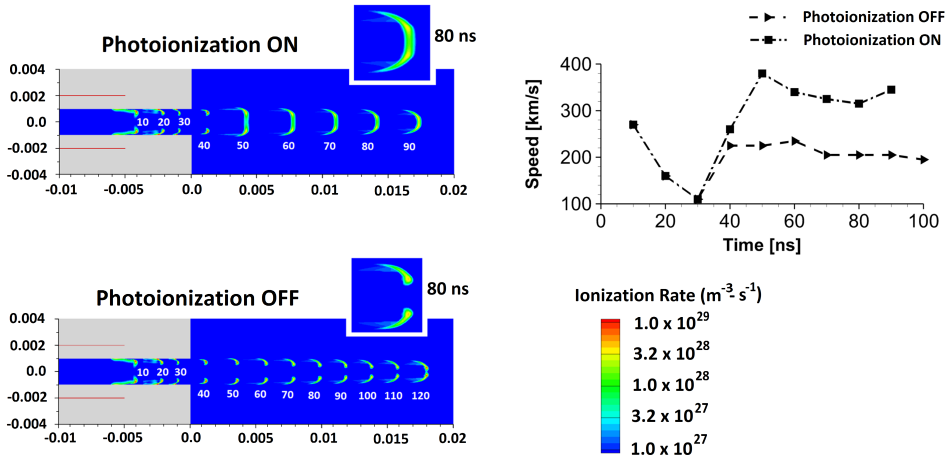


Figure 6.10: A collage of images for the total electron ionization rate as a function of time (in ns) (LEFT) and streamer speeds as a function of time (TOP RIGHT). Top panel is for the model with photo-ionization switch ON and bottom panel is for photo-ionization OFF.

### 6.3.2 Effect of Tube Radius

Because the streamer propagation is highly dependent on the physical shape of the inner core ( 1% air fraction region) of the helium jet, it comes as no surprise that changing the radius of the tube significantly affects the structure and propagation speed of the streamer. In this study, tube with radii of 0.5 mm, 1 mm and 2 mm were compared. Decreasing the tube radius results in streamers that propagate with noticeably higher speeds and plasma densities. As the tube radius is increased to 2 mm and greater, the plasma

propagates primarily along the helium-air mixing layer with very little plasma on-axis and with propagation speeds that are lower than those seen for smaller tube radii.

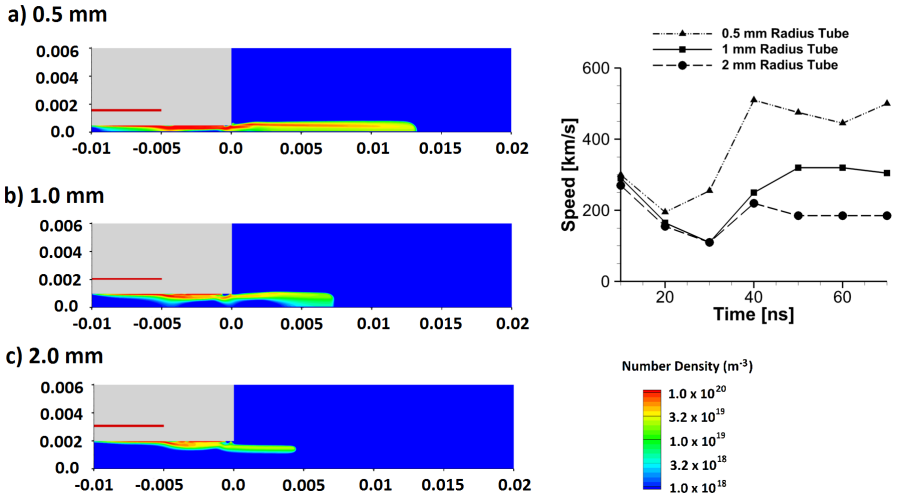


Figure 6.11: Structure of the streamer discharge for varying tube radii. Panels a), b), and c) display electron number densities of the streamer 60 ns after the start of the pulse. The figure on the right shows the streamer head (bullet) speed as a function of time for the three cases.

### 6.3.3 Effect of Mixing Layer Growth Rate

The growth rate of the mixing layer between the helium core and the air ambient depends on the fluid mechanical parameters such as the jet Reynolds number [115]. For increasing Reynolds numbers (higher tube exit velocities) the mixing layer growth rate decreases, meaning that the mixing layer width at any axial location decreases with increasing Reynolds numbers. Fig. 6.12 compares the streamer properties for three cases with a) no mixing layer

growth rate (abrupt boundary between helium and air) b) the baseline mixing layer growth rate used for the simulations in this study, and c) a mixing layer growth rate greater than that used for the baseline simulation. The bottom panels in Fig. 6.12 show the helium mole fraction contours as representative of the mixing layer growth rates. While the growth rate choices for b) and c) are somewhat arbitrary, it is important to note that at any axial location the increased growth rate is accompanied by an increase in the air mole fraction closer to the jet axis. Results indicate that a wider mixing layer width results in a fuller streamer structure with increased charge species densities closer to the jet axis. The streamer head speed is also observed to increase with increasing mixing layer growth rates. The dependency of the streamer speed on the mixing layer width is significantly weaker than the dependency on the tube radius. There are two physical mechanisms which could explain the observed speed increase. The first is the greater role that photo-ionization plays when the region of mixed air and helium is enlarged. The other, more likely explanation, is that as the mixing layer width increases, the radius of the inner helium core, which corresponds to the region where the helium-air ratio is 99%, decreases. As was seen when varying the tube radius, a decreasing helium core radius results in increasing streamer speeds. From this, it is concluded that the width of the mixing layer itself does not play a significant role in the kinetics of streamer propagation as long as a significant helium core (almost 100% helium mole fraction) region exits.

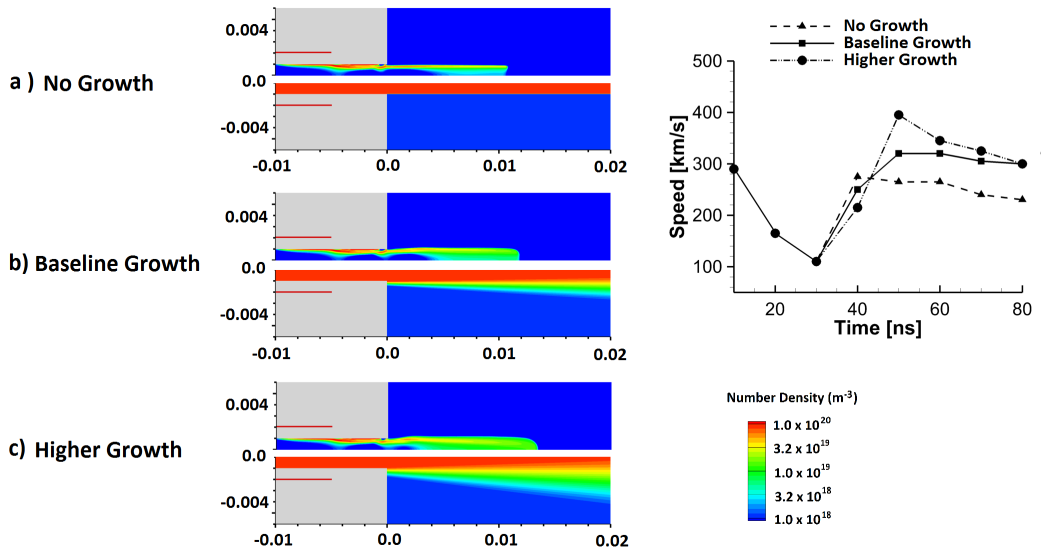


Figure 6.12: Electron density (TOP) and helium mole fractions (BOTTOM) for varying mixing layer growth rates. a) no growth, b) baseline growth, and c) high growth. Time snapshots of electron density are taken 75 ns from the start of the pulse. The figure on the right shows the streamer head (bullet) speed as a function of time for the three cases.

### 6.3.4 Role of Trace Impurities

Another parameter investigated is the role that trace impurities within the helium core have on the overall kinetics of the discharge. Different cases investigated include adding 1% air, 1% pure nitrogen ($N_2$) and 1% pure oxygen ($O_2$) impurities to the helium background. The initial helium densities are modified to 99% of their original value plus 1% of whichever impurity is being added. The number density ratio of the ambient air remains unchanged.

The resulting electron density profiles and streamer propagation speeds are shown in Fig. 6.13. The impurities are expected to have two principal

effects on the kinetics of the discharge. First, the presence of $O_2$ and $N_2$ impurities creates loss pathways for electron energy via electron collisions with these molecules to create vibrationally and electronically excited molecules. Less energy is thereby available for plasma formation through electron impact ionization. Also, oxygen is an electronegative gas and can deplete electrons via attachment reactions. These factors suggest that nitrogen and oxygen impurities will have an adverse effect on plasma formation. The second effect of impurities, when both oxygen and nitrogen impurities are present simultaneously (e.g. for air), is the occurrence of photo-ionization within the helium core which in turn produces seed electrons over a larger volume, potentially increasing the charge density and speed of the streamer.

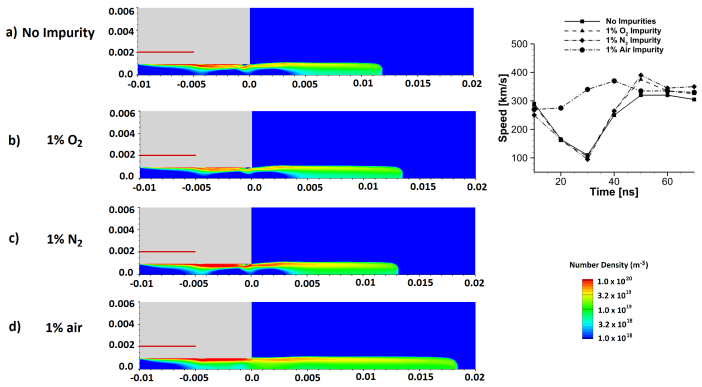


Figure 6.13: Electron density profiles after 75 ns from the start of the pulse, with different impurities in the helium jet core. The figure on the right shows the streamer head (bullet) speed as a function of time for varying impurities within the helium core.

For the first 30 ns after the pulse is turned on, corresponding to discharge propagation within the tube, it is seen that adding only pure $O_2$ or

pure $N_2$ has results in a very small decrease in streamer propagation speed. Adding air impurity ($N_2$ and $O_2$) results in a significant speed-up of the discharge propagation within the tube itself, and the plasma forms over a larger volume within the tube compared to the other cases. Outside the tube, the impurities result in a slight increase in streamer propagation speed. From these observations, it appears that the air impurity (mixture of oxygen and nitrogen) plays a significant role during the initial surface discharge phase in the dielectric tube. Once the discharge leaves the tube, the large amount of air from the ambient overwhelms the presence of trace impurities in the helium and only a small increase in streamer propagation speed is observed.

### 6.3.5 Electrode Thickness

The final parameter investigated in this study is the geometry of the powered electrode used to initiate the discharge in the dielectric tube. The objective is to determine how much of an impact the configuration of the electrode has on the formation of the discharge inside and outside of the dielectric tube. Both the electrode thickness and the vertical displacement of the electrode were varied to determine what effect the electrode placement and hence the externally applied potential field has on the formation of the streamer. Fig. 6.14 displays snapshots of the electrode densities 75 ns into the simulation. Fig. 6.14(a) through 6.14(c) show the streamer electron densities for varying the thickness of the electrode from 10 micrometers to an infinite electrode. Fig. 6.14(d) shows an electrode with the same thickness as Fig.

6.14(a) (baseline), but embedded at a greater radial distance of 3 mm from the axis (baseline case is for an electrode at a radial distance of 2 mm). It was observed that only the initial stages of discharge formation in the tube is affected by the electrode thickness. Thinner electrodes have greater electric field concentration at the electrode edge which results in plasma breakdown occurring earlier in the tube and larger peak plasma densities within the tube. Outside of the tube however, there is no discernible difference in the streamer propagation speed or its structure. When the electrode is shifted 1 mm away from the inner tube (Fig. 6.14(d)), breakdown occurs later compared to the baseline case. Once the streamer leaves the tube however, the structure and speed of the streamer head are unchanged compared to the default configuration. It is therefore apparent that the physical shape of the embedded electrode has some effect during the initial stages of the discharge formation within the dielectric tube, but has little to no effect on the streamer discharge once it leaves the tube.

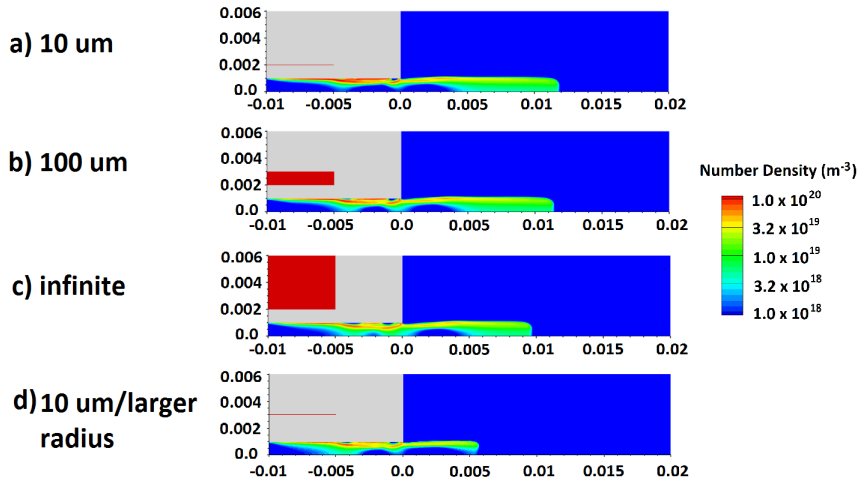


Figure 6.14: Electron densities for varying electrode geometries in discharge, 75 ns after the pulse is initiated.

## 6.4 Results : Plasma Jet Impinging on a Wall

For the simulation cases presented, the plasma discharge and propagation has three distinct stages: propagation in the dielectric tube, propagation in the ambient gap, and propagation adjacent to the target dielectric surface.

For the baseline case, a single fast ionization wave discharge event is analyzed over the duration of a one pulse. Before applying the voltage pulse, the flow solver is used to obtain the steady state laminar flow profile. The resulting helium-air mole fraction profile at steady state is shown in Fig. 6.4. Note that the mole fraction profile is crucial as it guides the subsequent discharge and determines when it will cease to propagate once the air-helium mole ratio exceeds a certain value.

The plasma discharge has three to four distinct stages that it under-

goes as it propagates from the dielectric tube to the dielectric surface. The different stages of the discharge from formation within the dielectric tube and its impingement and propagation along the surface are illustrated in Fig. 6.15.

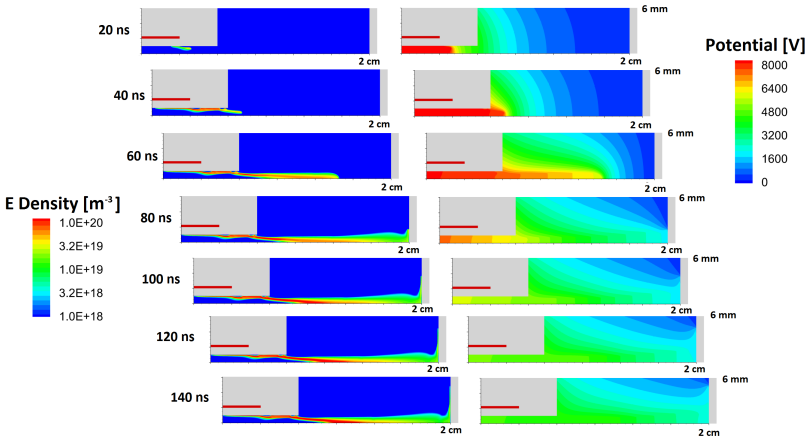


Figure 6.15: Electron density time shots (LEFT) and electrostatic potential time shots (RIGHT) for 2cm cm gap, 1 mm thick dielectric case.

During the first 30 nanoseconds of the discharge, the plasma is confined entirely to the dielectric tube. Gas breakdown begins approximately 10-20 nanoseconds after the pulse is applied. There are two distinguishable ionization zones that propagate along the tube edge. The first is located directly adjacent to the surface and is driven by charge trapping on the dielectric surface. The second ionization wave is offset above the surface discharge and is a driven by space charge produced in the streamer head.

Between 30 and 40 nanoseconds, the streamer and surface discharge reach the tube exit. The surrounding ambient air prevents the surface discharge from propagating along the outer tube edge while the streamer dis-

charge continues to propagate off axis along the 0.99 helium-air ratio line. At this point, the ionization wave region has the distinctive toroidal shape referred to as a plasma bullet in the literature. After 60 nanoseconds, the plasma bullet ionization wave profile peaks along axis and loses its toroidal shape.

Between 70 and 80 nanoseconds, the plasma bullet reaches the dielectric surface. Charged particle species are fluxed to the wall and embedded as trapped charge. As a result of charge trapping, the discharge continues to propagate adjacent to the surface. It is during this phase that most of the reactive radicals and charged species are deposited to the dielectric surface. The surface discharge covers a distance of approximately 4 mm from the axis before the ambient air quenches the discharge and it ceases to propagate. The ratio of helium-air at the point where the discharge ceases to propagate is 0.66.

### 6.4.1 Radical Production

Snapshots of the O, N, O2a1 (singlet delta oxygen) and $O^3$ radical densities after 100 ns of simulation time are shown in Fig. 6.16. The peak radical species densities are roughly: O ($10^{22}$ $m^{-3}$), N ($10^{20}$ $m^{-3}$), SDO($10^{21}$ $m^{-3}$) and $O_3$ ($10^{20}$ $m^{-3}$). The radicals can be further split these radicals into two types: short lived radicals such as O and N and longer lasting radicals such as singlet delta oxygen and ozone. Because the flow speeds are so low ($< 10$ m/s) one would not expect any of the short lived radicals (O and N) to reach the target surface before recombining. Singlet delta oxygen and ozone

on the other hand, have much longer lifetimes and it is likely that these species will persist between pulses and can may eventually be convected to the target surface by the gas flow.

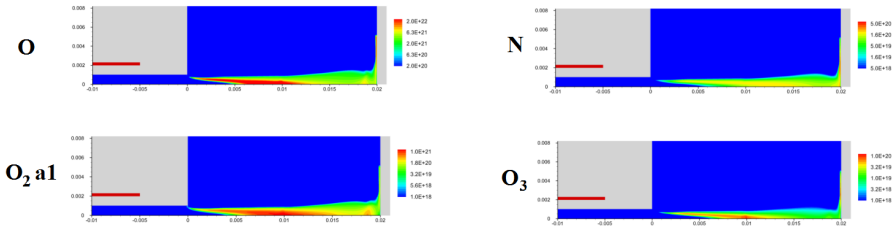


Figure 6.16: Time snapshots of radical species in the ionized trail of the plasma jet after 100 ns of simulation time.

Once the ionization wave reaches the target dielectric, it propagates radially outward and adjacent to the dielectric surface. As the plasma discharge propagates parallel and adjacent to the target dielectric, charged and reactive radical species are delivered to the surface. Fig. 6.17 compares the positive, negative and radical species fluxes to the dielectric surface at a given instant (100 ns) after the start of the simulation after the surface discharge has begun to propagate over the target surface.

The principal species delivered to the surface are O radicals. N, NOx and $O^3$ radicals are produced by the surface discharge but their fluxes to the surface are negligible compared to O radical fluxes. The dominant positive charge carrier delivered to the surface is $O_4^+$ ions with peak wall impact energies on the order of 1.3 eV. The dominant negative charge carrier delivered to the surface is electrons with peak wall impact energies on the order of 0.4 eV.

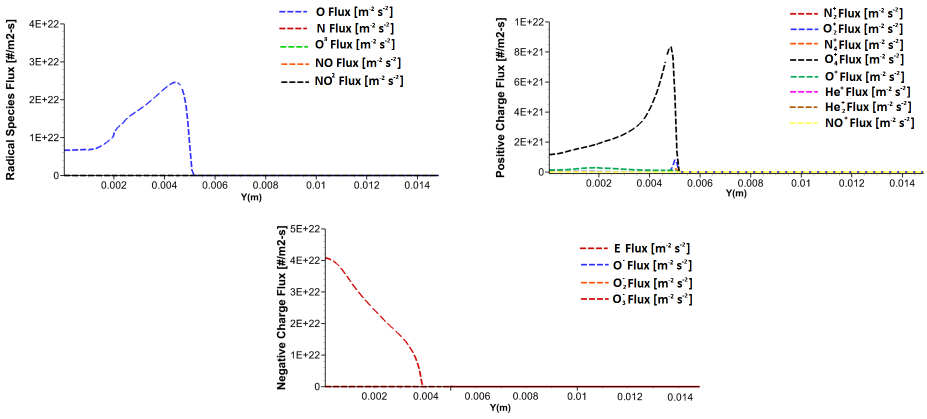


Figure 6.17: Positive charge flux, negative charge flux and radical flux to dielectric surface 100 ns after pulse initiation.

### 6.4.2 Dielectric Thickness - 1mm vs 1 cm

Next, the baseline case is compared to a simulation case where the target surface dielectric thickness is increased from 1 mm to 1 cm. The formation of the plasma from the dielectric tube, across the gap and along the surface is illustrated below in Fig. 6.18.

propagation in the tube and across the gap is virtually identical to the baseline case. When the chemically active ionization zone approaches the surface it does not transition to a surface discharge. From Fig. 6.18 one can see that the discharge appears to follow the contour helium-air stagnation jet instead of making contact with the surface. The ionization wave propagates parallel to the target surface, but is offset by a distance of approximately 0.5-1 mm. It appears then, that placing the ground plane closer to the surface is important in that it allows the discharge to make the transition to the surface.

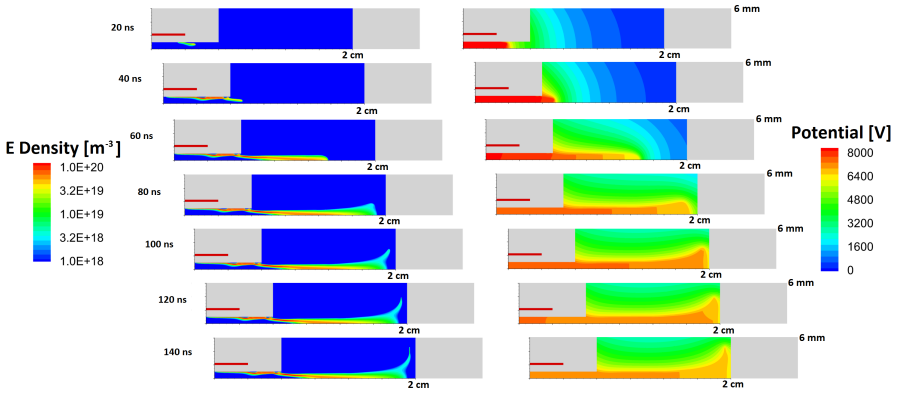


Figure 6.18: Electron density time shots (LEFT) and electrostatic potential time shots (RIGHT) for 2 cm cm gap, 1 cm thick dielectric case.

The offset of the propagating ionization wave from the target surface results in the delivery of significantly fewer radicals and charge carriers to the surface compared to the thinner dielectric case (see Fig. 6.20).

### 6.4.3 Gap Thickness - 0.5 mm vs 2 cm

The final case considered is for an APPJ placed closer to the surface of interest. The gap distance between the tube exit and the dielectric surface is reduced from 2 cm to half a cm. The most significant change that results from changing the gap distance is a different flow profile and more importantly, a different helium-air mole fraction profile.

First note that greater quantity of helium near the surface for the 0.5 cm case compared to the 2 cm case. Comparing the plasma to the base test case, two key differences are observed. The first is that the plasma jet impacts the surface significantly earlier than for the baseline case (40 ns versus 75 ns)

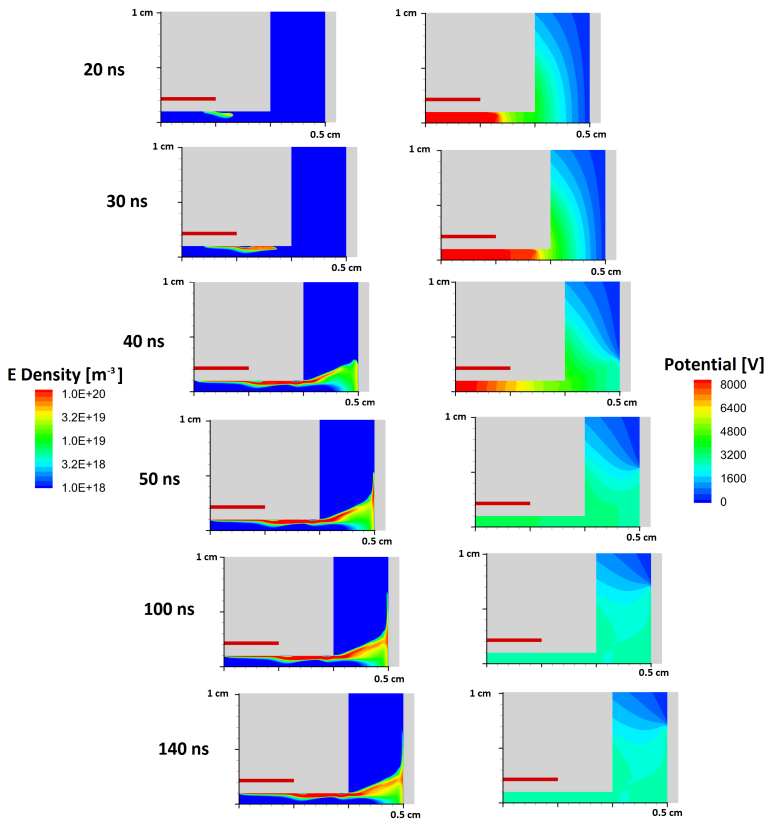


Figure 6.19: Electron density time shots (LEFT) and electrostatic potential time shots (RIGHT) for 0.5 cm gap, 1 mm thick dielectric case.

as is expected. The surface discharge that propagated over the target dielectric surface also covers a larger distance (6 mm radii) versus the baseline case (4 mm radii).

### 6.4.4 Comparison of Net Species Fluxes

The first thing that should be noted is that Fig. 6.20 is on a log scale, so differences in flux quantities are exaggerated. It is seen that the 0.5 cm gap

case, because of the closer proximity of the tube to the target surface, delivers radical and charged species to the surface far earlier than the 2 cm gap test cases. In addition, the peak O radical flux is greater than the baseline case. The net quantity of radicals and ions delivered to the surface is proportional to the integrated area under each curve. From Fig. 6.20 it can be seen that the 0.5 cm gas case delivers significantly more O radicals and ions to the surface than the 2 cm case. It was previously mentioned that by increasing the dielectric surface thickness, the electrostatic potential profile changed and instead of propagating directly on the surface as for the 1 mm thick case, the plasma propagated parallel to the surface at a distance of approximately 1 mm from the surface. The result is that the net flux of radicals and charged species to the surface is lowered by 5-6 orders of magnitude.

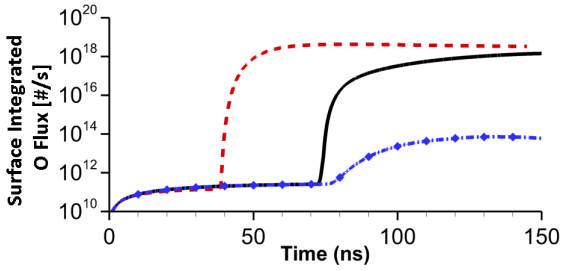


Figure 6.20: Comparison of the net integrated flux of O radicals on the target dielectric surface over the pulse interval (150 ns). Note the legend is log scale.

## 6.5 Summary and Conclusions

### 6.5.1 Imposed He-Air Diffusion Zone

The plasma discharge comprises a streamer (ionization wave) also called a plasma bullet generated by the start of an excitation pulse at an electrode that is embedded within or in the vicinity of a dielectric tube that carries the helium noble gas. The streamer is sustained by high (above threshold) electric fields that drive electron impact reactions. The mixing layer region where the helium core gas inter-diffuses with the ambient air is necessary to realize a streamer (bullet) that propagates parallel to the jet axis. Without the presence of air or some other gas that has higher breakdown threshold than the jet core gas, the plasma discharge from the tube will not propagate into the open gap and remains confined to the dielectric wall as a surface discharge.

Discharge geometric and operating parameters such as tube radius, jet Reynolds number (mixing layer growth rate), and electrode geometry and chemical process parameters such as Penning ionization reactions, the (air) photo-ionization process, and impurities in the jet core gas, were all found to have an effect on the streamer speed and the structure of the streamer to varying degrees. Photo-ionization has a significant impact on the speed of the streamer propagation but is not essential to streamer propagation. Penning ionization reactions also have an impact on streamer propagation although not to as great a degree as (air) photo-ionization. It was found that adding impurities and changing the electrode configuration have the greatest impact on the discharge while it is still confined to the dielectric tube. Adding air

impurities results in a significant increase in the propagation of the discharge in the tube, but otherwise has little effect on the discharge once it emerges as a propagating streamer in the ambient.

It was found that modifying the radius of the tube and the helium exhaust jet significantly modifies the streamer propagation speed and the plasma structure to a lesser degree. For larger radii, the plasma remains confined almost entirely in the mixing layer and propagates at lower speeds. For smaller tube radii, the streamer speed increases noticeably and the density of the plasma near the axis is also increased.

The diffusional mixing layer growth rate (width at any axial location) has a moderate effect on the bullet propagation. Widening the mixing layer at any axial location results in a modest increase in streamer speed and a slightly wider plasma profile. It is apparent however, that having a finite mixing layer width is not essential to streamer propagation. This is in agreement with simulations by Naidis ( [74] and Boeuf et al. [14] both of which successfully modeled streamer propagation without a finite width mixing layer.

Changing the powered electrode geometry changes the voltage gradients within the tube, which affects the breakdown and propagation of the surface discharge within the tube. Once the discharge leaves the tube however, the streamer structure and speed is relatively unaffected by the electrode geometry.

### 6.5.2 Plasma Jet Impinging on a Wall

To summarize, a two-temperature plasma model has been coupled with a compressible flow solver to simulate the plasma discharge in an atmospheric pressure helium jet impinging on a solid surface. Pure helium with an inlet velocity of 10 $m/s$ (1.885 liters/min) was exhausted into ambient air where a steady state laminar flow solution of the jet impinging on a solid wall was obtained. A 10 kV, 150 ns pulse with rise/fall time of 10 ns was then applied at the powered electrode. The resulting plasma discharge took the form of a fast ionization wave that propagated from within the tube, out into the helium jet and to the surface of the dielectric. The resulting charge and reactive species produced within the discharge and delivered to the target surface as fluxes were quantified and presented.

It was found that the entire discharge even for a single pulse has three discernible stages. The first stage consists of propagation within the dielectric tube, where the discharge takes the form of both a surface driven discharge and an ionization wave driven by electron impact ionizations. The second stage of the discharge begins when the ionization wave propagates out into the open air gap. The ionization wave is confined to the helium jet where it propagates along the helium-air mole fraction line and eventually along the axis until the discharge reaches the target. The final stage of the discharge is characterized by a change in direction of propagation from along the axis to radially outwards and parallel to the target surface. If the thickness between the dielectric and the ground is small enough, the discharge will reach the surface and propagate

adjacent to the surface until the fraction of air in the ambient is great enough to quench the ionization wave. If the ground is placed far enough behind the dielectric surface, the discharge does not reach the surface. Instead, it follows the contour of the helium-air jet diffusion zone until it eventually propagates parallel to but no longer adjacent to the target surface.

Peak radical production was observed in the region of the helium jet where a discernible pure helium core (region of 1.0 helium mole fraction) exists. For species that have long lifetimes, particular singlet delta oxygen, it is possible that bulk flow convection can carry these species produced in the hap to the target surface over longer timescales and subsequent pulses. Most of the short lived species, such as O and N and charged particles, are produced on site by the ionization wave as it propagates adjacent to the surface where they flux to the target surface. It was found that the dominant radical species delivered to the surface by the discharge as it propagates adjacent to the surface was O radicals.

Varying the dielectric thickness, or more specifically, varying the location of the ground plane behind the dielectric significantly impacts the behavior of the discharge and the subsequent production and delivery of radicals. For thin dielectrics (e.g. 1 mm), the discharge can reach the target surface and deliver radical and charged species to the surface. For thick dielectrics (e.g. 1 cm), the discharge does not reach the target surface and the net flux of radicals is lower by several orders of magnitude. Varying the gap distance impacts the profile of the helium jet. Shortening the gap distance increases the

area of coverage over which radical species are delivered, although the peak magnitudes of the fluxes remain approximately the same order of magnitude.

# Chapter 7

# Conclusions

A two-temperature plasma fluid model with self-consistent electrostatic fields was coupled with a compressible Navier-Stokes solver to investigate several problems of interest. The primary challenge in solving such coupled systems of equations is the large disparities in time and length scales and the consequent stiffness of the equations. Simulation speedup is achieved by solving the governing equations in parallel using a domain decomposition approach. Numerical studies of streamer discharges were performed for applications including non-equilibrium plasma ignition enhancement, flow actuation, and atmospheric pressure non-equilibrium plasma jets.

## 7.1 Plasma Assisted Ignition and Combustion

Simulations of nanosecond pulsed discharges in supersonic $O_2-H_2$ mixtures using a powered electrode embedded in a dielectric material were performed. Anodic and cathodic pulses at voltages ranging from 4 kV to 8 kV were studied. A comparison of pulsed discharges in premixed $O_2-H_2$ stream with a pure argon stream was made to quantify the effect of reactive chemistry in these discharges. For both gases, the anodic pulse forms cathode

directed streamers which propagate away from the electrode. The cathodic pulse plasma forms as a surface discharge which propagates over the adjacent dielectric surface due to charge trapping, with the dielectric itself acting as a virtual electrode. Increasing voltage results in an increase in plasma propagation distance, peak species number densities, and gas heating for anodic and cathodic pulses.

Oxygen radicals are the dominant species produced in the 4 kV anodic and cathodic pulses. The impact of the flow field is to advect O radicals downstream of the discharge region over microsecond timescales. Rapid gas temperature increase of hundreds of Kelvin due to ion Joule heating results in micro blast waves for both anodic and cathodic $O_2-H_2$ pulses. Gas heating was higher for the cathodic pulse. Anodic pulse streamers are found to propagate a greater distance from the dielectric surface compared to the cathodic pulse streamers, which remain in contact with the surface throughout their lifetime. Consequently, it is expected that radical species produced by anodic pulsed streamers are less likely to be quenched at the surface and can be carried further into the free stream where they can participate in combustion enhancement processes, i.e. anodic pulsing is a more efficient strategy for combustion enhancement using surface mounted pin electrodes.

Simulations of corona discharges at high pressures (10 atm) in methane-air mixtures were performed for both short gap (2.8 mm) and long gap (4 cm) cylindrical geometries with an inner powered electrode and a grounded outer shell. For the short gap simulations, it was found that the plasma bridges the

gap after approximately 10 nanosecond and is followed by a secondary streamer that forms in the plasma channel left behind by the primary streamer. Most of the radicals (particularly O radicals) are formed in the secondary streamer channel and are localized near the anode which is consistent with experimental observations. For the long gap simulations, the plasma propagates as a single long streamer. While the plasma produces a relatively uniform density channel of O radicals, peak radical production is localized near the prong tip where the electric fields are highest. For both the long and short gap simulations, varying the fuel-air ratio has little impact on the plasma discharge or radical yield other than slightly modifying the ratios of the oxygen to fuel radicals. The net radical yield is greater for the corona discharge than for the coaxial discharge, though the width of the corona streamer (approx. 40 microns) is less than the coaxial streamer (approx. 200 microns). The resulting simulations are consistent with experiments using similar geometries where it was observed that ignition kernels form near the high reduced electric fields of sharp geometric features such as pins or roughness elements.

## 7.2 Atmospheric Pressure Plasma Jets

Atmospheric pressure plasma jet are a type of atmospheric pressure discharge that are formed by flowing a noble gas such as argon through a thin (mm) tube into ambient air. High voltage pulsed or sinusoidal wave forms are applied to a powered electrode placed on the tube and the plasma forms due to a sequence of streamers that propagate in the exhaust plume of the noble

gas. To the naked eye, the rapid succession of streamers give the discharge the appearance of a continuous luminous jet. The streamer is sustained by high (above threshold) electric fields that drive electron impact reactions. The mixing layer region where the helium core gas inter-diffuses with the ambient air is necessary to realize a streamer (bullet) that propagates parallel to the jet axis. Without the presence of air or some other gas that has higher breakdown threshold than the jet core gas, the plasma discharge from the tube will not propagate into the open gap and remains confined to the dielectric wall as a surface discharge.

Discharge geometric and operating parameters such as tube radius, jet Reynolds number (mixing layer growth rate), and electrode geometry and chemical process parameters such as Penning ionization reactions, the (air) photo-ionization process, and impurities in the jet core gas, were all found to have an effect on the streamer speed and the structure of the streamer to varying degrees. Photo-ionization has a significant impact on the speed of the streamer propagation but is not essential to streamer propagation. Penning ionization reactions also have an impact on streamer propagation although not to as great a degree as (air) photo-ionization. It was found that adding impurities and changing the electrode configuration have the greatest impact on the discharge while it is still confined to the dielectric tube. Adding air impurities results in a significant increase in the propagation of the discharge in the tube, but otherwise has little effect on the discharge once it emerges as a propagating streamer in the ambient.

Modifying the radius of the tube and the helium exhaust jet significantly modifies the streamer propagation speed and the plasma structure to a lesser degree. For larger radii, the plasma remains confined almost entirely in the mixing layer and propagates at lower speeds. For smaller tube radii, the streamer speed increases noticeably and the density of the plasma near the axis is also increased. The diffusional mixing layer growth rate (width at any axial location) has a moderate effect on the bullet propagation. Widening the mixing layer at any axial location results in a modest increase in streamer speed and a slightly wider plasma profile. A finite mixing layer width is not essential to streamer propagation. This is in agreement with simulations by Naidis ( [74] and Boeuf et al. [14] both of which successfully modeled streamer propagation without a finite width mixing layer. Changing the powered electrode geometry changes the voltage gradients within the tube, which affects the breakdown and propagation of the surface discharge within the tube. Once the discharge leaves the tube the streamer structure and speed is relatively unaffected by the electrode geometry.

For the case of a plasma jet impinging on a solid surface, it was found that the entire discharge for a single pulse has three discernible stages. The first stage consists of propagation within the dielectric tube, where the discharge takes the form of both a surface driven discharge and an ionization wave driven by electron impact ionizations. The second stage of the discharge begins when the ionization wave propagates out into the open air gap. The ionization wave is confined to the helium jet where it propagates along the helium-air

mole fraction line and eventually along the axis until the discharge reaches the target. The final stage of the discharge is characterized by a change in direction of propagation from along the axis to radially outwards and parallel to the target surface. If the thickness between the dielectric and the ground is small enough, the discharge will reach the surface and propagate adjacent to the surface until the fraction of air in the ambient is great enough to quench the ionization wave. If the ground is placed far enough behind the dielectric surface, the discharge does not reach the surface. Instead, it follows the contour of the helium-air jet diffusion zone until it eventually propagates parallel to but no longer adjacent to the target surface.

Peak radical production was observed in the region of the helium jet where a discernible pure helium core (region of 1.0 helium mole fraction) exists. For species that have long lifetimes, particular singlet delta oxygen, it is possible that bulk flow convection can carry these species produced in the hap to the target surface over longer timescales and subsequent pulses. Most of the short lived species, such as O and N and charged particles, are produced on site by the ionization wave as it propagates adjacent to the surface where they flux to the target surface. It was found that the dominant radical species delivered to the surface by the discharge as it propagates adjacent to the surface was O radicals.

Varying the location of the ground plane behind the dielectric significantly impacts the behavior of the discharge and the subsequent production and delivery of radicals. For thin dielectrics (e.g. 1 mm), the discharge can

reach the target surface and deliver radical and charged species to the surface. For thick dielectrics (e.g. 1 cm), the discharge does not reach the target surface and the net flux of radicals is lower by several orders of magnitude. Varying the gap distance impacts the profile of the helium jet. Shortening the gap distance increases the area of coverage over which radical species are delivered, though the peak magnitudes of the fluxes remain approximately the same order of magnitude.

# Chapter 8

# Contributions and Future Work

Contributions to current research including publications as well as suggestions for future work are discussed in this chapter.

## 8.1 Research Contributions

### 8.1.1 Code Development

Contributions included development and optimization of pre-existing plasma fluid solver and compressible Navier-Stokes solver. An approximate photo-ionization model for air was implemented in parallel to model the production of seed electron charge produced by propagating streamers. The compressible Navier-Stokes solver was expanded from single species to a multi-species configuration and then coupled to the plasma solver. Optimization of the parallel plasma solver code on the Lonestar supercomputer to solve problems with several hundred cores. Performed strong and weak scaling studies on the Lonestar supercomputer to determine portions of the code requiring further optimization for parallel speedup.

### 8.1.2 Chemistry Mechanisms

For the problems of interest, multiple chemistry mechanisms were compiled from pre-existing literature. For supersonic flow ignition, an $H_2$-$O_2$ plasma mechanism was compiled. For investigations of plasma enhanced ignition in high pressure internal combustion engines a methane-air plasma chemistry was compiled. For atmospheric pressure plasma jets, a He-Air plasma chemistry was compiled.

### 8.1.3 Research Applications

Performed investigation of non-equilibrium plasma discharge for supersonic ignition and flow control applications. Performed numerical investigation of non-equilibrium plasma discharges in methane-air mixtures at very high pressures for both short gap and long gap axial electrode geometries. Performed numerical investigation of the kinetics of atmospheric pressure plasma jet formation and propagation in open air gaps and for plasma jets impinging on solid surfaces.

## 8.2 Publications

1. D. Breden and L.L. Raja, *Gas Heating Effects in a Nanosecond-Pulse Streamer Discharge Interacting with a Supersonic $O_2$-$H_2$ Flow*, IEEE Transactions on Plasma Science, 0093-3813, 2011, doi:10.1109/TPS.2011.2158323

2. D. Breden and L.L. Raja, *Simulations of Nanosecond Pulse Plasmas in Supersonic Flows for Combustion Applications*, AIAA Journal, Vol. 50, No.

3, Mar. 2012, doi: 10.2514/1.J051238

3. D. Breden, K. Miki and L.L. Raja, *Computational Study of Cold Atmospheric Nanosecond Pulsed Helium Plasma Jet in Air*, Applied Physics Letters 99, 11501, 2011, doi:10.1063/1.3636433

4. D. Breden, K. Miki and L.L. Raja, *Self-Consistent Two-Dimensional Modeling of Cold Atmospheric-Pressure Plasma Jets/Bullets*, Plasma Sources Science and Technology, Vol. 21, 034011 (13pp), 2012, doi:10.1088/0963-0252/21/3/034011

5. D. Breden, L. L. Raja, C.A. Idicheria, P. M. Najt and S. Mahadevan, *A Numerical Study of High-Pressure Non-Equilibrium Streamers for Combustion Ignition Application*, Journal of Applied Physics, 2013, *In Review.*

## 8.3 Future Work

Suggestions for future work include both expanding and improving the existing numerical models as well as suggestions for further research in the problems investigated in this work.

### 8.3.1 Code Development

For code development, it was determined that the electrostatic Poisson equation of the plasma solver is the limiting factor when attempting to solver problems on large numbers (hundreds) of processors simultaneously. Significant communication slow down occurs due to communications required by the

electron predictor step. It is recommended that the implementation either be modified to reduce/eliminate communications or to allow the option of disabling the predictor step for certain classes of problems. The second source of slow down is due to the time required to assemble and solve the linear system. The numerical stiffness of the problem necessitates many search iterations when using the default solver option (GMRES) along with the default pre-conditioner (block Jacobi). The solve step can be improved by utilizing by implementing a better parallel pre-conditioner such as an algebraic multi-grid pre-conditioner. The assembly portion of the Poisson equation A matrix (and all other equations) that each processor performs can be sped up by implementing support for shared memory parallelization using a co-processors such as a GPU in tandem with the MPI domain decomposition approach already implemented.

Remaining issues for code development include implementing photoionization models for processes other than air (e.g. helium photons ionizing oxygen). The Navier-Stokes solver can be expanded to include finite rate kinetics for neutral species such as neutral combustion reaction mechanisms. The plasma solver could then be responsible for solving the short time scale kinetics of plasma chemistry while the Navier-Stokes solver would be responsible for solving longer time scale neutral reaction kinetics such as neutral species combustion reactions.

In the long term, adaptive mesh refinement implementation would be advantageous for modeling processes where the plasma structure varies con-

siderable in time and space over the domain which is the case when modeling propagating streamers. In theory, only mesh cells in the vicinity of the streamer head need to be refined to the order of the Debye length while cells in the neutral bulk plasma and the rest of the domain can be much larger without sacrificing accuracy.

### 8.3.2 Research Applications

Following the numerical investigations presented in this work, there are two pathways which could be pursued.

The first involves non-equilibrium plasma ignition enhancement. Utilizing the speedup obtainable by solving large domains on hundreds of cores, it should now be possible to solve problems over much longer time scales. In practice, ignition would require multiple pulses to ignite the mixture. Therefore, the next logical step would be to simulate several pulses (e.g. 5-10) in order to determine how previous streamer discharges affect subsequent discharges, as well as to model the accumulation of radical species and thermal energy. The end goal would be to capture the entire ignition event due to the discharge, starting from the initial plasma kernel formation until an exponential rise in combustion radicals and temperature is observed. The current chemistry mechanism was compiled assuming simulation times would be on the order of 100 ns. The mechanism will need to be improved to account for the long time scale (micro-millisecond) reactions involving the plasma species. In addition to the plasma reaction kinetics, a combustion mechanism such as

GRI 3.0 should be included. Combustion mechanism such as GRI 3.0 include pressure-dependent reactions which are currently not implemented.

The second is to investigate the interaction of an atmospheric pressure plasma jet with chemically reactive surfaces. For this work, it was assumed that the surface was inert while in reality the surfaces of interest such as biological tissue are complex systems that can play an active role in the reaction kinetics. Thus, detailed surface chemistry mechanisms for target materials of interest will have to be developed.

# Appendices

# Appendix A

# Chemistry Species Tables

All units are in molecules-meters-kelvins and seconds. Reaction rates are specified as Arrhenius rates with the form

$$AT^{B}exp(-C/T) \tag{A.0.1}$$

For reactions involving only heavy species (neutrals/ions/metastables) the rate is dependent on the heavy species temperature. For reactions involving electrons, the rate is dependent on the electron temperature.

For reactions where there is energy transfer between the electron and the heavy species due to an inelastic collision, the energy loss/gain is specified in the tables as $E_a$ on a per particle (electron volt) basis. A negative sign indicates a loss of energy from the electron and a gain in energy for the heavy species.

Finally, the electronically excited states of the molecules are often modeled as separate species with their own separate reaction rate coefficient. A metastable or long lived electronically excited state of a species is denoted with the species name and the uppercase symbol m (e.g. $Ar^m$). For other electronically excited states of species, the species symbols and the corresponding electronic excited states are listed in the table below.

| **Species Name** | **Electronic State** | **eV** |
|---|---|---|
| $O_2(a1)$ "Singlet Delta" | $a^1\Delta_g$ | 0.98 |
| $O_2(b1)$ "Singlet Sigma" | $b_1\sum_g^+$ | 1.63 |
| $O_2^*$ "Herzberg" | $O_2(c^1\sum_u^-)$,$O_2(C^3\delta_u)$, $O_2(A^3\sum_u^+)$ | 4.5 |
| $N_2(A)$ | $N_2(^A3\sum_u^+)$ | 6.17 |
| $N_2(a1)$ | $N_2(a^1\prod_g)$, $N_2(a'^1\sum_u^-)$, $N_2(W^1\Delta_u)$ | 8.4, 8.55, 8.89 |
| $N_2(C)$ | $N_2(C^3\prod_u)$ | 11.03 |
| $O_2(electronic)$ | $-$ | 6.0, 8.4, 9.97 |
| $N_2(electronic)$ | $N_2(E^3\sum_g^+)$, $N_2(A''\sum_g^+)$, $N^2(\|bco\|^3\prod_u)\|b'c'\|\sum_u^+$ | 11.88, 12.25, 13.0 |

Table A.1: Hydrogen-Oxygen List of Species

# Appendix B

# $O_2$-$H_2$ Chemistry

| Rxn | Reaction | A | B | C | $E_a$ | ref |
|---|---|---|---|---|---|---|
| | **Electron Impact Excitation/Dissociative Excitation** | | | | | |
| G1 | E + O → O($^1$D)+ E | | BOLSIG+ | | 2 | [40] |
| G2 | E + $O_2$ → O + O($^1$D) + E | | BOLSIG+ | | 7.12 | [40] |
| G3 | E + $O_2$ → $O_2(a1)$ + E | | BOLSIG+ | | 0.98 | [40] |
| G4 | E + $O_2$ → $O_2(b1)$ + E | | BOLSIG + | | 1.63 | [40] |
| G5 | E + $O_2$ → E + $O_2$ (rot.) | | BOLSIG + | | 0.02 | [40] |
| G6 | E + $O_2$ → E + $O_2$ (vib.) | | BOLSIG + | | 0.19 | [40] |
| G7 | E + $O_2$ → E + $O_2$ (elec.)(Herzberg) | | BOLSIG+ | | 4.5 | [40] |
| G8 | E + $O_2$ → E + $O_2$ (elec.) (other) | | BOLSIG+ | | 1 | [40] |
| G9 | E + $H_2$ → E + $H_2$ (rot.) | | BOLSIG+ | | 1 | [40] |
| G10 | E + $H_2$ → E + $H_2$ (vib.) | | BOLSIG+ | | 1 | [40] |
| G11 | E + $H_2$ → E + $H_2$ (elec.) | | BOLSIG+ | | 1 | [40] |
| G12 | E + $O_2(a1)$ → O + O($^1$D) + E | | BOLSIG+ | | 6.34 | [40] |
| G13 | E + $O_2(a1)$ → $O_2(b1)$ + E | | BOLSIG+ | | 0.64 | [40] |
| G14 | E + $O_2(b1)$ → O + O($^1$D) + E | 1.80E-13 | 0 | 2.13E+05 | 5.44 | [38] |
| | **Metastable Quenching** | | | | | |
| G15 | $2O_2(a1)$ → $O_2(b1)$ + $O_2$ | 6.99E-35 | 3.8 | -700 | -0.33 | [43] |
| G16 | $O_2(a1)$ + $O_2$ → $O_2$ + $O_2$ | 1.69E-24 | 0 | 0 | -0.98 | [102] |
| G17 | $O_2(a1)$ + $H_2$ → $O_2$ + $H_2$ | 4.48E-24 | 0 | 0 | -0.98 | [102] |
| G18 | $O_2(a1)$ + O → $O_2$ + O | 6.97E-22 | 0 | 0 | -0.98 | [102] |
| G19 | $O_2(a1)$ + H → $O_2$ + H | 6.97E-22 | 0 | 0 | -0.98 | [102] |
| G20 | $O_2(b1)$ + $O_2$ → $O_2(a1)$ + $O_2$ | 4.58E-23 | 0 | 0 | -0.65 | [102] |
| G21 | $O_2(b1)$ + $H_2$ → $O_2(a1)$ + $H_2$ | 8.17E-19 | 0 | 0 | -0.65 | [102] |
| G22 | $O_2(b1)$ + O → O2($a1$) + O | 7.97E-20 | 0 | 0 | -0.65 | [102] |
| G23 | $O_2(b1)$ + H → O2($a1$) + H | 7.97E-20 | 0 | 0 | -0.65 | [102] |
| G24 | O($^1$D) + $O_2$ → O + $O_2(a1)$ | 6.31E-18 | 0 | -67 | -1.02 | [102] |
| G25 | O($^1$D) + $O_2$ → O + $O_2(b1)$ | 2.56E-17 | 0 | -67 | -0.37 | [102] |
| G26 | O($^1$D) + $O_2(a1)$ → O + $O_2(b1)$ | 4.98E-17 | 0 | 0 | -1.35 | [102] |
| G27 | O($^1$D) + $H_2$ → O + $H_2$ | 5.48E-18 | 0 | 0 | -2 | [102] |
| G28 | O($^1$D) + O → O + O | 3.19E-17 | 0 | -67 | -2 | [102] |
| G29 | O($^1$D) + H → O + H | 3.19E-17 | 0 | -67 | -2 | [102] |
| G30 | O($^1$D) + $O_2$ → O + $O_2$ | 3.19E-17 | 0 | -67 | -2 | [102] |

| | | | | | | |
|---|---|---|---|---|---|---|
| G31 | $O_2(b1) + O_2 \rightarrow 2\ O_2$ | 1.00E-24 | 0 | 0 | -1.63 | [43] |
| G32 | $O_2(b1) + O \rightarrow O_2 + O$ | 8.00E-20 | 0 | 0 | -1.63 | [43] |
| | **Metastable De-Excitation** | | | | | |
| G33 | $E + O_2(a1) \rightarrow O_2 + E$ | 5.60E-15 | 0 | 2.55E+04 | -0.98 | [38] |
| G34 | $E + O_2(b1) \rightarrow O_2 + E$ | 5.60E-15 | 0 | 2.55E+04 | -1.63 | [38] |
| G35 | $E + O(^1D) \rightarrow O + E$ | 8.00E-15 | 0 | 0 | -2 | [37] |
| | **Electron Impact Dissociation** | | | | | |
| G36 | $E + O_2 \rightarrow O + O + E$ | | BOLSIG+ | | 5.12 | [40] |
| G37 | $E + H_2 \rightarrow E + 2H$ (combined) | | BOLSIG+ | | 1 | [40] |
| G38 | $E + O_2(a1) \rightarrow 2O + E$ | 4.20E-15 | 0 | 5.34E+04 | 4.14 | [38] |
| G39 | $E + O_2(b1) \rightarrow 2O + E$ | 7.10E-15 | 0 | 9.98E+04 | 3.44 | [38] |
| | **Electron Impact Ionization/Dissociative Ionization** | | | | | |
| G40 | $E + O_2 \rightarrow O2^+ + 2E$ | | BOLSIG+ | | 12.06 | [40] |
| G41 | $E + O \rightarrow O^+ + 2E$ | | BOLSIG+ | | 13.61 | [40] |
| G42 | $E + H_2 \rightarrow H_2^+ + 2E$ | | BOLSIG+ | | 15.4 | [40] |
| G43 | $E + H \rightarrow 2E + H^+$ | | BOLSIG+ | | 13.6 | [40]] |
| G44 | $E + O_2 \rightarrow O + O^+ + 2E$ | | BOLSIG+ | | 19.5 | [40] |
| G45 | $E + O_2 \rightarrow O^+ + O^- + E$ | 7.10E-17 | 0.5 | 1.97E+05 | 17.81 | [37] |
| G46 | $E + O(^1D) \rightarrow O^+ + 2E$ | 1.95E-17 | 0.6 | 1.40E+05 | 11.61 | [70] |
| G47 | $E + O_2(a1) \rightarrow O_2^+ + 2E$ | 9.00E-16 | 2 | 1.35E+05 | 11.08 | [38] |
| G48 | $E + O_2(b1) \rightarrow O_2^+ + 2E$ | 9.00E-16 | 0 | 1.46E+05 | 10.43 | [38] |
| G49 | $E + O_2(b1) \rightarrow O^+ + O + 2E$ | 5.30E-16 | 0.9 | 2.32E+05 | 17.1 | [38] |
| | **Electron Attachment** | | | | | |
| G50 | $E + O_2 \rightarrow O + O^-$ | | BOLSIG+ | | 4.2 | [40] |
| G51 | $E + O_2(a1) \rightarrow O + O^-$ | | BOLSIG+ | | 3.22 | [40] |
| G52 | $E + O_2(b1) \rightarrow O + O^-$ | | BOLSIG+ | | 2.57 | [40] |
| G53 | $E + O_2 + M \rightarrow O_2^- + M$ | | BOLSIG+ | | -0.43 | [40] |
| G54 | $E + O + O_2 \rightarrow O^- + O_2$ | 1.00E-43 | 0 | 0 | -0.92 | [37] |
| G55 | $E + O + O_2 \rightarrow O + O_2^-$ | 1.00E-43 | 0 | 0 | -0.43 | [37] |
| | **Electron-Ion** | | | | | |
| G56 | $E + O_2^+ \rightarrow 2O$ | | BOLSIG+ | | -6.91 | [40] |
| G57 | $E + O_4^+ \rightarrow 2O_2$ | | BOLSIG + | | -12.07 | [40] |
| G58 | $E + O_2^+ \rightarrow O(^1D) + O$ | 3.65E-12 | -0.7 | 0 | -10.06 | [37] |
| G59 | $E + O^- \rightarrow O + 2E$ | 2.10E-16 | 0.5 | 3.94E+04 | 0.92 | [70] |
| | **Ion-Neutral** | | | | | |
| G60 | $O^- + O \rightarrow O_2 + E$ | 1.40E-16 | 0 | 0 | -4.2 | [70] |
| G61 | $_2^- + O \rightarrow O^- + O_2$ | 5.73E-15 | -0.5 | 0 | -0.49 | [37] |
| G62 | $O^+ + O_2 \rightarrow O_2^+ + O$ | 2.10E-17 | 0 | 0 | -1.55 | [70] |
| G63 | $O_2^+ + O_2 + M \rightarrow O_2^+ + M$ | 2.03E-34 | -3.2 | 0 | 0.01 | [45] |
| | **Ion-Metastable** | | | | | |

| | | | | | | |
|---|---|---|---|---|---|---|
| G64 | $O_2(a1) + O^- \rightarrow O_2^- + O$ | 1.91E-16 | -0.5 | 0 | -0.48 | [37] |
| G65 | $O_2(a1) + O_2^- \rightarrow 2O_2 + E$ | 4.68E-16 | -0.5 | 0 | -0.55 | [37] |
| G66 | $O(^1D) + O2^+ \rightarrow O_2(a1) + O$ | 1.73E-17 | -0.5 | 0 | -13.08 | [37] |
| | **Ion-Ion** | | | | | |
| G67 | $O^- + O^+ \rightarrow O + O$ | 4.68E-12 | -0.5 | 0 | -12.69 | [37] |
| G68 | $O^- + O^+ \rightarrow O + O(^1D)$ | 8.49E-15 | -0.5 | 0 | -10.69 | [37] |
| G69 | $O^- + O_2^+ \rightarrow O + O_2$ | 3.46E-12 | -0.5 | 0 | -10.61 | [45] |
| G70 | $O_2^- + O_2^+ + M \leftrightarrow 2O_2 + M$ | 3.12E-31 | -2.5 | 0 | -11.64 | [45] |
| G71 | $O_2^- + O_4^+ \leftrightarrow 3O_2$ | 1.00E-13 | 0 | 0 | -11.64 | [45] |
| G72 | $O_2^- + O_4^+ + M \leftrightarrow 3O_2 + M$ | 3.12E-31 | -2.5 | 0 | -11.64 | [45] |
| G73 | $O_2^- + O^+ \rightarrow O_2 + O$ | 3.46E-12 | -0.5 | 0 | -13.18 | [37] |
| | **Neutral Combustion Reactions** | | | | | |
| G74 | $2O + M \leftrightarrow O_2 + M$ | 3.31E-43 | -1 | 0 | - | [36] |
| G75 | $O + H + M \leftrightarrow OH + M$ | 1.38E-42 | -1 | 0 | - | [36] |
| G76 | $O + H_2 \leftrightarrow OH + H$ | 6.43E-26 | 2.7 | 3.14E+03 | - | [36] |
| G77 | $O + OH \leftrightarrow O_2 + H$ | 4.40E-14 | -0.6707 | 8.56E+03 | - | [36] |
| G78 | $2H + M \leftrightarrow H_2 + M$ | 2.76E-42 | -1 | 0 | - | [36] |
| G79 | $H_2 + 2H \leftrightarrow 2H_2$ | 2.48E-43 | -0.6 | 0 | - | [36] |
| | **Metastable Combustion Reactions** | | | | | |
| G80 | $O_2(a1) + M \rightarrow 2O + M$ | 8.97E-12 | -1 | 4.80E+04 | - | [102] |
| G81 | $O_2(b1) + M \rightarrow 2O + M$ | 8.97E-12 | -1 | 4.04E+04 | - | [102] |
| G82 | $H_2 + O(^1D) \rightarrow OH + H$ | 1.04E-16 | 0 | 0 | - | [102] |
| G83 | $O_2(a1) + H \rightarrow OH + O$ | 1.83E-16 | 0 | 3.19E+03 | - | [102] |
| G84 | $OH + O \rightarrow O_2(a1) + H$ | 9.63E-18 | 0 | 6.22E+03 | - | [102] |
| G85 | $O_2(b1) + H \rightarrow OH + O$ | 1.83E-16 | 0 | 1.62E+03 | - | [102] |
| G86 | $H_2 + O_2(a1) \rightarrow 2OH$ | 2.82E-15 | 0 | 1.79E+04 | - | [102] |
| G87 | $H_2 + O_2(b1) \rightarrow 2OH$ | 2.82E-15 | 0 | 1.47E+04 | - | [102] |

# Appendix C

# Argon Chemistry

| **Rxn** | **Reaction** | **A** | **B** | **C** | $E_a$ | **ref** |
|---|---|---|---|---|---|---|
| G1 | $E + Ar \rightarrow E + Ar^m$ | 1.0E-14 | 0.1 | 1.3856E+05 | 11.56 | [27] |
| G2 | $E + Ar \rightarrow 2E + Ar^+$ | | BOLSIG+ | | 15.8 | [40] |
| G3 | $E + Ar^m \rightarrow 2E + Ar^+$ | | BOLSIG+ | | 4.43 | [40] |
| G4 | $E + Ar^m \rightarrow E + Ar$ | | BOLSIG + | | -11.5 | [40] |
| G5 | $2Ar^m \rightarrow E + Ar + Ar^+$ | 5.0E-16 | 0.0 | 0.0 | -7.2 | [27] |
| G6 | $E + Ar_2^m \rightarrow 2E + Ar_2^+$ | 1.29E-16 | 0.7 | 0.42456e5 | 3.66 | [27] |
| G7 | $E + Ar_2^m \rightarrow E + 2Ar$ | 1.0E-13 | 0.0 | 0.0 | -10.9 | [27] |
| G8 | $Ar^m + 2Ar \rightarrow Ar_2^m + Ar$ | 1.14E-44 | 0.0 | 0.0 | -0.6 | [27] |
| G9 | $Ar^+ + 2Ar \rightarrow Ar_2^+ + Ar$ | 2.5E-43 | 0.0 | 0.0 | -1.3 | [27] |
| G10 | $Ar_2^m \rightarrow 2Ar$ | 6.0E+7 | 0.0 | 0.0 | -10.9 | [27] |
| G11 | $2Ar_2^m \rightarrow E + Ar_2^+ + 2Ar$ | 5.0E-16 | 0.0 | 0.0 | -7.3 | [27] |
| G12 | $E + Ar^+ \rightarrow Ar^m$ | 4.3E-17 | -0.5 | 0.0 | -4.3 | [27] |
| G13 | $2E + Ar^+ \rightarrow E + Ar^m$ | 9.75E-15 | -4.5 | 0.0 | -4.3 | [27] |
| G14 | $E + Ar_2^+ \rightarrow Ar^m + Ar$ | 2.59E-11 | -0.66 | 0.0 | -3.0 | [27] |

# Appendix D

# Helium-Air Chemistry

| Rxn | Reaction | A | B | C | $E_a$ | ref |
|---|---|---|---|---|---|---|
| | **Helium Chemistry** | | | | | |
| G1 | $E + He \rightarrow 2E + He^+$ | 2.58E-18 | 0.68 | 285409 | 24.6 | [117] |
| G2 | $E + He \rightarrow E + He^m$ | 2.31E-16 | 0.31 | 229700 | 19.8 | [117] |
| G3 | $E + He^m \rightarrow 2E + He^+$ | 4.66E-16 | 0.6 | 55460 | 4.78 | [117] |
| G4 | $2He^m \rightarrow E + He + He^+$ | 4.50E-16 | 0 | 0 | -15 | [117] |
| G5 | $E + He^m \rightarrow E + He$ | 1.10E-11 | 0.31 | 0 | -19.8 | [117] |
| G6 | $E + He_2^m \rightarrow He_2^+ + 2E$ | 1.27E-18 | 0.71 | 39450 | 3.4 | [117] |
| G7 | $E + He_2^+ \rightarrow He^m + He$ | 5.39E-13 | -0.5 | 0 | 0 | [117] |
| G8 | $He^m + 2He \rightarrow He_2^m + He$ | 1.30E-45 | 0 | 0 | 0 | [117] |
| G9 | $He^+ + 2He \rightarrow He_2^+ + He$ | 1.00E-43 | 0 | 0 | 0 | [117] |
| | **Air Chemistry** | | | | | |
| G10 | $E + N_2 \rightarrow 2E + N_2^+$ | | BOLSIG+ | | 15.6 | [40] |
| G11 | $E + O_2 \rightarrow 2E + O_2^+$ | | BOLSIG+ | | 12.07 | [40] |
| G12 | $E + O_2 \rightarrow E + 2O$ | | BOLSIG+ | | 5.58 | [40] |
| G13 | $E + O_2 \rightarrow E + O + O(^1D)$ | | BOLSIG+ | | 8.4 | [40] |
| G14 | $E + O_2 \rightarrow O + O^-$ | | BOLSIG+ | | 3.6 | [40] |
| G15 | $E + N_2 \rightarrow E + N_2(rot.)$ | | BOLSIG+ | | 0.29 | [40] |
| G16 | $E + N_2 \rightarrow E + N_2(vsum)$ | | BOLSIG+ | | 1 | [40] |
| G17 | $E + N_2 \rightarrow E + N_2(elec.)$ | | BOLSIG+ | | 1 | [40] |
| G18 | $E + N_2 \rightarrow E + N_2(A)$ | | BOLSIG+ | | 6.17 | [40] |
| G19 | $E + O_2 \rightarrow E + O_2(rot.)$ | | BOLSIG+ | | 0.02 | [40] |
| G20 | $E + O_2 \rightarrow E + O_2(vsum)$ | | BOLSIG+ | | 0.193 | [40] |
| G21 | $E + O_2 \rightarrow E + O_2(elec.)$ | | BOLSIG+ | | 1 | [40] |
| G22 | $E + O_2 \rightarrow E + O_2(a1)$ | | BOLSIG+ | | 0.98 | [40] |
| G23 | $N_2^+ + N_2 + M \rightarrow N_4^+ + M$ | 5.00E-41 | 0 | 0 | 0 | [45] |
| G24 | $N_4^+ + O_2 \rightarrow O_2^+ + 2N_2$ | 2.50E-16 | 0 | 0 | -3.51 | [45] |
| G25 | $N_2^+ + O_2 \rightarrow O_2^+ + N_2$ | 1.04E-15 | -0.5 | 0 | -3.51 | [45] |
| G26 | $O_2^+ + 2N_2 \rightarrow O_2{+}N_2 + N_2$ | 8.10E-38 | -2 | 0 | 0 | [45] |
| G27 | $O_2{+}N_2 + N_2 \rightarrow O_2^+ + 2N_2$ | 14.8 | -5.3 | 2357 | 0 | [45] |
| G28 | $O_2{+}N_2 + O_2 \rightarrow O_4^+ + N_2$ | 1.00E-15 | 0 | 0 | 0 | [45] |
| G29 | $O_2^+ + O_2 + M \rightarrow O_4^+ + M$ | 2.03E-34 | -3.2 | 0 | 0 | [45] |

| | | | | | | |
|---|---|---|---|---|---|---|
| G30 | $E + O_4^+ \rightarrow 2O_2$ | 2.42E-11 | -0.5 | 0 | -12.07 | [45] |
| G31 | $E + O_2^+ \rightarrow 2O$ | 6.00E-11 | -1 | 0 | -6.91 | [45] |
| G32 | $E + 2O_2 \rightarrow O_2^- + O_2$ | 6.00E-39 | -1 | 0 | -0.43 | [45] |
| G33 | $O_2^- + O_4^+ \rightarrow 3O_2$ | 1.00E-13 | 0 | 0 | -11.64 | [45] |
| G34 | $O_2^- + O_4^+ + M \rightarrow 3O_2 + M$ | 3.12E-31 | -2.5 | 0 | -11.64 | [45] |
| G35 | $O_2^- + O_2^+ + M \rightarrow 2O_2 + M$ | 3.12E-31 | -2.5 | 0 | -11.64 | [45] |
| G36 | $O^- + O_2^+ \rightarrow O + O_2$ | 3.46E-12 | -0.5 | 0 | -10.61 | [45] |
| | **Helium-Nitrogen Interactions** | | | | | |
| G37 | $He^m + N_2 \rightarrow E + N_2^+ + He$ | 7.00E-17 | 0 | 0 | 0 | [117] |
| G38 | $He_2^m + N_2 \rightarrow E + N_2^+ + 2He$ | 7.00E-17 | 0 | 0 | 0 | [117] |
| G39 | $He^+ + N_2 \rightarrow N_2^+ + He$ | 5.00E-16 | 0 | 0 | 0 | [117] |
| G40 | $He_2^+ + N_2 \rightarrow N_2^+ + 2He$ | 5.00E-16 | 0 | 0 | 0 | [117] |

# Appendix E

# Methane-Air Chemistry

| Rxn | Reaction | A | B | C | $E_a$ | ref |
|---|---|---|---|---|---|---|
| G1 | $E + N_2 \rightarrow E + N_2(rot.)$ | | BOLSIG+ | | 0.02 | [42] |
| G2 | $E + N_2 \rightarrow E + N_2(vib.)$ | | BOLSIG+ | | 1.0 | [42] |
| G3 | $E + N_2 \rightarrow E + N_2(A)$ | | BOLSIG+ | | 6.17 | [42] |
| G4 | $E + N_2 \rightarrow E + N_2(B)$ | | BOLSIG+ | | 7.35 | [42] |
| G5 | $E + N_2 \rightarrow E + N_2(B)$ | | BOLSIG+ | | 7.36 | [42] |
| G6 | $E + N_2 \rightarrow E + N_2(B)$ | | BOLSIG+ | | 8.16 | [42] |
| G7 | $E + N_2 \rightarrow E + N_2(a1)$ | | BOLSIG+ | | 8.4 | [42] |
| G8 | $E + N_2 \rightarrow E + N_2(a1)$ | | BOLSIG+ | | 8.55 | [42] |
| G9 | $E + N_2 \rightarrow E + N_2(a1)$ | | BOLSIG+ | | 8.89 | [42] |
| G10 | $E + N_2 \rightarrow E + N_2(C)$ | | BOLSIG+ | | 11.03 | [42] |
| G11 | $E + N_2 \rightarrow E + N_2(elec.)$ | | BOLSIG+ | | 11.88 | [42] |
| G12 | $E + N_2 \rightarrow E + N_2(elec.)$ | | BOLSIG+ | | 12.25 | [42] |
| G13 | $E + N_2 \rightarrow E + N_2(elec.)$ | | BOLSIG+ | | 13.0 | [42] |
| G14 | $E + N_2 \rightarrow 2E + N_2^+$ | | BOLSIG+ | | 15.6 | [42] |
| G15 | $E + O_2 \rightarrow E + O_2(rot.)$ | | BOLSIG+ | | 0.02 | [42] |
| G16 | $E + O_2 \rightarrow E + O_2$ | | BOLSIG+ | | 0.0193 | [42] |
| G17 | $E + O_2 \rightarrow E + O_2(a1)$ | | BOLSIG+ | | 0.98 | [42] |
| G18 | $E + O_2 \rightarrow E + O_2(b1)$ | | BOLSIG+ | | 1.63 | [42] |
| G19 | $E + O_2 \rightarrow E + O_2^*$ | | BOLSIG+ | | 4.5 | [42] |
| G20 | $E + O_2 \rightarrow E + O_2(elec.)$ | | BOLSIG+ | | 6.0 | [42] |
| G21 | $E + O_2 \rightarrow E + O_2(elec.)$ | | BOLSIG+ | | 8.4 | [42] |
| G22 | $E + O_2 \rightarrow E + O_2(elec.)$ | | BOLSIG+ | | 9.97 | [42] |
| G23 | $E + O_2 \rightarrow E + 2O$ | | BOLSIG+ | | 5.58 | [42] |
| G24 | $E + O_2 \rightarrow E + 2O(O + O(^1D))$ | | BOLSIG+ | | 8.4 | [42] |
| G25 | $E + O_2 \rightarrow 2E + O_2^+$ | | BOLSIG+ | | 12.07 | [42] |
| G26 | $E + O \rightarrow E + O$ | | BOLSIG+ | | 6.34 | [42] |
| G27 | $E + CH_4 \rightarrow E + CH_4(vib.)$ | | BOLSIG+ | | 0.36 | [22] |
| G28 | $E + CH_4 \rightarrow E + CH_4$ | | BOLSIG+ | | 0.162 | [22] |
| G29 | $E + CH_4 \rightarrow 2E + CH_4^+$ | | BOLSIG+ | | 12.6 | [22] |
| G30 | $E + CH_4 \rightarrow 2E + CH_3^+ + H$ | | BOLSIG+ | | 14.3 | [22] |
| G31 | $E + CH_4 \rightarrow E + CH_3 + H$ | | BOLSIG+ | | 9.0 | [22] |
| G32 | $E + CH_4 \rightarrow E + CH_3 + H$ | | BOLSIG+ | | 10.0 | [22] |
| G33 | $E + CH_4 \rightarrow E + CH_3 + H$ | | BOLSIG+ | | 11.0 | [22] |

| | | | | | | |
|---|---|---|---|---|---|---|
| G34 | $E + CH_4 \rightarrow E + CH_3 + H$ | BOLSIG+ | | | 12.0 | [22] |
| G35 | $E + O_2^+ \rightarrow 2O$ | BOLSIG+ | | | -0.691 | [42] |
| G36 | $E + O_4^+ \rightarrow 2O_2$ | BOLSIG+ | | | -12.07 | [42] |
| G37 | $E + O_2 \rightarrow O^- + O$ | BOLSIG+ | | | 4.66 | [42] |
| G38 | $E + CH_4 \rightarrow H^- + CH_3$ | BOLSIG+ | | | 9.0 | [42] |
| G39 | $E + CH_4 \rightarrow CH_2^- + CH_2$ | BOLSIG+ | | | 10.8 | [42] |
| G40 | $E + O_2(a1) \rightarrow E + O_2(b1)$ | BOLSIG+ | | | 0.65 | [42] |
| G41 | $E + O_2(a1) \rightarrow E + 2O$ | BOLSIG+ | | | 6.34 | [42] |
| G42 | $E + O_2(a1) \rightarrow O^- + O$ | BOLSIG+ | | | 3.9 | [42] |
| G43 | $E + O_2(b1) \rightarrow O^- + O$ | BOLSIG+ | | | 3.7 | [42] |
| G44 | $N_2^+ + N_2 + M \rightarrow N_4^+ + M$ | 5.0-41 | 0 | 0 | 1.0 | [77] |
| G45 | $N_4^+ + O_2 \rightarrow O_2^+ + 2N_2$ | 2.5-16 | 0 | 0 | -3.51 | [77] |
| G46 | $N_2^+ + O_2 \rightarrow O_2^+ + N_2$ | 1.04-15 | -0.5 | 0 | -3.51 | [77] |
| G47 | $O_2^+ + 2N_2 \rightarrow (O_2 + N_2) + N_2$ | 8.1-38 | -2.0 | 0.0 | – | [77] |
| G48 | $(O_2 + N_2) + N_2 \rightarrow O_2^+ + 2N_2$ | 14.8 | -5.3 | 2357 | – | [77] |
| G49 | $O_2 + N_2 + O_2 \rightarrow O_4^+ + N_2$ | 1.0E-15 | 0.0 | 0.0 | – | [77] |
| G50 | $O_2^+ + O_2 + M \rightarrow O_4^+ + M$ | 2.03E-34 | -3.2 | 0.0 | – | [77] |
| G51 | $E + 2O_2 \rightarrow O_2^- + O_2$ | 6.0E-39 | -1.0 | 0.0 | -0.43 | [77] |
| G52 | $O_2^- + O_4^+ \rightarrow 3O_2$ | 1.0E-13 | 0.0 | 0.0 | -11.64 | [77] |
| G53 | $O_2^- + O_4^+ + M \rightarrow 3O_2 + M$ | 3.12E-31 | -2.5 | 0.0 | -11.64 | [77] |
| G54 | $O_2^- + O_2^+ + M \rightarrow 2O_2 + M$ | 3.12E-31 | -2.5 | 0.0 | -11.64 | [77] |
| G55 | $O^- + O_2^+ + M \rightarrow O + O_2$ | 3.464E-12 | -0.5 | 0.0 | -10.61 | [77] |
| G56 | $N_2(A) + O_2 \rightarrow N_2 + 2O$ | 1.7E-18 | 0.0 | 0.0 | -1.05 | [8] |
| G57 | $N_2(A) + O_2 \rightarrow N_2 + O_2(b1)$ | 7.5E-19 | 0.0 | 0.0 | -4.54 | [8] |
| G58 | $2N_2(A) \rightarrow N_2 + N_2(B)$ | 7.7E-17 | 0.0 | 0.0 | -4.99 | [8] |
| G59 | $2N_2(A) \rightarrow N_2 + N_2(C)$ | 1.6E-16 | 0.0 | 0.0 | -1.31 | [8] |
| G60 | $N_2(A) + N_2 \rightarrow N_2 + N_2(B)$ | 1.0E-16 | 0.0 | 1500 | -0.32 | [8] |
| G61 | $N_2(A) + O \rightarrow N_2 + O$ | 3.0E-17 | 0.0 | 0.0 | -6.17 | [8] |
| G62 | $N_2(B) + O_2 \rightarrow N_2 + 2O$ | 3.0E-16 | 0.0 | 0.0 | -2.23 | [8] |
| G63 | $N_2(B) + N_2 \rightarrow N_2(A) + N_2$ | 1.0E-17 | 0.0 | 0.0 | -1.18 | [8] |
| G64 | $N_2(a1) + O_2 \rightarrow N_2 + 2O$ | 2.8E-17 | 0.0 | 0.0 | -3.28 | [8] |
| G65 | $N_2(a1) + N_2 \rightarrow 2N_2$ | 2.0E-19 | 0.0 | 0.0 | -8.4 | [8] |
| G66 | $N_2(C) + O_2 \rightarrow N_2 + 2O$ | 3.0E-16 | 0.0 | 0.0 | -5.91 | [8] |
| G67 | $N_2(C) + N_2 \rightarrow N_2(a1) + N_2$ | 1.0E-17 | 0.0 | 0.0 | -2.63 | [8] |
| G68 | $N_2(C) \rightarrow N_2(B) + h\nu\ (photon)$ | 3.0 | 0.0 | 0.0 | – | [8] |
| G69 | $N_2(A) + CH_4 \rightarrow N_2 + CH_4$ | 3.0E-21 | 0.0 | 0.0 | -6.17 | [8] |
| G70 | $N_2(B) + CH_4 \rightarrow N_2(A) + CH_4$ | 2.85E-16 | 0.0 | 0.0 | -1.08 | [8] |
| G71 | $N_2(B) + CH_4 \rightarrow N_2 + CH_3 + H$ | 1.5E-17 | 0.0 | 0.0 | 3.15 | [8] |
| G72 | $N_2(a1) + CH_4 \rightarrow N_2 + CH_3 + H$ | 3.0E-16 | 0.0 | 0.0 | 2.1 | [8] |
| G73 | $N_2(C) + CH_4 \rightarrow N_2 + CH_3 + H$ | 3.0E-16 | 0.0 | 0.0 | -0.8 | [8] |
| G74 | $O_2^* + CH_4 \rightarrow O_2 + CH_3 + H$ | 3.0E-21 | 0.0 | 0.0 | – | [8] |
| G75 | $O_2^* + O_2 \rightarrow O_2(a1) + O_2$ | 1.86E-19 | 0.0 | 0.0 | -3.52 | [8] |
| G76 | $O_2^* + O_2 \rightarrow O_2(b1) + O_2$ | 8.1E-20 | 0.0 | 0.0 | -2.87 | [8] |
| G77 | $O_2^* + O_2 \rightarrow 2O_2$ | 2.3E-20 | 0.0 | 0.0 | -4.5 | [8] |

| | | | | | | |
|---|---|---|---|---|---|---|
| G78 | $O_2^* + \mathrm{O} \rightarrow O_2 + \mathrm{O}$ | 5.0E-18 | 0.0 | 0.0 | -4.5 | [8] |
| G79 | $O_2^* + \mathrm{O} \rightarrow O_2(a1) + \mathrm{O}$ | 2.7E-18 | 0.0 | 0.0 | -3.52 | [8] |
| G80 | $O_2^* + \mathrm{O} \rightarrow O_2(b1) + \mathrm{O}$ | 1.35E-18 | 0.0 | 0.0 | -2.87 | [8] |
| G81 | $N_2^+ + CH_4 \rightarrow N_2 + CH_3^+ + \mathrm{H}$ | 1.3E-15 | 0.0 | 0.0 | – | [8] |
| G82 | $CH_4^+ + O_2 \rightarrow CH_4 + O_2^+ + \mathrm{H}$ | 5.0E-16 | 0.0 | 0.0 | – | [8] |
| G83 | $\mathrm{E} + CH_4^+ \rightarrow CH_3 + \mathrm{H}$ | 2.95E-12 | -0.5 | 0.0 | – | [8] |
| G84 | $\mathrm{E} + CH_4^+ \rightarrow CH_2 + 2\mathrm{H}$ | 2.95E-12 | -0.5 | 0.0 | – | [8] |
| G85 | $\mathrm{E} + CH_3^+ \rightarrow CH_2 + \mathrm{H}$ | 6.06E-12 | -0.5 | 0.0 | – | [8] |

# Bibliography


[1] Etatech advanced ignition system, www.etatech.us/technical-papers/eccos-advanced-ignition-system.ppt.

[2] University of southern california pulsed power research group, http://www.usc.edu/dept/ee/

[3] N.Y. Liu S. Celestin P. Segur A. Bourdon, N.P. Pasko and E. Marode. Efficient models for photoionization produced by non-thermal gas discharges in air based on radiative transfer and the helmholtz equations. *Plasma Sources Science and Technology*, 16:656–678, 2007.

[4] C. Montijn A. Luque, U. Ebert and W. Hundsdorfer. Photoionization in negative streamers: fast computationas and two propagation modes. *Applied Physics Letters*, 90:081501, 2007.

[5] C. Montijn A. Luque, U. Ebert and W. Hundsdorfer. Computational study of cold atmospheric pulsed helium plasma jet in air. *Applied Physics Letters*, 99:111501, February 2011.

[6] I.V. Adamovich, I. Choi, N. Jiang, J.H. Kim, S. Keshav, W.R. Lempert, E. Mintusov, M. Nishihara, M. Samimy, and M. Uddi. Plasma assisted ignition and high-speed flow control: non-thermal and thermal effects. *Plasma Sources Science and Technology*, 18:034018, 2009.

[7] I.V. Adamovich, W.R. Lempert, M. Nishihara, J.W. Rich, and Y.G. Utkin. Repetitively pulsed nonequilibrium plasmas for magnetohydrodynamic flow control and plasma-assisted combustion. *Journal of Propulsion and Power*, 24(6):1198, 2010.

[8] N.L. Aleksandrov, S.V. Kindysheva, E.N. Kukaev, SM Starikovskaia, and A.Y. Starikovskii. Simulation of the ignition of a methane-air mixture by a high-voltage nanosecond discharge. *Plasma physics reports*, 35(10):867–882, 2009.

[9] P.R. Amestoy, I.S. Duff, J.Y. LExcellent, and J. Koster. Multifrontal massively parallel solver (mumps version 4.3) users guide. *ENSEEIHT-IRIT, Toulouse, France*, 2003.

[10] S. Balay, J. Brown, K. Buschelman, V. Eijkhout, W. Gropp, D. Kaushik, M. Knepley, L.C. McInnes, B. Smith, and H. Zhang. Petsc users manual revision 3.3. 2012.

[11] D.L. Bayliss, J.L. Walsh, G. Shama, F. Iza, and M.G. Kong. Reduction and degradation of amyloid aggregates by a pulsed radio-frequency cold atmospheric plasma jet. *New Journal of Physics*, 11(11):115024, 2009.

[12] J. Blazek. *Computational fluid dynamics: principles and applications*. Elsevier Science, 2001.

[13] J. Blazek. *Computational fluid dynamics: principles and applications*, volume 2. Elsevier Science, 2005.

[14] G.P. Boeuf and L. Pitchford. *4th Intl. Workshop on Micro-plasmas*, April 3-6, 2011.

[15] A. Bourdon, V.P. Pasko, N.Y. Liu, S. Célestin, P. Ségur, and E. Marode. Efficient models for photoionization produced by non-thermal gas discharges in air based on radiative transfer and the helmholtz equations. *Plasma Sources Science and Technology*, 16(3):656, 2007.

[16] A. Bourig, V. Lago, J.P. Martin, K. Pliavaka, F. Pliavaka, S. Gorbatov, A. Chernukho, and V. Naumov. Generation of singlet oxygen in hv pulsed+ dc crossed discharge at atmospheric pressure for oxygen-enhanced combustion. *International Journal of Plasma Environmental Science and Technology*, 1(1):57–63, 2007.

[17] A. Bourig, D. Thévenin, J.P. Martin, G. Janiga, and K. Zähringer. Numerical modeling of h2-o2 flames involving electronically-excited species o2 (a1 [delta] g), o (1d) and oh (2 [sigma]+). *Proceedings of the Combustion Institute*, 32(2):3171–3179, 2009.

[18] D. Breden, K. Miki, and L.L. Raja. Computational study of cold atmospheric nanosecond pulsed helium plasma jet in air. *Applied Physics Letters*, 99(11):111501–111501, 2011.

[19] D Breden and L L Raja. Simulations of nanosecond pulsed plasmas in supersonic flows for combustion applications. *AIAA Journal*, 50(3):647–658, 2012.

[20] D. Breden and L.L. Raja. Simulations of nanosecond pulse plasmas in supersonic flows for combustion applications. *AIAA Journal*, 50(3), 2012.

[21] K. Miki D. Breden and L.L. Raja. Self-consistent two-dimensional modelling of cold atmospheric-pressure plasma jets/bullets. *Plasma Sources Science and Technology*, 21:034011 (13pp), 2012.

[22] D.K. Davies, L.E. Kline, and W.E. Bies. Measurements of swarm parameters and derived electron collision cross sections in methane. *Journal of Applied Physics*, 65(9):3311–3323, 1989.

[23] G.A. Dawson and W.P. Winn. A model for streamer propagation. *Zeitschrift für Physik*, 183(2):159–171, 1965.

[24] T. Deconinck, S. Mahadevan, and L.L. Raja. Simulation of direct-current surface plasma discharge phenomena in high-speed flow actuation. *Plasma Science, IEEE Transactions on*, 35(5):1301–1311, 2007.

[25] T. Deconinck, S. Mahadevan, and L.L. Raja. Computational simulation of coupled nonequilibrium discharge and compressible flow phenomena in a microplasma thruster. *Journal of Applied Physics*, 106(6):063305–063305, 2009.

[26] T. Deconinck, S. Mahadevan, and L.L. Raja. Discretization of the joule heating term for plasma discharge fluid models in unstructured meshes. *Journal of Computational Physics*, 228(12):4435–4443, 2009.

[27] T. Deconinck and L.L. Raja. Modeling of mode transition behavior in argon microhollow cathode discharges. *Plasma Processes and Polymers*, 6(5):335–346, 2009.

[28] S.K. Dhali and P.F. Williams. Numerical simulation of streamer propagation in nitrogen at atmospheric pressure. *Physical Review A*, 31(2):1219, 1985.

[29] S.K. Dhali and P.F. Williams. Two-dimensional studies of streamers in gases. *Journal of applied physics*, 62(12):4696–4707, 1987.

[30] H. Do, M.A. Cappelli, and M.G. Mungal. Plasma assisted cavity flame ignition in supersonic flows. *Combustion and Flame*, 157(9):1783–1794, 2010.

[31] H. Do, M.G. Mungal, and M.A. Cappelli. Jet flame ignition in a supersonic crossflow using a pulsed nonequilibrium plasma discharge. *Plasma Science, IEEE Transactions on*, 36(6):2918–2923, 2008.

[32] U. Ebert, C. Montijn, T.M.P. Briels, W. Hundsdorfer, B. Meulenbroek, A. Rocco, and E.M. Van Veldhuizen. The multiscale nature of streamers. *Plasma Sources Science and Technology*, 15(2):S118, 2006.

[33] P. Felsenthal and J.M. Proud. Nanosecond-pulse breakdown in gases. *Physical Review*, 139(6A):A1796, 1965.

[34] G.I. Font, C.L. Enloe, and T.E. McLaughlin. Plasma volumetric effects on the force production of a plasma actuator. *AIAA journal*, 48(9):1869–1874, 2010.

[35] I. Gallimberti. A computer model for streamer propagation. *Journal of Physics D: Applied Physics*, 5(12):2179, 1972.

[36] Michael Frenklach Nigel W. Moriarty Boris Eiteneer Mikhail Goldenberg C. Thomas Bowman Ronald K. Hanson Soonho Song William C. Gardiner Jr. Vitali V. Lissianski Gregory P. Smith, David M. Golden and Zhiwei Qin. Gri-mech 3.0, http://www.me.berkeley.edu/gri_mech.

[37] J.T. Gudmundsson. Global model of plasma chemistry in a low-pressure o2/f2 discharge. *Journal of Physics D: Applied Physics*, 35(4):328, 2002.

[38] J.T. Gudmundsson. Recombination and detachment in oxygen discharges: the role of metastable oxygen molecules. *Journal of Physics D: Applied Physics*, 37(15):2073, 2004.

[39] G.J.M. Hagelaar and G.M.W. Kroesen. Speeding up fluid models for gas discharges by implicit treatment of the electron energy source term. *Journal of Computational Physics*, 159:1–12, 2000.

[40] G.J.M. Hagelaar and L. C. Pitchford. Solving the boltzmann equation to obtain electron transport coefficients and rate coefficients for fluid models. *Plasma Sources Science and Technology*, 14:722, 2005.

[41] A. Haselbacher and J. Blazek. Accurate and efficient discretization of navier-stokes equations on mixed grids. *AIAA journal*, 38(11):2094–2102, 2000.

[42] A.A. Ionin, I.V. Kochetov, A.P. Napartovich, and N.N. Yuryshev. Physics and engineering of singlet delta oxygen production in low-temperature plasma. *Journal of Physics D: Applied Physics*, 40(2):R25, 2007.

[43] J.Y. Jeong, J. Park, I. Henins, S.E. Babayan, V.J. Tu, G.S. Selwyn, G. Ding, and R.F. Hicks. Reaction chemistry in the afterglow of an oxygen-helium, atmospheric-pressure plasma. *The Journal of Physical Chemistry A*, 104(34):8027–8032, 2000.

[44] E. Karakas, M. Koklu, and M. Laroussi. Correlation between helium mole fraction and plasma bullet propagation in low temperature plasma jets. *Journal of Physics D: Applied Physics*, 43:155202, 2010.

[45] I.A. Kossyi, A.Y. Kostinsky, A.A. Matveyev, and V.P. Silakov. Kinetic scheme of the non-equilibrium discharge in nitrogen-oxygen mixtures. *Plasma Sources Science and Technology*, 1(3):207, 1992.

[46] C.H. Kruger, C.O. Laux, L. Yu, D.M. Packan, L. Pierrot, et al. Nonequilibrium discharges in air and nitrogen plasmas at atmospheric pressure. *Pure and applied chemistry*, 74(3):337–347, 2002.

[47] Alejandro L., V. Ratushnaya, and U. Ebert. Positive and negative streamers in ambient air: modelling evolution and velocities. *Journal of*

*Physics D: Applied Physics*, 41(23):234005, 2008.

[48] M. Laroussi and T. Akan. Arc-free atmospheric pressure cold plasma jets: A review. *Plasma Processes and Polymers*, 4(9):777–788, 2007.

[49] M. Laroussi and X. Lu. Room-temperature atmospheric pressure plasma plume for biomedical applications. *Applied Physics Letters*, 87(11):113902–113902, 2005.

[50] S.B. Leonov and D.A. Yarantsev. Plasma-induced ignition and plasma-assisted combustion in high-speed flow. *Plasma Sources Science and Technology*, 16:132, 2007.

[51] X.S. Li and J.W. Demmel. Superlu_dist: A scalable distributed-memory sparse direct solver for unsymmetric linear systems. *ACM Transactions on Mathematical Software (TOMS)*, 29(2):110–140, 2003.

[52] M.A. Lieberman and A.J. Lichtenberg. Principles of plasma discharges and materials processing. 1994.

[53] A.V. Likhanskii, M.N. Shneider, S.O. Macheret, and R.B. Miles. Modeling of dielectric barrier discharge plasma actuators driven by repetitive nanosecond pulses. *Physics of plasmas*, 14:073501, 2007.

[54] M.S. Liou. A sequel to ausm: Ausm. *Journal of computational Physics*, 129(2):364–382, 1996.

[55] J. Little and M. Samimy. High-lift airfoil separation with dielectric barrier discharge plasma actuation. *AIAA journal*, 48(12):2884–2898, 2010.

[56] J. Little, K. Takashima, M. Nishihara, I. Adamovich, and M. Samimy. Separation control with nanosecond-pulse-driven dielectric barrier discharge plasma actuators. *AIAA Journal-American Institute of Aeronautics and Astronautics*, 50(2):350, 2012.

[57] L.B. Loeb and J.M. Meek. The mechanism of spark discharge in air at atmospheric pressure. i. *Journal of Applied Physics*, 11(6):438–447, 1940.

[58] L.B. Loeb and J.M. Meek. The mechanism of spark discharge in air at atmospheric pressure. ii. *Journal of Applied Physics*, 11(7):459–474, 1940.

[59] G. Lou, A. Bao, M. Nishihara, S. Keshav, Y.G. Utkin, J.W. Rich, W.R. Lempert, and I.V. Adamovich. Ignition of premixed hydrocarbon–air flows by repetitively pulsed, nanosecond pulse duration plasma. *Proceedings of the Combustion Institute*, 31(2):3327–3334, 2007.

[60] X.P. Lu and M. Laroussi. Dynamics of an atmospheric pressure plasma plume generated by submicrosecond voltage pulses. *Journal of applied physics*, 100:063302, 2006.

[61] A. Luque, U. Ebert, and W. Hundsdorfer. Interaction of streamer discharges in air and other oxygen-nitrogen mixtures. *Physical review letters*, 101(7):075005, 2008.

[62] A. Luque, U. Ebert, C. Montijn, and W. Hundsdorfer. Photoionization in negative streamers: Fast computations and two propagation modes. *Applied physics letters*, 90(8):081501–081501, 2007.

[63] S.O. Macheret, M.N. Shneider, and R.C. Murray. Ionization in strong electric fields and dynamics of nanosecond-pulse plasmas. *Physics of plasmas*, 13:023502, 2006.

[64] S. Mahadevan and L.L Raja. Electrode polarity effects in surface plasma discharges for supersonic flow control applications: A computational study. *AIAA Paper*, 256:2010, 2010.

[65] S. Mahadevan and L.L. Raja. Simulations of direct-current air glow discharge at pressures 1. *Journal of Applied Physics*, 107(9):093304–093304, 2010.

[66] S. Mahadevan and L.L. Raja. Simulations of direct-current air glow discharge at pressures 1 torr: Discharge model validation. *Journal of Computational Physics*, 107:093304, 2010.

[67] S. Mahadevan and L.L. Raja. Simulation of direct-current surface plasma discharges in air for supersonic flow control. *AIAA journal*, 50(2):325–337, 2012.

[68] E. Marode. The mechanism of spark breakdown in air at atmospheric pressure between a positive point and a plane. i. experimental: Nature of the streamer track. *Journal of Applied Physics*, 46(5):2005–2015, 1975.

[69] A.Kh. Mnatsakanyan M.B. Zheleznyak and S.V. Sizykh. Photoionization of nitrogen-oxygen mixtures by radiation of gas discharge teplofiz. *High Temp*, 20:833, 1982.

[70] E. Meeks, R.S. Larson, P. Ho, C. Apblett, S.M. Han, E. Edelberg, and E.S. Aydil. Modeling of sio2 deposition in high density plasma reactors and comparisons of model predictions with experimental measurements. *Journal of Vacuum Science & Technology A: Vacuum, Surfaces, and Films*, 16(2):544–563, 1998.

[71] N. Mericam-Bourdet, M. Laroussi, A. Begum, and E. Karakas. Experimental investigations of plasma bullets. *Journal of Physics D: Applied Physics*, 42:055207, 2009.

[72] M. Nagulapally, G.V. Candler, C.O. Laux, L. Yu, D. Packan, C.H. Kruger, R. Stark, and K.H. Schoenbach. Experiments and simulations of dc and pulsed discharges in air plasmas. *AIAA Paper*, 2417, 2000.

[73] G.V. Naidis. Simulation of streamer-induced pulsed discharges in atmospheric-pressure air. *The European Physical Journal Applied Physics*, 47(02), 2009.

[74] G.V. Naidis. Modelling of streamer propagation in atmospheric-pressure helium plasma jets. *Journal of Physics D: Applied Physics*, 43:402001, 2010.

[75] G.V. Naidis. Modelling of plasma bullet propagation along a helium jet in ambient air. *Journal of Physics D: Applied Physics*, 44:215203, 2011.

[76] E. Marode D. Bessieres P. Segur, A. Bourdon and J.H. Paillol. The use of an improved eddington approximation to facilitate the calculation of photoionization in streamer discharges. *Plasma Sources Sci. Technol.*, 15:648–660, 2006.

[77] S. Pancheshnyi, M. Nudnova, and A. Starikovskii. Development of a cathode-directed streamer discharge in air at different pressures: experiment and comparison with direct numerical simulation. *Physical Review E*, 71(1):016407, 2005.

[78] S. Pancheshnyi, P. Ségur, J. Capeillère, and A. Bourdon. Numerical simulation of filamentary discharges with parallel adaptive mesh refinement. *Journal of Computational Physics*, 227(13):6574–6590, 2008.

[79] S.V. Pancheshnyi and A.Y. Starikovskii. Two-dimensional numerical modelling of the cathode-directed streamer development in a long gap at high voltage. *Journal of Physics D: Applied Physics*, 36(21):2683, 2003.

[80] Suhas V. Patankar. *Numerical heat transfer and fluid flow.* Taylor & Francis Group, 1980.

[81] G. Pilla, D. Galley, D.A. Lacoste, F. Lacas, D. Veynante, and C.O. Laux. Stabilization of a turbulent premixed flame using a nanosecond repetitively pulsed plasma. *Plasma Science, IEEE Transactions on*, 34(6):2471–2477, 2006.

[82] G.L. Pilla, D.A. Lacoste, D. Veynante, and C.O. Laux. Stabilization of a swirled propane–air flame using a nanosecond repetitively pulsed plasma. *Plasma Science, IEEE Transactions on*, 36(4):940–941, 2008.

[83] R.J. Hoekstra P.L.G. Ventzek, T.J. Sommerer and M.J. Kushner. Two-dimensional hybrid model of inductively coupled plasma sources for etching. *Applied Physics Letters*, 63:5, 1993.

[84] H. Raether. The development of electron avalanche in a spark channel (from observations in a cloud chamber). *Zeitschrift fur Physik*, 112:464–472, 1939.

[85] H. Raether. *Electron avalanches and breakdown in gases.* Butterworths London, 1964.

[86] Y.P. Raizer and C. Braun. Gas discharge physics. *Applied Optics*, 31:2400–2401, 1992.

[87] D.V. Roupassov, A.A. Nikipelov, M.M. Nudnova, and A.Y. Starikovskii. Flow separation control by plasma actuator with nanosecond pulsed-periodic discharge. *AIAA Journal*, 47(1):168–185, 2009.

[88] K. Buschelman W. D. Gropp D. Kaushik M.G. Kneplery L.C. McInnes B.F. Smith S. Balay, J. Brown and H. Zhang. Petsc web page, 2012.

[89] Y. Saad. *Iterative methods for sparse linear systems*. Society for Industrial and Applied Mathematics, 2003.

[90] Y. Sakiyama, D.B. Graves, J. Jarrige, and M. Laroussi. Finite element analysis of ring-shaped emission profile in plasma bullet. *Applied Physics Letters*, 96(4):041501–041501, 2010.

[91] D.L. Scharfetter and H.K. Gummel. Ieee transactions on electron devices. *Journal of Computational Physics*, ED-16(1), 1969.

[92] P. Ségur, A. Bourdon, E. Marode, D. Bessieres, and J.H. Paillol. The use of an improved eddington approximation to facilitate the calculation of photoionization in streamer discharges. *Plasma Sources Science and Technology*, 15(4):648, 2006.

[93] A. Shashurin, M.N. Shneider, A. Dogariu, R.B. Miles, and M. Keidar. Temporal behavior of cold atmospheric plasma jet. *Applied Physics Letters*, 94(23):231504–231504, 2009.

[94] J. Shin and L.L. Raja. Dynamics of pulse phenomena in helium dielectric-barrier atmospheric-pressure glow discharges. *Journal of applied physics*, 94(12):7408–7415, 2003.

[95] T. Shiraishi and T. Urushihara. Fundamental analysis of combustion initiation characteristics of low temperature plasma ignition for internal combustion engine. *SAE International*, page 0660, 2011.

[96] T. Shiraishi, T. Urushihara, and M.A. Gundersen. A trial of ignition innovation of gasoline engine by nanosecond pulsed low temperature plasma ignition. *Journal of Physics D: Applied Physics*, 42(13):135208, 2009.

[97] R.S. Sigmond. The residual streamer channel: Return strokes and secondary streamers. *Journal of applied physics*, 56(5):1355–1370, 1984.

[98] D. Singleton, S.J. Pendleton, and M.A. Gundersen. The role of non-thermal transient plasma for enhanced flame ignition in c2h4–air. *Journal of Physics D: Applied Physics*, 44(2):022001, 2011.

[99] V.R. Soloviev and V.M. Krivtsov. Surface barrier discharge modelling for aerodynamic applications. *Journal of Physics D: Applied Physics*, 42:125208, 2009.

[100] G.D. Stancu, F. Kaddouri, D.A. Lacoste, and C.O. Laux. Investigations of rapid plasma chemistry generated by nanosecond discharges in air at atmospheric pressure using advanced optical diagnostics, 2009.

[101] A.M. Starik, B.I. Lukhovitskii, and N.S. Titova. Initiation of combustion of a ch 4-o 2 mixture in a supersonic flow with excitation of o 2 molecules by an electric discharge. *Combustion, Explosion, and Shock Waves*, 44(3):249–261, 2008.

[102] A.M. Starik and N.S. Titova. Kinetics of detonation initiation in the supersonic flow of the h2+ o2 (air) mixture in o2 molecule excitation by resonance laser radiation. *Kinetics and catalysis*, 44(1):28–39, 2003.

[103] A.M. Starik, N.S. Titova, L.V. Bezgin, V.I. Kopchenov, and V.V. Naumov. Control of combustion by generation of singlet oxygen molecules in electrical discharge. *Czechoslovak Journal of Physics*, 56:1357–1363, 2006.

[104] S.M. Starikovskaia. Plasma assisted ignition and combustion. *Journal of Physics D: Applied Physics*, 39:R265, 2006.

[105] A.Y. Starikovskii and N. Aleksandrov. Plasma-assisted ignition and combustion. *Progress in Energy and Combustion Science*, 2012.

[106] A.Y. Starikovskii, N.B. Anikin, I.N. Kosarev, E.I. Mintoussov, M.M. Nudnova, A.E. Rakitin, D.V. Roupassov, S.M. Starikovskaia, and V.P. Zhukov. Nanosecond-pulsed discharges for plasma-assisted combustion and aerodynamics. *Journal of Propulsion and Power*, 24(6):1182, 2010.

[107] A.Y. Starikovskii, A.A. Nikipelov, M.M. Nudnova, and D.V. Roupassov. Sdbd plasma actuator with nanosecond pulse-periodic discharge. *Plasma*

*Sources Science and Technology*, 18:034015, 2009.

[108] S. Mahadevan T. Deconinck and L.L. Raja. Computational simulation of coupled non-equilbirium discharge and compressible flow phenomena in a microplasma thruster. *Journal of Applied Physics*, 106:063305–1, 2009.

[109] M. Teschke, J. Kedzierski, E.G. Finantu-Dinu, D. Korzec, and J. Engemann. High-speed photographs of a dielectric barrier atmospheric pressure plasma jet. *Plasma Science, IEEE Transactions on*, 33(2):310–311, 2005.

[110] M. Uddi, N. Jiang, E. Mintusov, I.V. Adamovich, and W.R. Lempert. Atomic oxygen measurements in air and air/fuel nanosecond pulse discharges by two photon laser induced fluorescence. *Proceedings of the Combustion Institute*, 32(1):929–936, 2009.

[111] T. Unfer and J.P. Boeuf. Modelling of a nanosecond surface discharge actuator. *Journal of physics D: applied physics*, 42(19):194017, 2009.

[112] K. Urabe, T. Morita, K. Tachibana, and B.N. Ganguly. Investigation of discharge mechanisms in helium plasma jet at atmospheric pressure by laser spectroscopic measurements. *Journal of Physics D: Applied Physics*, 43:095201, 2010.

[113] P.L.G. Ventzek, T.J. Sommerer, R.J. Hoekstra, and M.J. Kushner. Two-dimensional hybrid model of inductively coupled plasma sources for etch-

ing. *Applied physics letters*, 63(5):605–607, 1993.

[114] J.L. Walsh, F. Iza, N.B. Janson, V.J. Law, and M.G. Kong. Three distinct modes in a cold atmospheric pressure plasma jet. *Journal of Physics D: Applied Physics*, 43:075201, 2010.

[115] F.M. White. *Viscous Fluid Flow 3e*. Tata McGraw-Hill Education, 1974.

[116] L. Wu, J. Lane, N.P. Cernansky, D.L. Miller, A.A. Fridman, and A.Y. Starikovskiy. Plasma-assisted ignition below self-ignition threshold in methane, ethane, propane and butane-air mixtures. *Proceedings of the Combustion Institute*, 33(2):3219–3224, 2011.

[117] X. Yuan and L.L. Raja. Computational study of capacitively coupled high-pressure glow discharges in helium. *Plasma Science, IEEE Transactions on*, 31(4):495–503, 2003.

[118] X. Yuan, J. Shin, and L.L. Raja. One-dimensional simulation of multi pulse phenomena in dielectric-barrier atmospheric-pressure glow discharges. *Vacuum*, 80(11):1199–1205, 2006.

[119] M.B. Zheleznyak, A. Mnatsakanian, and S.V. Sizykh. Photoionization of mixtures of nitrogen and oxygen by gas discharge radiation teplofiz. vysokih temp. 1982.